Impedance and resolvent methods for calculating the shear waves spectra in 1D and 2D phononic waveguides

Maria Korotyaeva

université de BORDEAUX

Thèse

Pour obtenir le grade de

DOCTEUR EN SCIENCES
DE L'UNIVERSITÉ DE BORDEAUX

ÉCOLE DOCTORALE DES SCIENCES PHYSIQUES ET DE L'INGENIEUR
SPÉCIALITÉ : MÉCANIQUE

Par **Maria KOROTYAEVA**

Impedance and resolvent methods for calculating the shear waves spectra in 1D and 2D phononic waveguides

Directeur de thèse : M. Alexander SHUVALOV, Directeur de Recherche CNRS
Co-directeur : M. Olivier PONCELET, Chargé de Recherche CNRS,
Institut de Mécanique et d'Ingénierie (I2M), Université de Bordeaux

Soutenue le 6 novembre 2014 devant le jury composé de

Président	M. Alain BACHELOT, Professeur	Université de Bordeaux
Rapporteur	M. Emmanuel LE ClÉZIO, Professeur	Université Montpellier 2
Rapporteur	M. Bruno LOMBARD, Chargé de Recherche CNRS	LMA, Marseille
Examinateur	M. Jérome VASSEUR, Professeur	Université Lille 1
Examinateur	M. Alexander SHUVALOV, Directeur de Recherche CNRS	Université de Bordeaux, I2M
Examinateur	M. Olivier PONCELET, Chargé de Recherche CNRS	Université de Bordeaux, I2M
Invité	M. Anton KUTSENKO, Docteur	Université de Lorraine

Abstract

We propose two methods for calculating the shear waves spectra in 1D and 2D phononic crystal (PC) waveguides. Starting this study with 1D PC, we consider the 1D-periodic coated substrate. Here we develop scalar impedance method providing efficient means for analysis and calculation of dispersion spectrum.

The main focus of our work in on the 2D PC's: the 2D PC layer on a substrate, the free PC plate and the PC plate sandwiched between two substrates. Since the propagator $\mathbf{M}$ over a unit cell approximated by Fourier harmonics in one coordinate can have very large components, we introduce its resolvent $\mathbf{R} = (z\mathbf{I} - \mathbf{M})^{-1}$ (z is a complex number outside of $\mathrm{spec}\mathbf{M}$) as a numerically stable substitute. Another two key tools given in terms of the resolvent, a spectral projector $\mathbf{P}_d$ and propagator $\mathbf{M}_d$ for the decreasing modes, come into play in the case of a waveguide with a substrate.

The resolvent method providing simple dispersion and wave field equations in terms of $\mathbf{R}$, $\mathbf{P}_d$ and $\mathbf{M}_d$ has several advantages. It is of a good precision due to the exact solution in one direction, computationally cheap due to the reduction of the problem to one unit cell even in a semi-infinite substrate, and versatile since it is applicable to uniform, 1D- or 2D-periodic structures. Moreover, it is extendible to P/SV waves and 3D PC.

In numerical examples, we model low-frequency band gaps and compare them for the mirror-symmetric and perturbed profiles.

Keywords: Phononic crystals, Guided waves, Propagator, Resolvent, Spectral projector

Résumé. Méthodes de l'impédance et de la résolvante pour le calcul des modes de cisaillement dans des guides d'ondes phononiques 1D et 2D

Nous proposons deux méthodes pour calculer le spectre des ondes de cisaillement dans les cristaux phononiques (CP) 1D et 2D. Commençant notre étude par les CP 1D, nous développons la méthode des impédances scalaires pour la couche sur le substrat 1D.

Le focus principal de ce travail est sur les CP 2D : en particulier, on considère la couche sur le substrat 2D, la plaque à conditions libres 2D et la couche entre les deux substrats 2D. Comme la matrice propagateur $\mathbf{M}$ à travers la cellule unitaire obtenue via l'expansion des ondes planes dans une coordonnée peut avoir des composants très grandes, notre approche consiste à la substituer par sa résolvante $\mathbf{R} = (z\mathbf{I} - \mathbf{M})^{-1}$ qui est numériquement stable (où z est un nombre complexe hors de $\mathrm{spec}\mathbf{M}$). Deux autres outils centraux définis par la résolvante, le projecteur spectral $\mathbf{P}_d$ et propagateur $\mathbf{M}_d$ pour les ondes évanescentes, entrent en jeu pour le cas des CP avec un substrat.

La méthode de la résolvante, fournissant les équations de dispersion et du champ d'ondes en termes de $\mathbf{R}$, $\mathbf{P}_d$ et $\mathbf{M}_d$, a de multiples avantages. Elle est d'une bonne précision grâce à la solution exacte dans une coordonnée, efficace grâce à la réduction du problème à une seule cellule unitaire, même pour un substrat semi-infini, et polyvalente, puisque applicable pour les structures uniformes ou périodiques à 1D ou 2D. De plus, la méthode peut être généralisée aux CP à 3D et aux ondes vectorielles.

Dans les exemples numériques, nous calculons les bandes d'arrêt de basse fréquence et les comparons avec les profils de symétrie axiale et les profils perturbées.

Mots-clés: cristaux phononiques, ondes guidées, propagateur, résolvante, projecteur spectral

Résumé étendu. Méthodes de l'impédance et de la résolvante pour le calcul des modes de cisaillement dans des guides d'ondes phononiques 1D et 2D

Nous proposons deux méthodes pour calculer le spectre des ondes de cisaillement dans les cristaux phononiques (CP) à une et deux dimensions (1D et 2D). Les CP sont des structures périodiques, dont le spectre d'onde acoustique présente des bandes acoustiques d'arrêt donnant lieu à des effets acoustiques particuliers. Les structures étudiées sont constituées d'inclusions solides distribuées périodiquement dans une matrice solide. Bien que les méthodes proposées puissent être élargies aux CP tri dimensionnels (3D) et aux ondes vectorielles, nous ne considérerons que la propagation des ondes scalaires à travers des CP 1D et 2D afin de simplifier le problème posé.

Nous commençons notre étude par les CP 1D, et nous développons la méthode des impédances scalaires pour la couche sur le substrat 1D. Une analyse rigoureuse des fonctions d'impédance nous permet d'obtenir une formulation alternative du problème posé; cette approche se révèle plus avantageuse par rapport à la formulation commune de la matrice de transfert. En particulier, la monotonicité des fonctions impédance par rapport à la fréquence ω et au nombre d'ondes k_x permet la visualisation graphique des racines des équations de dispersion et clarifie la connectivité des branches rompues d'ondes de Love. Ici x dénote la direction (latérale) de propagation. De plus, le comportement des fonctions d'impédance soutient la relation entre le nombre des ondes de Love dans les bandes d'arrêt et le nombre de résonances de la couche.

Nous illustrons les phénomènes spectraux observés au moyen de diverses exemples numériques et comparons ces derniers avec les spectres des autres structures des CP. Le spectre de dispersion d'un CP 1D formé par une couche sur le substrat est comparé dans un premier temps avec le cas classique d'un substrat homogène recouvert par une couche

homogène ou une couche 1D. Dans un second temps, cette comparaison sera faite cette fois avec un substrat CP 1D sans la couche. On constate de multiples différences dans le spectre. Par exemple, on constate qu'un substrat périodique, en contraste avec un substrat homogène, admet des ondes localisées apparaissant à des fréquences finies quand $k_x = 0$. La différence générale entre les ondes de Love et les ondes de surface est que chaque bande d'arrêt à k_x fixé peut contenir au plus une onde de cisaillement de surface, tandis qu'elle peut contenir plusieurs ondes de Love (leur nombre est égal au nombre des résonances de la couche qui tombent dans cette bande d'arrêt). Un autre effet significatif de la couche peut être constaté dans un cas assez typique lorsqu'un substrat périodique à surface libre n'admet que des modes de cisaillement de surface que dans un étroit éventail de vitesses. Dans ce cas, même une faible perturbation par une fine couche crée des ondes localisées dans le domaine spectral où elles ne peuvent pas exister dans le cas d'un substrat sans couche.

Le focus principal de ce travail porte sur les CP 2D : en particulier, on considère la couche sur le substrat 2D, la plaque à conditions libres 2D et la couche entre les deux substrats 2D. On développe ici une méthode basée sur la résolvante de propagation. Le propagateur $\mathbf{M}$ (la matrice de monodromie) à travers la cellule unitaire est obtenu par l'expansion en ondes planes dans une coordonnée. Comme la matrice $\mathbf{M}$ peut avoir des composantes très grandes, nous substituons cette matrice par sa résolvante $\mathbf{R} = (z\mathbf{I} - \mathbf{M})^{-1}$, où z est un nombre complexe hors du spectre de $\mathbf{M}$. La norme de $\mathbf{R}$ étant bornée, $\mathbf{R}$ est numériquement stable. Cette approche permet de contourner les instabilités du propagateur à travers la cellule élémentaire de la plaque. En général, la résolvante est la solution d'une équation différentielle de Riccati dans la direction de la profondeur. Le calcul explicite de la résolvante peut être simplifié considérablement si le milieu est homogène au moins partiellement dans sa profondeur. Dans ce cas, la cellule unitaire peut être partagée en couches partielles 2D homogènes, homogènes dans la profondeur et 2D hétérogènes. Les résolvantes 'partielles' $\mathbf{R}_j$ de ces couches partielles peuvent être

calculées d'une manière plus rapide; soit explicitement ou comme une fonction de la matrice système. La résolvante complète $\mathbf{R}$ est ensuite obtenue via les $\mathbf{R}_j$ en utilisant la règle de la chaîne pour la résolvante.

Pour une plaque à conditions libres 2D, les équation de dispersion et des champs de déplacement et de contrainte sont établis en introduisant la résolvante. Dans le cas des CP avec un substrat semi-infini, entrent en ligne de compte la résolvante $\mathbf{R}_s$ de la cellule unitaire du substrat, le projecteur spectral $\mathbf{P}_d$ et le propagateur $\mathbf{M}_d$ pour les ondes évanescentes.

Pour calculer le spectre de la dispersion des ondes localisées, la solution évanescente $\boldsymbol{\eta}$ est extraite en appliquant le projecteur $\mathbf{P}_d$ sur les modes évanescentes et en imposant l'égalité $\boldsymbol{\eta} = \mathbf{P}_d\boldsymbol{\eta}$. Le projecteur peut être considéré comme un filtre qui permet de ne conserver que les ondes spécifiquement choisies (évanescentes ou propagatives), tout en renonçant au reste. Il extrait les modes 'physiques' évanescentes dans la profondeur du substrat sans résoudre l'équation d'ondes, mais en utilisant la position des valeurs propres dans le plan complexe, tout en évitant leur calcule explicite. En général, cet opérateur peut être défini comme une intégrale curviligne : $\mathbf{P}_d = \frac{1}{2\pi i}\int_{|z|=1-0}\mathbf{R}_s(z)dz$. Cette définition peut être implémentée comme une fonction matricielle de la résolvante $\mathbf{R}_s$, et son calcul admet des simplifications sous la condition que la cellule unitaire complète soit totalement uniforme ou uniforme dans le profondeur.

Pour calculer le champ des modes évanescents sans avoir recours au propagateur $\mathbf{M}$ qui est numériquement instable, on utilisera la matrice $\mathbf{M}_d$ définie par l'intégrale curviligne $\mathbf{M}_d = \frac{1}{2\pi i}\int_{|z|=1-0} z\mathbf{R}_s(z)dz$ et implémentée comme une fonction matricielle de la résolvante $\mathbf{R}_s$.

La méthode de la résolvante, fournissant les équations de la dispersion et du champ d'ondes en termes de $\mathbf{R}$, $\mathbf{P}_d$ et $\mathbf{M}_d$, a de multiples avantages. Le propagateur $\mathbf{M}$ et sa résolvante $\mathbf{R}$ sont obtenus à l'aide d'un développement en ondes planes tronqué (DOP) selon la direction de propagation couplée à un calcul intégral exact, alors que les autres

méthodes, comme le DOP 2D ou la méthode des éléments finis, impliquent une troncature suivant deux directions. Par conséquent, notre méthode permet une plus grande précision et une meilleure efficacité grâce à la taille réduite de la matrice à traiter. La méthode de la résolvante est en outre efficace grâce à la réduction du problème à une seule cellule unitaire au moyen du projecteur $\mathbf{P}_d$ même pour un substrat semi-infini. De plus, elle est polyvalente, applicable pour les structures uniformes ou périodiques à 1D ou 2D. On remarquera que l'expansion en séries de Fourier empêche l'application de la méthode de la résolvante à d'autres types de CP, tels des CP fluide/solide, solide/fluide ou solide avec des inclusions vides. Dans ces cas, un changement de base de projection en lieu de l'expansion de Fourier pourrait apporter une solution.

L'utilisation de la méthode est présentée à travers plusieurs exemples numériques. On montre que les branches à basse fréquence peuvent soit se croiser soit se repousser, donnant lieu, dans ce dernier cas, à des bandes d'arrêt de basse fréquence à l'intérieur de la zone de Brillouin. Ces bandes d'arrêt sont d'autant plus larges quand les inclusions sont proches de la surface à conditions libres ou à l'interface; de plus leur taille augmente avec la taille des inclusions. Nous comparons différentes bandes d'arrêt de basse fréquence pour établir les profils de symétrie axiale et les profils perturbés. Les bandes d'arrêt proviennent de la répulsion des branches de dispersion au bord de la zone de Brillouin pour les profiles de symétrie axiale et au bord ainsi qu'à l'intérieur de la zone de Brillouin pour les profiles asymétriques. Les champs de déplacement et de contrainte sont calculés pour les CP avec les valeurs de raideur très différentes entre la matrice et les inclusions, ce qui nous permet de révéler la géométrie du CP.

Table of contents

Abstract / Résumé bref et étendu **2**

1 Introduction **11**

2 Love waves in 1D PC **17**

2.1 Introduction 17

2.2 Background 19

2.2.1 Propagator (monodromy matrix) 19

2.2.2 Definition of conditional and modal SH impedances 21

2.2.3 Statement of the Love wave problem 22

2.3 Properties of the impedances 23

2.3.1 Layer impedance 23

2.3.2 Substrate impedances 25

2.4 Love wave spectrum 28

2.4.1 Overview of the spectrum 28

2.4.2 Number of Love waves per a stopband 28

2.4.3 Monotonicity of the Love wave branches 29

2.4.4 Lower bound of the Love wave spectrum 30

2.4.5 Fundamental branch 30

2.5 Numerical examples 32

2.6 Conclusion 37

3 Love waves in 2D PC **39**

3.1 Introduction 39

3.2 Problem statement 40

3.3 The resolvent 43

3.4 The spectral projector 45

3.4.1 The eigenspaces 45

3.4.2 The spectral projector definition via propagator eigenvalues 47

3.4.3 The alternative definition of the spectral projector via path integral . 48

3.5 The dispersion equation 48

3.5.1 Love wave spectrum 49

3.5.2 Projection of the spectrum of the propagating waves 51

3.6 Numerical examples 52

3.7 Conclusion 55

4 Plate waves in 2D PC **57**

4.1 Introduction 57

4.2 Problem statement 58

4.3 The dispersion equation in terms of the propagator 59

4.4 The dispersion equation in terms of the resolvent 60

4.5 The dispersion spectrum for mirror symmetric profiles 61

4.5.1 Problem decomposition for symmetric and antisymmetric waves . . 61

4.5.2 Dispersion equations in stable terms 64

4.6 Numerical examples 65

4.6.1 One array of inclusions 65

4.6.2 Two arrays of inclusions 68

4.7 The displacement and traction field 69

4.7.1 The wave field equation 69
4.7.2 Numerical examples 70
4.8 Conclusion 72

5 Guided waves in 2D PC **75**
5.1 Introduction 75
5.2 Problem statement 77
5.3 Dispersion equation with resolvent and projector 78
5.3.1 The localized waves spectrum 78
5.3.2 Projection of the spectrum of the propagating waves 80
5.4 The dispersion equation for the mirror-symmetric case 80
5.4.1 Problem decomposition for symmetric and antisymmetric waves . . 80
5.4.2 Dispersion equations in stable terms 82
5.5 Numerical examples 83
5.5.1 Square inclusions and 2D substrates 83
5.5.2 Circular inclusions and layered substrates 84
5.6 The displacement and traction field 85
5.6.1 The propagators for decreasing modes 85
5.6.2 The wave field equation 86
5.6.3 Numerical examples 88
5.7 Conclusion 90

6 Conclusions **93**

A Useful identities **99**
A.1 Chain rule and Hilbert identity 99
A.2 **T**-unitarity 100
A.3 Mirror-symmetric sublayers 103

B Explicit formulas **105**

C Options for calculation **109**

C.1 Options for calculation of the resolvent 109

C.1.1 2D-uniform sublayer. The explicit formula 110

C.1.2 Depth-uniform sublayer. The function of system matrix 110

C.1.3 Multilayer. The chain rule 111

C.1.4 Examples of the calculation scheme 112

C.2 Options for calculation of the projector 113

C.2.1 2D-uniform substrate. The explicit formula 114

C.2.2 Depth-uniform substrate. The function of system matrix 114

C.2.3 2D-periodic substrate. The function of resolvent matrix 114

C.2.4 2D-periodic substrate. The sum of resolvents 116

C.3 Calculation of the propagators for decreasing modes 117

D The spectrum of the propagating waves **119**

D.1 Dispersion equation 119

D.2 Numerical implementation 120

D.3 Numerical examples 120

Bibliography **123**

Chapter 1

Introduction

Phononic crystals (PC) are periodic structures whose wave spectra exhibit frequency band gaps; see [1]. This feature makes possible extraordinary effects such as total transmission, negative refraction, superlensing etc. The present study is concerned with SH (shear horizontal) waves in solid PC with boundaries and interfaces. We start with a relatively simpler case of Love waves in the coated periodically multilayered or functionally graded isotropic substrate. This setup may be viewed as a particular case of a periodic laminate with structural defect; see [2]–[10]. The layering is parallel to the surface, so that the substrate is vertically periodic and laterally homogeneous. Thus this is a 1D PC structure. The method of scalar impedances is an appropriate tool for tackling this problem. The main focus of this work is on the 2D PC laterally periodic depth-dependent structures represented by 2D solid isotropic inclusions (bars) parallel to the surface of a solid isotropic matrix and periodic along this surface. Taking the direction of lateral periodicity as the coordinate x_1, the properties of such a 2D structure depend (periodically or not) on the depth coordinate x_2 and are uniform along the second lateral coordinate x_3 parallel to the bars; see Fig. 1.1. Hence this structure admits uncoupling of the SH mode propagating in the plane X_1X_2 and polarized along the axis X_3. Specifically, we consider SH waves for a 2D PC layer on a uniform or 2D-periodic substrate (2D Love waves), for a

free 2D PC layer (2D plate waves), and for a 2D PC layer between two periodic substrates (2D guided waves).

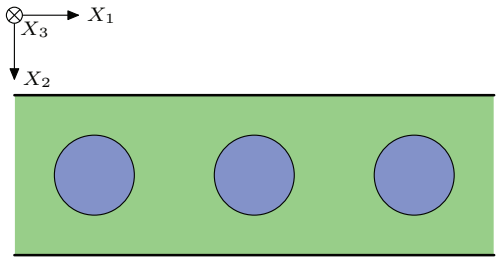

Figure 1.1: Example of a 2D PC structure.

Much work which has recently been devoted to the dispersion spectra of the PC layer on a substrate (see [11]–[21]) and of the PC plate and the PC sandwiched plate (see [22]–[37]) used extended plane wave expansion (PWE), supercell method in combination with PWE, finite difference method (FDM) or, most commonly, with finite elements method (FEM). Moreover, note other related techniques for the waveguides such as the Dirichlet-to-Neumann approach (see [38]) or scattering and Green function approach for discrete structures (see [39]–[41]). The main aim of this thesis is to propose a new method for calculation of the SH dispersion spectrum of bounded 2D PC (note that it can be extended to P/SV waves and 3D PC). The method can be applied, like the supercell method, for any type of substrate, uniform, depth-uniform or 2D-periodic, whereas extended PWE for example is suitable only for uniform substrates. This 2D method proceeds from the propagator M over a vertical period of the structure (see § 3.2). Reducing consequently the waveguide problems to their unit cells by means of M makes our method less computationally expensive than other methods considering several unit cells of the periodic structure. M is approximated via truncated PWE in the lateral coordinate giving a matrix of large size (corresponding to the size of wave packet) $2(2N+1)\times 2(2N+1)$, where $2N+1$ is the number of Fourier harmonics. In particular, we take into account here the Floquet-Bloch form of displacement field in periodic media. Next, M is obtained by means of

exact integration in the depth coordinate in contrast to other methods (see above) involving truncation in all coordinates. Thus the advantages of this method are accuracy and efficiency due to the smaller size of the input matrix of coefficients of the governing system of equations ($O(N)$ instead of $O(N^2)$ for other methods). At the same time, the propagator $\mathbf{M}$ of large size becomes numerically unstable. This problem is circumvented by substituting instead of $\mathbf{M}$ its resolvent $\mathbf{R} = (z\mathbf{I} - \mathbf{M})^{-1}$ (z is a complex number outside of the spectrum of $\mathbf{M}$ and $\mathbf{I}$ denotes the identity matrix), which is numerically stable (see § 3.3).

The resolvent is the central object of our method which can therefore be called the resolvent method. We propose the resolvent as a numerically stable substitute for the exponentially growing propagator. The resolvent formalism is an amply developed theory to solve differential equations and study the spectral properties - thanks to its stabilizer feature. Nevertheless still it remains relatively unused in physical acoustics. Generally, a resolvent can be taken of any matrix $\mathbf{A}$ by choosing an appropriate z outside of the spectrum of $\mathbf{A}$. Therefore, it gives a small object by inverting a big one. Roughly speaking, it can be considered as a stable inverse. Here, we take the resolvent of the propagator.

The main idea to state the dispersion equation is the following. On a bounded piece of structure like a layer, the resolvent substitutes the layer propagator. For the problem including substrate(s) (Love waves and guided waves, see Chapters 3 and 5), another key tool defined by the resolvent $\mathbf{R}_s$ of the propagator through the unit-cell of the substrate comes into play. This key tool is a spectral projector $\mathbf{P}$ which allows us to extract the 'physical' modes decreasing or propagating into the depth of the substrate without solving the wave equation (see § 3.3). Spectral projector was first applied for surface waves in [42]; here we extend this tool to other types of structures. Note again that the projector extracting 'physical' modes is defined over a single unit cell, which makes our method less computationally expensive than the widely used supercell method, which requires considering several unit cells for the same purpose. Summarizing, the dispersion equation

for the PC waveguides can be formulated via two tools, the resolvent $\mathbf{R}_l$ of the layer(s) and the projector $\mathbf{P}_d$ on the decreasing modes in the half-space(s).

We calculate the wave field for the PC waveguides by extending the method developed for the dispersion equation. The initial wave field is given by the solution of the dispersion equation of the overall structure discussed above. To calculate the propagating wave field, we 'move' our tools inside the structure considering e.g. $\mathbf{R}_l(x_2, 0)$ for any $x_2 \in [d, 0]$ instead of $\mathbf{R}_l(d, 0)$. As before, we apply the resolvent $\mathbf{R}_l$ of the layer(s) for the wave field propagating inside a plate. However to calculate the wave field decreasing into the depth of the substrate, we can not use the projector $\mathbf{P}_d$ introduced above, since it only extracts the decreasing modes, but does not give the corresponding values. Here we introduce a new tool, a modification of the projector $\mathbf{P}_d$, the propagator $\mathbf{M}_d$ for the decreasing modes over a unit cell of the substrate (see § 5.6). This propagator is numerically stable, since it can be viewed as a substrate propagator $\mathbf{M}_s$ containing only eigenvalues corresponding to the decreasing modes and other eigenvalues replaced by zeros.

The means of calculation of the resolvent, the projector and the propagator for decreasing modes are as follows. The resolvent is calculated similarly as the propagator. In general, the resolvent satisfies the Riccati equation and hence can be computed by standard numerical means such as the Runge-Kutta method. At the same time, the calculation can often be simplified, since the unit cell can often be partitioned into the sublayers including the ones uniform along the depth or along the both coordinates. The 'partial' resolvents $\mathbf{R}_j$ of such sublayers can be calculated in a faster way (explicitly or as a function of a constant system matrix), and the overall resolvent $\mathbf{R}$ is obtained via $\mathbf{R}_j$ using the special chain rule. In general, the projector $\mathbf{P}_d$ on the decreasing modes is expressed as a contour integral $\mathbf{P}_d = \frac{1}{2\pi i} \int_{|z|=1-0} \mathbf{R}_s(z) dz$. This definition can be implemented as a function of the resolvent matrix. Moreover, like in the case of the resolvent, the calculation of $\mathbf{P}_d$ admits simplification, but this time only if the entire unit cell of a substrate is uniform or depth-uniform. The propagator $\mathbf{M}_d$ for decreasing modes is defined similarly as $\mathbf{P}_d$ by a

contour integral $\mathbf{M}_d = \frac{1}{2\pi i}\int_{|z|=1-0} z\mathbf{R}_s(z)dz$ and implemented as a matrix function of the resolvent.

In the thesis, we consider the analytical derivation of the dispersion equations and wave field equations for 2D PC structures and the implementation of the numerical solutions. We also use various numerical examples to discuss the observed physical features. In particular, we demonstrate how a variation of the structure of the PC (i.e. changing the size, material, form and position of inclusions) can make bandgaps appear or disappear. Special attention is given to the case of asymmetric periodic perturbation of a symmetric profile which can create absolute bandgaps due to a split of the formerly intersecting symmetric and antisymmetric dispersion branches.

The thesis is organized as follows. For comparison with the 2D cases, we proceed in Chapter 2 from the case of the SH Love waves in a coated vertically periodic substrate (1D PC). Due to the lateral homogeneity, the dispersion spectrum $\omega(k_1)$ is infinite and has no bandgaps. Also due to the lateral homogeneity, the SH propagator $\mathbf{M}$ is confined to the 2×2 size, so there is only one decreasing ('physical') and one increasing ('nonphysical') modes, which can be identified explicitly. Instead of using a most common propagator approach, we recast the dispersion equation in terms of the scalar impedances. Analytical properties of the impedances facilitate analysis of the spectrum and provide an insightful graphical method of visualizing roots of the dispersion equation. The results of Chapter 2 are published in [43]. Chapters 3-5 are devoted to 2D PC structures. Lateral periodicity makes this setup much more complicated than the case of 1D PC. First, the dispersion spectrum $\omega(k_1)$ folds up in the first Brillouin zone and acquires bandgaps. Secondly, the corresponding SH propagator $\mathbf{M}$ is now of a large size $2(2N+1) \times 2(2N+1)$ and respectively there is a large number $2N+1$ of decreasing and increasing Floquet-Bloch modes in the substrate. This calls for a resolvent $\mathbf{R}$ to bypass numerical instability of $\mathbf{M}$ and for a projector $\mathbf{P}$ in the substrate to extract 'physical' modes decaying into the depth without calculating them explicitly. These objects are introduced in Chapter 3 which deals with

the Love waves in a laterally periodic 2D PC layer on a substrate. The dispersion equation is expressed via the resolvent in the layer and the projector in the substrate. Examples of the formation of bandgaps in the subsonic dispersion spectra depending on the position of the inclusions are discussed. Chapter 4 describes the SH waves in a free 2D PC plate. The starting point is the formulation of the dispersion equation via propagator M which is then recast in stable terms of the resolvent. Chapter 5 is concerned with the SH guided waves in a 2D PC layer between two substrates. This case involves two substrates, hence the dispersion equation is written via the resolvent in the layer and two projectors in the substrate. Chapters 4 and 5 also discuss in some detail the uncoupled dispersion equations for symmetric and antisymmetric branches in the case of a mirror-symmetric profile of the structure. Examples are provided where the asymmetric perturbation of the symmetric profile breaks the intersection of the symmetric and antisymmetric branches and creates absolute bandgaps. Moreover, in Chapters 4 and 5 we derive the wave field equation for displacement and traction field and illustrate it by some numerical examples. The results of Chapters 3-5 are published in the papers [44] and [45]. Mathematical technicalities, explicit formulas for the model uniform case and different options for calculating the resolvent and projector in the general are discussed in the Appendices A, B and C respectively. Application of the resolvent method to the calculation of the Floquet-Bloch spectrum of propagating SH waves in the 2D infinite PC is demonstrated in the Appendix D.

Chapter 2

Love waves in a vertically periodic coated substrate

2.1 Introduction

Acoustic wave spectra in periodic laminates with structural defects has been studied from different perspectives; see [2]–[10]. One of the topical problems studies the effect of coating on SH waves in a periodically layered substrate. It is well known that if a semi-infinite substrate is homogeneous then its coating by 'slow' layer is a means to achieve the SH wave localisation (decay into the depth). These are the classical Love waves whose phase-velocity branches $v\left(k_x\right)=\omega/k_x$ must be subsonic with respect to the substrate, i.e. be confined between the shear speeds of the coating layer and the substrate $c_l<c_s$ (here k_x is the wavenumber along the surface, and c_l means $\min c_l\left(y\right)$ if the coating is transversely inhomogeneous); see [46]. The situation is different if the substrate is periodic. For any k_x (possibly $k_x=0$), taking ω in the Floquet stopbands ensures by itself decaying waves without setting upper limit on their velocity $v=\omega/k_x$ [2, 3, 47, 48]. At the same time, it is also possible that SH surface waves in a free (uncoated) periodic substrate are restricted to a fairly narrow velocity range, as detailed in [49]. For instance, this may be often the

case in substrates with a bilayered or monotonic profile on a period; moreover, there is no SH surface waves at all if the profile is even. In such cases, coating the substrate creates or drastically enriches the spectrum of SH localised waves and thus plays a similar role as in the classical setting with a homogeneous substrate, though in a more complicated context (e.g. the coating does not have to be 'slow'). In view of different terminology used in the literature, let us agree to refer to the SH localised waves in the uncoated and coated periodic substrate as the surface waves and the Love waves, respectively. The former are related to a strictly periodic halfspace, the latter imply perturbed periodicity. Similar in that they both lie in the Floquet stopbands of a substrate and decay into the depth, these are actually two different types of wave solutions. One essential difference is that any periodic substrate admits no more than a single SH surface wave per a stopband, while there is no such limitation for Love waves. This feature of possible wave mutliplexing is another interesting functional capacity of coating.

The present Chapter studies the dispersion spectrum of Love waves in a coated substrate with arbitrary periodic piecewise constant or functionally graded (see [49, 50]) variation of material properties in the depth direction. The motivation is to gain better understanding into the spectral effect of coating and to obtain some general analytical results. The structure and main results of the Chapter are as follows. The background of the problem is outlined in §2.2. Here we state the SH wave equation, introduce the notion of propagator for 1D periodic structure (also referred to as monodromy matrix) and explain how it defines spectrum of the propagating waves. Unlike commonly used formulation via the transfer matrix, the dispersion equation is set as equality of scalar SH impedances of the coating layer and the substrate. The advantage of using impedances lies in their helpful analytical properties such as monotonicity in ω and k_x which is demonstrated in §2.3 and exploited in §2.4.1. It enables insightful graphical visualisation of roots of the dispersion equation that clarifies the nature and connectivity of the broken branches of Love waves (§2.4.1.1), and it also underpins the relation of the number of Love waves in a

stopband to the number of resonances of the coating layer (§2.4.1.2). The monotonicity of Love dispersion branches $\omega(k_x)$ is proved in §2.4.1.3 and their lower bound is discussed in §2.4.1.4. The criterion for existence of the fundamental Love branch with an origin at zero ω and k_x is derived in §2.4.2. General findings are illustrated in §2.5 by examples of Love waves which arise due to coating of periodically layered and functionally graded substrates. Concluding remarks are presented in §2.6.

2.2 Background

2.2.1 Propagator (monodromy matrix)

Consider the SH wave $u_z(x,y,t) = u(y)\, e^{i(k_x x - \omega t)}$ in an isotropic medium with piecewise continuous density $\rho(y)$ and shear modulus $\mu(y)$. The wave equation

$$(\mu u')' - \mu k_x^2 u = -\rho\omega^2 u \tag{2.1}$$

may be recast as the system

$$\mathbf{Q}\eta = \eta' \text{ with } \mathbf{Q}(y) = i\begin{pmatrix} 0 & -\mu^{-1} \\ \mu k_x^2 - \rho\omega^2 & 0 \end{pmatrix},\ \eta(y) = \begin{pmatrix} u \\ if \end{pmatrix}, \tag{2.2}$$

where $f = \mu u'$ is the traction and $' \equiv \mathrm{d}/\mathrm{d}y$. For any initial condition $\eta(y_0)$, the solution of the first-order differential system (2.2) is

$$\eta(y) = \mathbf{M}(y, y_0)\,\eta(y_0) \text{ with } \mathbf{M}(y, y_0) \equiv \begin{pmatrix} M_1 & M_2 \\ M_3 & M_4 \end{pmatrix} = \widehat{\int_{y_0}^{y}} (\mathbf{I} + \mathbf{Q}\mathrm{d}y), \tag{2.3}$$

where $\mathbf{M}$ is the matricant (propagator or transfer matrix) and $\widehat{\int}$ is the multiplicative integral which expands in the Peano series and reduces to a product $\prod_{j=n}^{1} \exp \mathbf{Q}_j (\Delta y)_j$ if

$\mathbf{Q}(y)$ takes piecewise constant values $\mathbf{Q}_j$ on $[y_0, y]$; see [51]. In view of the explicit form of $\mathbf{Q}$ in (2.2), it follows that $\det \mathbf{M} = 1$ and that $\mathrm{Im}M_{1,4} = 0,\ \mathrm{Re}M_{2,3} = 0$.

In the case of periodic properties $\rho(y) = \rho(y+T)$ and $\mu(y) = \mu(y+T)$, the central role is played by the matricant over the period, or the monodromy matrix, $\mathbf{M}(y+T, y)$ $[= \mathbf{M}(y,0)\,\mathbf{M}(T,0)\,\mathbf{M}^{-1}(y,0)]$ with eigenvectors $\mathbf{w}_{1,2} = \mathbf{w}_{1,2}(y)$ and with eigenvalues $q_{1,2}$ ($q_1 = q_2^{-1}$) independent of y.

The monodromy matrix gives the projection of the spectrum of the propagating waves on the plane $\{\omega, k_x\}$ in the following way. The so-called Lyapunov function $\Delta(\omega^2, k_x^2) = \frac{1}{2}\mathrm{trace}\mathbf{M}(T,0)$ partitions the $\{\omega, k_x\}$-plane into alternating passband and stopband areas where, respectively,

$$\begin{gathered} |\Delta(\omega^2, k_x^2)| < 1 \Rightarrow \text{complex } q_1 \neq q_2 \text{ with } |q_{1,2}| = 1,\ \ \mathbf{w}_1^+ \mathbf{T} \mathbf{w}_2 = 0; \\ |\Delta(\omega^2, k_x^2)| > 1 \Rightarrow \text{real } q_{1,2} \gtrless 1,\ \mathbf{w}_1^+ \mathbf{T} \mathbf{w}_1 = \mathbf{w}_2^+ \mathbf{T} \mathbf{w}_2 = 0 \end{gathered} \tag{2.4}$$

($^+$ means Hermitian conjugation and $\mathbf{T}$ is a matrix with zero diagonal and unit off-diagonal components). Equation $|\Delta(\omega^2, k_x^2)| = 1$ defines the set of curves $\{\omega_e(k_x)\}$ of band edges where a degenerate eigenvalue $q_d = \pm 1$ corresponds to a single eigenvector $\mathbf{w}_d$ so that $\mathbf{w}_1, \mathbf{w}_2 \to \mathbf{w}_d$ at $|\Delta| \to 1$ (barring the exceptional case of a zero-width stopband and also the point $\omega = 0,\ k_x = 0$ where (2.1) has a trivial solution $u(y) = const$). Note that $|\Delta(0, k_x^2)| > 1$ at $k_x \neq 0$. Indeed the first stopband area $[0, \omega_e^{(1)}(k_x))$ for the case of periodic media is what is the subsonic interval for homogeneous media.

In the following, we refer to eqs. (2.1)-(2.3) with $\rho_l,\ \mu_l$ for a coating layer $y \in [-d, 0]$ and with $\rho_s,\ \mu_s$ for a T-periodic substrate $y \geqslant 0$. Denote

$$\begin{gathered} c_l^2(y) = \mu_l/\rho_l,\ \ \bar{c}_l^2 = \langle \mu_l \rangle / \langle \rho_l \rangle \ \ \text{with} \ \ \langle \cdot \rangle \equiv \tfrac{1}{d}\textstyle\int_{-d}^{0} \cdot\, \mathrm{d}y, \\ c_s^2(y) = \mu_s/\rho_s,\ \ \bar{c}_s^2 = \langle \mu_s \rangle / \langle \rho_s \rangle \ \ \text{with} \ \ \langle \cdot \rangle \equiv \tfrac{1}{T}\textstyle\int_{0}^{T} \cdot\, \mathrm{d}y, \end{gathered} \tag{2.5}$$

where $c(y)$ implies 'local' speed of short waves and $\bar{c}$ implies effective speed of long

waves in the direction x. Note that we will use the same symbol $\langle\cdot\rangle$ for an average across the layer and across the substrate period (the label l or s of the enclosed quantities suffices to clarify which is the case).

2.2.2 Definition of conditional and modal SH impedances

Assume that a layer $y \in [-d, 0]$ with $\rho_l(y)$ and $\mu_l(y)$ is free of traction at the upper face and, under this condition, introduce via (2.3) the impedance z_l at the lower face:

$$f(-d) = 0,\ f(0) = -z_l u(0) \ \Rightarrow\ z_l = iM_3(0,-d)\, M_1^{-1}(0,-d)\,. \tag{2.6}$$

The 'conditional' impedance $z_l = z_l(\omega^2, k_x^2)$ is a real function, whose zeros and poles define the spectra $\{\omega_{\mathrm{f/f}}(k_x)\}$ and $\{\omega_{\mathrm{f/c}}(k_x)\}$ of SH waves in the given layer with free/free or free/clamped faces ($f(-d) = 0$ and $f(0) = 0$ or $u(0) = 0$), respectively. The least value $\omega^{(1)}_{\mathrm{f/f}}(k_x)$ among $\{\omega_{\mathrm{f/f}}(k_x)\}$, i.e. the first zero of z_l, satisfies

$$k_x \min_{y\in[-d,0]} c_l(y) \leqslant \omega^{(1)}_{\mathrm{f/f}}(k_x) \leqslant k_x \bar{c}_l\,, \tag{2.7}$$

while the first pole of z_l is $\omega^{(1)}_{\mathrm{f/c}}(k_x) \sim O(1)$ at any k_x. The definition $(2.6)_2$ obviously reduces to

$$z_l = \mu_l k_y \tan k_y d \ \text{ with } k_y = \sqrt{\omega^2/c_l^2 - k_x^2} \tag{2.8}$$

if the layer is homogeneous (has constant ρ_l, μ_l).

Next, consider a periodic half-space $y \geqslant 0$. With reference to (2.3), define the Floquet modes $\eta_{1,2}(y)$ via the eigenvectors $\mathbf{w}_{1,2}$ of, specifically, $\mathbf{M}(T,0)$:

$$\eta_\alpha(y) = \mathbf{M}(y,0)\,\mathbf{w}_\alpha, \ \text{ where } \mathbf{M}(T,0)\,\mathbf{w}_\alpha = q_\alpha \mathbf{w}_\alpha;\ \ \alpha = 1,2. \tag{2.9}$$

By this definition, $\eta_\alpha(nT) = q_\alpha^n \mathbf{w}_\alpha$ for $n = 0, 1, ...$ Using the notations $\eta_\alpha = (u_\alpha\ if_\alpha)^T$ and

$\mathbf{w}_\alpha = (a_\alpha\ b_\alpha)^T$, $\mathbf{w}_d = (a_d\ b_d)^T$ (^{T} means transposition), introduce the modal impedances $Z_{s\alpha}$ at the substrate surface as follows

$$\begin{gathered} f_\alpha(0) = -Z_{s\alpha} u_\alpha(0) \Leftrightarrow Z_{s\alpha} = i b_\alpha a_\alpha^{-1},\ \alpha = 1, 2; \\ \left(Z_{s1} = Z_{s2} = i b_d a_d^{-1} \text{ at } |\Delta| = 1 \text{ if } a_d \neq 0\right), \end{gathered} \tag{2.10}$$

where

$$\frac{i b_\alpha}{a_\alpha} = \frac{i M_3(T,0)}{q_\alpha - M_4(T,0)} \left(= \frac{M_1(T,0) - q_\alpha}{i M_2(T,0)}\right),\ q_\alpha = \Delta \pm \sqrt{\Delta^2 - 1}. \tag{2.11}$$

Our case of interest is when ω, k_x lie in the stopbands. The impedances $Z_{s\alpha}(\omega^2, k_x^2)$ at $|\Delta| \geqslant 1$ (hence $\mathbf{w}_\alpha^+ \mathbf{T} \mathbf{w}_\alpha = 0$, see (2.4)$_2$) are real functions, with zeros and poles on the sets of curves $\{\omega_N(k_x)\}$ and $\{\omega_D(k_x)\}$ which yield $b_\alpha = 0$ and $a_\alpha = 0$ and thus fulfil the Neumann $f(0) = 0$ ($\Leftrightarrow u'(0) = 0$) and Dirichlet $u(0) = 0$ conditions, respectively. It is known that each closed stopband contains one Neumann branch $\omega_N(k_x)$ and one Dirichlet branch $\omega_D(k_x)$ (missing in the first stopband only), and that these two branches coincide with the opposite edges of each stopband if $\rho(y)$ and $\mu(y)$ are even about the midpoint of a period $[0, T]$. Similarly to (2.7), the first Neumann branch $\omega_N^{(1)}(k_x)$ lying in the first stopband $\omega \in [0, \omega_e^{(1)}(k_x))$ satisfies

$$k_x \min_{y \in [0,T]} c_s(y) \leqslant \omega_N^{(1)}(k_x) \leqslant \omega_e^{(1)}(k_x) \leqslant k_x \bar{c}_s, \tag{2.12}$$

while the second stopband and hence the first Dirichlet branch occur at finite frequency whatever small k_x is. For more details, see [52].

2.2.3 Statement of the Love wave problem

Consider Love waves in a periodic substrate $y \geqslant 0$ coated by a layer $y \in [-d, 0]$. The Love-wave spectrum $\{\omega_L(k_x)\}$ follows from the SH wave equation under the traction-free condition $f(-d) = 0$ at the upper surface, continuity of displacement $u(y)$ and traction

$f(y)$ at the layer/substrate interface, and the requirement that the solution must vanish at $y \to \infty$. The latter implies that the branches $\omega_L(k_x)$ are confined to the stopbands and that the Love waves must incorporate the decreasing Floquet mode in the substrate ($|q_\alpha| < 1$). In the following, we choose to label the two Floquet modes so that $\alpha = 1$ and $\alpha = 2$ always correspond to, respectively, decreasing and increasing ones, i.e. $|q_1| < 1 < |q_2|$ in any stopband. In this regard, we will refer to the impedances Z_{s1} and Z_{s2} in the stopbands as physical and non-physical one.

Using the above auxiliary conditions and the definitions (2.6) and (2.10) of the layer and substrate impedances, the dispersion equation on the Love spectrum may be posed in the form

$$z_l\left(\omega^2, k_x^2\right) = Z_{s1}\left(\omega^2, k_x^2\right) \quad \text{for} \quad \left|\Delta\left(\omega^2, k_x^2\right)\right| > 1 \text{ with } |q_1| < 1 < |q_2|. \tag{2.13}$$

Note that equation $z_l = Z_{s2}$ defines the branches $\omega_{nL}(k_x)$ of non-physical Love waves increasing into the depth. The impedance formulation of the problem is convenient due to some useful and general properties of the functions z_l and $Z_{s\alpha}$. These properties are considered next.

2.3 Properties of the impedances

2.3.1 Layer impedance

Using (2.2), let us develop positive functions $\rho_l(y)|u(y)|^2$ and $\mu_l(y)|u(y)|^2$ as follows

$$\begin{aligned} \rho_l|u|^2 &= i\eta^+(\mathbf{T}\tfrac{\partial \mathbf{Q}}{\partial(\omega^2)})\eta = i\eta^+\mathbf{T}\tfrac{\partial^2\eta}{\partial y\partial(\omega^2)} + i\left(\mathbf{Q}\eta\right)^+\mathbf{T}\tfrac{\partial\eta}{\partial(\omega^2)} \\ &= i(\eta^+\mathbf{T}\tfrac{\partial\eta}{\partial(\omega^2)})' = (f^*\tfrac{\partial u}{\partial(\omega^2)} - u^*\tfrac{\partial f}{\partial(\omega^2)})', \\ \mu_l|u|^2 &= -i\eta^+(\mathbf{T}\tfrac{\partial \mathbf{Q}}{\partial(k_x^2)})\eta = ... = -(f^*\tfrac{\partial u}{\partial(k_x^2)} - u^*\tfrac{\partial f}{\partial(k_x^2)})', \end{aligned} \tag{3.14}$$

where * means complex conjugation. Integrate both sides of (3.14) over the layer $y \in [-d, 0]$ under the condition $f(-d) = 0$, insert $f(0) = -z_l u(0)$ with real z_l from (2.6) and

express $u(y) = M_1(y, -d)\, u(-d)$ from (2.3). Hence

$$\left\langle \rho_l M_1^2 \right\rangle = \frac{1}{d} \frac{\partial z_l(\omega^2, k_x^2)}{\partial(\omega^2)} M_1^2(0, -d), \ \left\langle \mu_l M_1^2 \right\rangle = -\frac{1}{d} \frac{\partial z_l(\omega^2, k_x^2)}{\partial(k_x^2)} M_1^2(0, -d), \tag{3.15}$$

where $\langle \cdot \rangle$ denotes average across the layer, see (2.5). Next, multiplying (2.1) by complex conjugated $u^*(y)$ and manipulating likewise as above gives

$$\begin{gathered} -\tfrac{1}{d}\mu_l(0)\, u'(0)\, u^*(0) + \langle \mu_l |u'|^2 \rangle + k_x^2 \langle \mu_l |u|^2 \rangle = \omega^2 \langle \rho_l |u|^2 \rangle \ \Rightarrow \\ \tfrac{1}{d} z_l M_1^2(0, -d) + \langle \mu_l^{-1} |M_3|^2 \rangle + k_x^2 \langle \mu_l M_1^2 \rangle = \omega^2 \langle \rho_l M_1^2 \rangle. \end{gathered} \tag{3.16}$$

Note that (3.16) is consistent with identical vanishing of z_l and M_3 at $\omega = 0,\ k_x = 0$.

By (3.15) and (3.16), the impedance $z_l(\omega^2, k_x^2)$ for a layer with any $\rho_l(y)$ and $\mu_l(y)$ satisfies

$$\partial z_l / \partial\left(\omega^2\right) > 0,\ \partial z_l / \partial\left(k_x^2\right) < 0;\ z_l\left(0, k_x^2\right)_{k_x \neq 0} < 0\ (z_l(0,0) = 0), \tag{3.17}$$

hence its zeros $\omega_{\mathrm{f/f}}$ and poles $\omega_{\mathrm{f/c}}$ are strictly alternating and its overall shape mimics the 'tangent-like' function (2.8) describing a homogeneous layer. Dependence $z_l(\omega)$ at fixed $k_x \neq 0$ is outlined in Fig. 2.1.

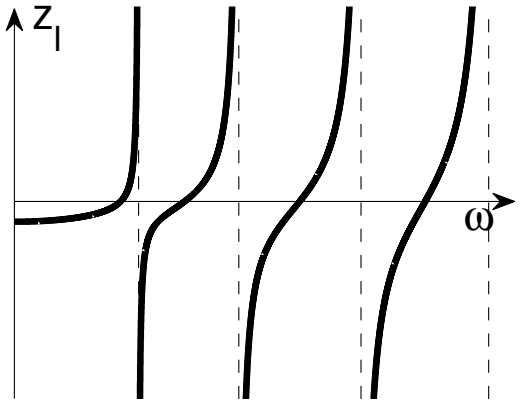

Figure 2.1: Shape of $z_l(\omega)$ at fixed $k_x \neq 0$.

2.3.2 Substrate impedances

For a substrate material with T-periodic $\rho_s(y)$ and $\mu_s(y)$, define the positive forms similar to (3.14) but now associated with each of the Floquet modes $\eta_\alpha(y)$ (2.9), namely,

$$\rho_s |u_\alpha|^2 = i(\eta_\alpha^+ \mathbf{T} \frac{\partial \eta_\alpha}{\partial(\omega^2)})', \ \mu_s |u_\alpha|^2 = -i(\eta_\alpha^+ \mathbf{T} \frac{\partial \eta_\alpha}{\partial(k_x^2)})'; \ \ \alpha = 1, 2. \tag{3.18}$$

Integrate both sides of (3.18) over the period $y \in [0, T]$, insert $(2.9)_2$, invoke the definition (2.10) of the impedances $Z_{s\alpha}(\omega^2, k_x^2)$ and consider them in the stopbands so that $Z_{s\alpha}$ are real. It thus follows that

$$\begin{gathered} \left\langle \rho_s |u_\alpha|^2 \right\rangle = \tfrac{i}{T}(|q_\alpha|^2 - 1)\mathbf{w}_\alpha^+ \mathbf{T} \tfrac{\partial \mathbf{w}_\alpha}{\partial(\omega^2)} = \tfrac{1}{T}(|q_\alpha|^2 - 1)\tfrac{\partial Z_{s\alpha}\left(\omega^2, k_x^2\right)}{\partial(\omega^2)} |a_\alpha|^2, \\ \left\langle \mu_s |u_\alpha|^2 \right\rangle = \ldots = \tfrac{1}{T}(1 - |q_\alpha|^2)\tfrac{\partial Z_{s\alpha}\left(\omega^2, k_x^2\right)}{\partial(k_x^2)} |a_\alpha|^2; \ \ \alpha = 1, 2, \end{gathered} \tag{3.19}$$

where $\langle \cdot \rangle$ denotes average across the period, see (2.5). It can also be shown, similarly to (3.16), that real $Z_{s\alpha}$ satisfy the identity

$$\frac{1}{T}(|q_\alpha|^2 - 1) Z_{s\alpha} |a_\alpha|^2 + \langle \mu_s |u_\alpha'|^2 \rangle + k_x^2 \langle \mu_s |u_\alpha|^2 \rangle = \omega^2 \langle \rho_s |u_\alpha|^2 \rangle, \ \ \alpha = 1, 2. \tag{3.20}$$

In particular, (3.20) is valid at any point $\omega = 0$, $k_x \neq 0$ (since it always lies a stopband, see §2.2.1).

By (3.19) and (3.20), the physical and non-physical impedances Z_{s1} and Z_{s2} associated with the decreasing $\alpha = 1$ and increasing $\alpha = 2$ Floquet modes ($|q_1| < 1 < |q_2|$) fulfil the inequalities

$$\begin{gathered} \partial Z_{s1}/\partial(\omega^2) < 0, \ \partial Z_{s2}/\partial(\omega^2) > 0; \ \partial Z_{s1}/\partial(k_x^2) > 0, \ \partial Z_{s2}/\partial(k_x^2) < 0; \\ Z_{s1}(0, k_x^2)_{k_x \neq 0} > 0, \ Z_{s2}(0, k_x^2)_{k_x \neq 0} < 0 \ \ (Z_{s\alpha}(0, 0) = 0), \end{gathered} \tag{3.21}$$

which specify at the band edges as

$$\partial Z_{s\alpha}/\partial\left(\omega^2\right),\ \partial Z_{s\alpha}/\partial\left(k_x^2\right)\to\pm\infty \text{ at } |q_\alpha|\to 1\quad(\alpha=1,2)\,. \tag{3.22}$$

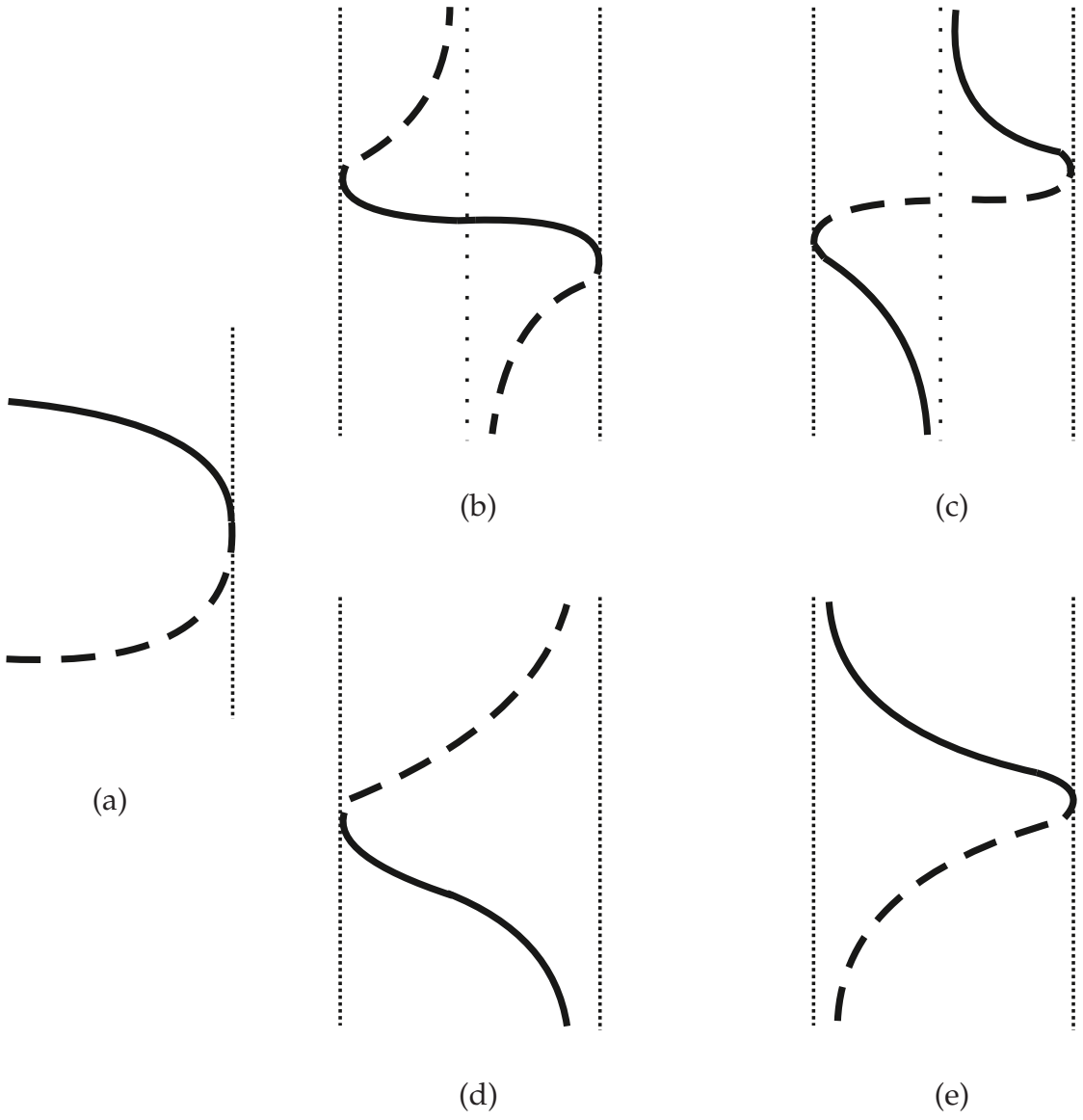

Figure 2.2: Possible shapes of $Z_{s\alpha}(\omega)$ at fixed k_x in the (a) first and (b,c) higher stopbands ($|\Delta|>1$) of a semi-infinite periodic substrate with an asymmetric profile and (d,e) with an even profile of $\rho_s(y)$, $\mu_s(y)$ on a period. Solid and dashed lines are used for the physical and non-physical impedances Z_{s1} and Z_{s2} associated with decreasing and increasing Floquet modes, respectively. Dotted lines indicate the stopband edges ($|\Delta|=1$) and asymptotes.

Adding into consideration the known properties of the Neumann and Dirichlet branches $\omega_N(k_x)$ and $\omega_D(k_x)$ which define zeros and poles of $Z_{s\alpha}$ (see §2.2.2), possible shapes of the curves $Z_{s\alpha}(\omega)$ occurring in the stopbands at fixed k_x are encompassed in Fig. 2.2. Recall that the first stopband (Fig. 2.2a) is a case apart, since it does not admit a Dirichlet solution ω_D and it disappears at $k_x = 0$ (see (2.12)). In order to embrace different options concisely, we do not fix zero mark of the axis $Z_{s\alpha}$ in Figs. 2.2a-c which thus imply that, generally, a single zero point ω_N of $Z_{s\alpha}$ within a given stopband may correspond to either decreasing $\alpha = 1$ or increasing $\alpha = 2$ mode (i.e. either $Z_{s1}(\omega_N) = 0$ or $Z_{s2}(\omega_N) = 0$) and may occur either before or after the pole (i.e. $\omega_N \lessgtr \omega_D$). The particular case where $\rho_s(y)$ and $\mu_s(y)$ are even on a period $[0, T]$ (see §2.2.2) is shown in Figs. 2.2d,e: here the pole ω_D (unless the first stopband) and zero ω_N coincide with the opposite edges of each stopband.

In conclusion, consider the transformation under which the profile $\rho_s(y)$, $\mu_s(y)$ of each period is 'symmetrically reflected' about the midline. It can be shown that such transformation amounts to interchanging the diagonal components of the monodromy matrix $\mathbf{M}(T, 0)$; see [49]. By (2.10), (2.11), this leads to the reciprocal identity

$$Z_{s1} = -\widetilde{Z}_{s2},\ Z_{s2} = -\widetilde{Z}_{s1} \tag{3.23}$$

between the impedances $Z_{s\alpha}$ and $\widetilde{Z}_{s\alpha}$ of any substrate and its 'symmetric reflection'. Note that (3.23) is consistent with the identity $Z_{s1} = -Z_{s2}$ for periodically even substrates, see Figs. 2.2d,e.

2.4 Love wave spectrum

2.4.1 Overview of the spectrum

The impedance properties established in §2.3 and delineated in Figs. 2.1, 2.2 are insightful for understanding the Love-wave spectrum $\{\omega_L(k_x)\}$. At any fixed k_x, the solutions ω_L of the dispersion equation (2.13) for Love waves can be identified graphically as intersections of the curves $z_l(\omega)$ and $Z_{s1}(\omega)$, while intersections of $z_l(\omega)$ with $Z_{s2}(\omega)$ define the solutions ω_{nL} for non-physical (increasing) Love wave. Allowing k_x to vary, it is evident from Figs. 2.1, 2.2 that branches of physical and non-physical solutions transform to each other when they meet the stopband edge. Thus the Love spectrum should generally include finite and semi-infinite branches $\omega_L(k_x)$ originating and/or terminating at cutoff points $k_x \neq 0$, where a branch $\omega_L(k_x)$ meets a band-edge curve $\omega_e(k_x)$ and pass on a non-physical branch $\omega_{nL}(k_x)$ (see examples in §2.5).

2.4.2 Number of Love waves per a stopband

It is seen from Figs. 2.1, 2.2 that, in contrast to a free substrate which does not admit more than a single SH surface wave per stopband, there is no such limitation for Love waves defined by intersections of z_l with Z_{s1}. The number of Love waves increases along with the number n of poles of $\omega_{\mathrm{f/c}}$ of z_l getting into the given stopband. To be specific, let us formulate a few statements in which Ω denotes the frequency interval of a stopband at fixed k_x.

1) Let the stopband Ω contain no poles of $z_l(\omega)$. Then there must be (i) none or one or two Love waves in Ω of the type plotted in Fig. 2.2b and (ii) none or one Love wave in Ω of all other types plotted in Fig. 2.2.

2) Let the stopband Ω contain $n = 1, 2, ...$ poles of $z_l(\omega)$. Then there must be (i) n or $n+1$ or $n+2$ Love waves in Ω of the type plotted in Fig. 2.2b, (ii) $n-1$ or n or $n+1$ Love waves

in Ω of the type plotted in Fig. 2.2c, and (iii) n or $n+1$ Love waves in Ω of other types plotted in Figs. 2.2a,c,d. Also note that there must be at least n non-physical solutions ω_{nL} in Ω of the type plotted in Fig. 2.2c and at least $n-1$ of them in Ω of other types plotted in Fig. 2.2.

These observations are evident from Figs. 2.1, 2.2 and can be proved analytically by noting that, according to (2.13) and (3.17), (3.21), the Love wave solutions ω_L are zeros of monotonic function $z_l(\omega) - Z_{s1}(\omega)$ and hence there is one and only one ω_L between each pair of poles of $z_l(\omega) - Z_{s1}(\omega)$ occurring inside Ω or at its edges. In other words, there is one Love wave in between two poles $\omega_{\mathrm{f/c}}$ of $z_l(\omega)$ in Ω unless they enclose ω_D realizing pole of Z_{s1} (Fig. 2.2b), in which case there are two Love waves in between such pair of $\omega_{\mathrm{f/c}}$.

Similar analysis basing on (3.17), (3.21) can be performed at fixed ω and varying k_x.

2.4.3 Monotonicity of the Love wave branches

Equations (2.13) and (3.17), (3.21) show that the Love branches $\omega_L(k_x)$ are monotonically increasing at $k_x \neq 0$. Using (3.15) and (3.19) yields the explicit identity

$$\frac{\mathrm{d}\omega_L^2}{\mathrm{d}(k_x^2)} = -\frac{\partial(z_l - Z_{s1})/\partial(k_x^2)}{\partial(z_l - Z_{s1})/\partial(\omega^2)} = \frac{(1-|q_1|^2)|a_1|^2\langle\mu_l M_1^2\rangle d + M_1^2(0,-d)\langle\mu_s|u_1|^2\rangle T}{(1-|q_1|^2)|a_1|^2\langle\rho_l M_1^2\rangle d + M_1^2(0,-d)\langle\rho_s|u_1|^2\rangle T} > 0, \tag{4.24}$$

where $|q_1|^2 < 1$. Expressing $\omega_L^2(k_x)$ from the system of equations $(3.16)_2$, (3.20) taken at $z_l = Z_{s1}$ and combining with (4.24) provides a similar identity for the velocity branches $v_L(k_x) = \omega_L(k_x)/k_x$ which shows that they are monotonically decreasing at $k_x \neq 0$:

$$k_x^2\frac{\mathrm{d}v_L^2}{\mathrm{d}(k_x^2)} = \frac{\mathrm{d}\omega_L^2}{\mathrm{d}(k_x^2)} - v_L^2 = -\frac{(1-|q_1|^2)|a_1|^2\langle\mu_l^{-1}M_3^2\rangle d + M_1^2(0,-d)\langle\mu_s|u_1'|^2\rangle T}{k_x^2\left[(1-|q_1|^2)|a_1|^2\langle\rho_l M_1^2\rangle d + M_1^2(0,-d)\langle\rho_s|u_1|^2\rangle T\right]} < 0. \tag{4.25}$$

The same consideration but with Z_{s2} and $|q_2|^2 > 1$ reveals that the branches $\omega_{nL}(k_x)$ and $v_{nL}(k_x)$ of non-physical Love solutions (the ones that involve the increasing Floquet mode

$\alpha = 2$) are generally *not* monotonic. The latter is in contrast to the case of a free periodic halfspace where both physical and non-physical SH surface waves are monotonic.

2.4.4 Lower bound of the Love wave spectrum

The velocity spectrum of Love waves $\{v_L(k_x)\} = \{\omega_L(k_x)\}/k_x$ has the lower bound

$$\{v_L(k_x)\} > \min\left(\min_{y\in[-d,0]} c_l(y), \min_{y\in[0,T]} c_s(y)\right). \tag{4.26}$$

Since the Love velocity branches $v_L(k_x)$ are decreasing (§2.4.2), the bound (4.26) should also be a common limit for those of them which extend up to $k_x \to \infty$ (i.e. do not switch to a non-physical branch).

The result (4.26) follows directly from the wave equation (2.1) and the auxiliary conditions of the Love-wave problem (§2.3), since the latter imply that the operator $(\mu u')'$ of (2.1) defined on $y \in [-d, \infty)$ is negative definite. The same conclusion is evident from the impedance approach whereby Figs. 2.1, 2.2 show that the dispersion equation $z_l = Z_{s1}$ can hold only if $\omega > \min\left(\omega^{(1)}_{\mathrm{f/f}}, \omega^{(1)}_N\right)$ which leads via (2.7) and (2.12) to (4.26).

Recall the meaning of $c(y) = \sqrt{\mu/\rho}$ as a local velocity of SH bulk mode. It is noteworthy to this end that if $\min c_s(y) < \min c_l(y)$ ($= c_l$ for a homogeneous layer), then (4.26) admits existence of the Love waves with $v_L(k_x) < \min c_l(y)$ which are thus slower than the slowest SH bulk mode in the layer (see Fig. 2.6b below). Such regime is ruled out for the case of a homogeneous substrate, i.e. for the classical Love waves.

2.4.5 Fundamental branch

The fundamental dispersion branch is understood as a (physical) branch with origin at zero ω and k_x. The Love spectrum may or may not contain such a branch. The criterion as to which is the case is based on the low-frequency long-wave asymptotics of z_l and $Z_{s\alpha}$. These can be found using the Peano series of the matricant $\mathbf{M} = \mathbf{I} + \int \mathbf{Q} + \int\int \mathbf{QQ} + ...$

(see [51]) with $\mathbf{Q}$ given by (2.2). From (2.6), it readily follows that

$$z_l = -k_x^2 d\left(\langle\mu_l\rangle - \langle\rho_l\rangle v^2\right) + O\left(k_x^4 d^3\right), \tag{4.27}$$

where d is the layer thickness. To obtain $Z_{s\alpha}$, we first note that $\mathrm{trace}\mathbf{M}(T,0) = 2 + F(v)\kappa^2 + ...$ hence the eigenvalues q_α and eigenvectors $\mathbf{w}_\alpha$ of $\mathbf{M}(T,0)$ expand as

$$\begin{gathered} q_\alpha = 1 \mp \sqrt{F(v)}\kappa + \tfrac{1}{2}F(v)\kappa^2 + O(\kappa^3), \\ \mathbf{w}_\alpha \parallel \begin{pmatrix} -iT\langle\mu_s^{-1}\rangle + O(\kappa^2) \\ \pm\kappa\sqrt{F(v)} + \kappa^2\left(J(v) - \frac{1}{2}F(v)\right) + O(\kappa^3) \end{pmatrix}, \end{gathered} \tag{4.28}$$

and thus, from (2.10) with (4.28),

$$Z_{s\alpha} = \frac{1}{T\langle\mu_s^{-1}\rangle}\left[\pm\kappa\sqrt{F(v)} + \kappa^2\left(J(v) - \frac{1}{2}F(v)\right) + O\left(\kappa^3\right)\right],\ \alpha = 1,2. \tag{4.29}$$

The notations used above are $\kappa = k_x T,\ F(v) = \langle\rho_s\rangle\langle\mu_s^{-1}\rangle(\bar{c}_s^2 - v^2)$ and

$$\begin{gathered} J(v) = \frac{1}{T^2}\int_0^T \mu_s^{-1}\int_0^y (\mu_s - \rho_s v^2)\,\mathrm{d}y\mathrm{d}y_1 = \\ \frac{1}{T^2}\sum_{j=1}^n\sum_{k=1}^j \left(1 - \frac{1}{2}\delta_{jk}\right)\mu_j^{-1}(\mu_k - \rho_k v^2)\,d_j d_k, \end{gathered} \tag{4.30}$$

where $(4.30)_2$ is specialized for the case of a piecewise homogeneous substrate whose period consists of n layers with constant $\rho_j,\ \mu_j$ and thickness $d_j,\ j = 1..n$. The upper and lower signs in (4.28), (4.29) correspond to the decreasing $\alpha = 1$ and increasing $\alpha = 2$ modes, respectively (cf. (3.21)).

Denote the Love fundamental branch by $\omega_L^{(1)}(k_x) = v_L^{(1)}(k_x)\,k_x$. By definition, it must start at the point $\omega = 0,\ k_x = 0$ as a physical branch extending into the first stopband $[0, \omega_e^{(1)})$ (where its extent may be finite, i.e. it may transform into non-physical branch due to meeting the band-edge $\omega_e^{(1)}$ at $k_x \neq 0$). Consider the dispersion equation $z_l = Z_{s1}$ (2.13) with (4.27) and (4.29). The quasistatic limit gives $F(v^2) = 0$ and hence $v_L^{(1)}(0) = \bar{c}_s$

(the same follows from (4.24) at $\omega, k_x \to 0$). Taking into account the next-order terms, we arrive at the following conclusion:

$$\text{if } C = d\left(\frac{\langle\rho_l\rangle}{\langle\rho_s\rangle} - \frac{\langle\mu_l\rangle}{\langle\mu_s\rangle}\right) - T\frac{J\left(\bar{c}_s\right)}{\langle\mu_s\rangle\left\langle\mu_s^{-1}\right\rangle} \text{ is positive } (C > 0), \tag{4.31}$$

then there exists the Love fundamental branch and its long-wave onset is described by the formula

$$v_L^{(1)}\left(k_x\right) = \bar{c}_s\left[1 - \tfrac{1}{2}\left\langle\mu_s\right\rangle\left\langle\mu_s^{-1}\right\rangle C^2 k_x^2 + O\left(k_x^4\right)\right] \text{ with } \bar{c}_s^2 = \langle\mu_s\rangle/\langle\rho_s\rangle. \tag{4.32}$$

If, alternatively, $C < 0$ then no physical branch emerges from zero of ω, k_x and hence the Love spectrum has no fundamental branch. In fact what happens at $C < 0$ is that now the same quasistatic velocity value $v = \bar{c}_s$ gives rise to a non-physical Love branch $v_{nL}^{(1)}\left(k_x\right)$ defined by the equation $z_l = Z_{s2}$. Inserting (4.29) with lower sign gives the asymptotics of $v_{nL}^{(1)}\left(k_x\right)$ described by the same right-hand side of (4.32). Thus, the point $\omega = 0$, $k_x = 0$ always gives rise to velocity branch with long-wave onset (4.32) which is physical at $C > 0$ and non-physical at $C < 0$.

2.5 Numerical examples

As a typical example, consider a periodically bilayered substrate. Assume the W-Al substrate $y \geqslant 0$ consisting of equidistant layers of W and Al materials, so that T-periodic ρ_s, μ_s are equal to $\rho_1 \equiv \rho_{\mathrm{W}}$, $\mu_1 \equiv \mu_{\mathrm{W}}$ at $y \in [0, T/2]$ and to $\rho_2 \equiv \rho_{\mathrm{Al}}$, $\mu_2 \equiv \mu_{\mathrm{Al}}$ at $y \in [T/2, T]$ (see Table 1). Explicit form of the monodromy matrix $\mathbf{M}\left(T, 0\right)$ through a bilayered unit

cell $[0, T]$ is well-known:

$$\begin{aligned}\mathbf{M}(T,0) &= \mathbf{M}(T,T/2)\mathbf{M}(T/2,0)\\ &= \begin{pmatrix} \cos_1 & -\frac{i}{\mu_1 k_{y_1}}\sin_1 \\ -i\mu_1 k_{y_1}\sin_1 & \cos_1 \end{pmatrix}\begin{pmatrix} \cos_2 & -\frac{i}{\mu_2 k_{y_2}}\sin_2 \\ -i\mu_2 k_{y_2}\sin_2 & \cos_2 \end{pmatrix}\\ &= \begin{pmatrix} \cos_1\cos_2 - \frac{\mu_2 k_{y_2}}{\mu_1 k_{y_1}}\sin_1\sin_2 & -i(\frac{1}{\mu_1 k_{y_1}}\sin_1\cos_2 + \frac{1}{\mu_2 k_{y_2}}\cos_1\sin_2) \\ -i(\mu_1 k_{y_1}\sin_1\cos_2 + \mu_2 k_{y_2}\cos_1\sin_2) & \cos_1\cos_2 - \frac{\mu_1 k_{y_1}}{\mu_2 k_{y_2}}\sin_1\sin_2 \end{pmatrix},\end{aligned} \tag{5.33}$$

where we denote $\cos_j \equiv \cos(\frac{k_{y_j}T}{2})$ and $\sin_j \equiv \sin(\frac{k_{y_j}T}{2})$ with wave numbers $k_{y_j} = \sqrt{\frac{\rho_j}{\mu_j}\omega^2 - k_x^2}$ and $j = 1, 2$. Plugging $\mathbf{M}(T, 0)$ in (2.4) and (2.11) defines the passband and stopband areas (shaded and blanc in the subsequent figures) and the impedances $Z_{s\alpha}$.

According to [49], the inequalities $(\rho\mu)_{\mathrm{W}} > (\rho\mu)_{\mathrm{Al}}$ and $(\rho/\mu)_{\mathrm{W}} > (\rho/\mu)_{\mathrm{Al}}$ suffice to conclude that the SH surface waves in the free W-Al substrate terminated by the W layer are restricted to the narrow range $c_{\mathrm{W}} < \omega/k_x < c_{\mathrm{Al}}$ and there is no surface waves elsewhere. This is observed in Fig. 2.3 where zeros of impedance $Z_{s\alpha}$ and hence the dispersion branches are all non-physical $\omega/k_x > c_{\mathrm{Al}}$. The effect of coating this substrate by Ag layer is demonstrated in Fig. 2.4. In particular, it is seen that even a very thin coating creates branches of physical (localised) waves, the reason being evident from the graphical display of dispersion equation $z_l = Z_{s1}$ on right-hand panel. Note also that the thicker coating the more disconnected Love branches appear in the spectrum, see Fig. 2.4c.

Table 1. Material properties used in calculations

	W	Al	Ag	Si
ρ, g/cm^3	19.32	2.73	10.64	2.33
μ, GPa	160.2	26.1	33.7	79.6
c, mm/μs	2.88	3.09	1.78	5.85

Let Al-W substrate be a semi-infinite structure of the same W and Al layers as above but terminated by the Al layer. The W-Al and Al-W substrates have the same pass-

band/stopband spectrum while their impedances satisfy the reciprocity identity (3.23), as observed on comparing the right-hand panels of Figs. 2.4 and 2.5. This impedance reciprocity underlies the different configuration of the Love branches of the W-Al and Al-W substrates with the same Ag coating, see Figs 2.4b,c and 2.5a,b.

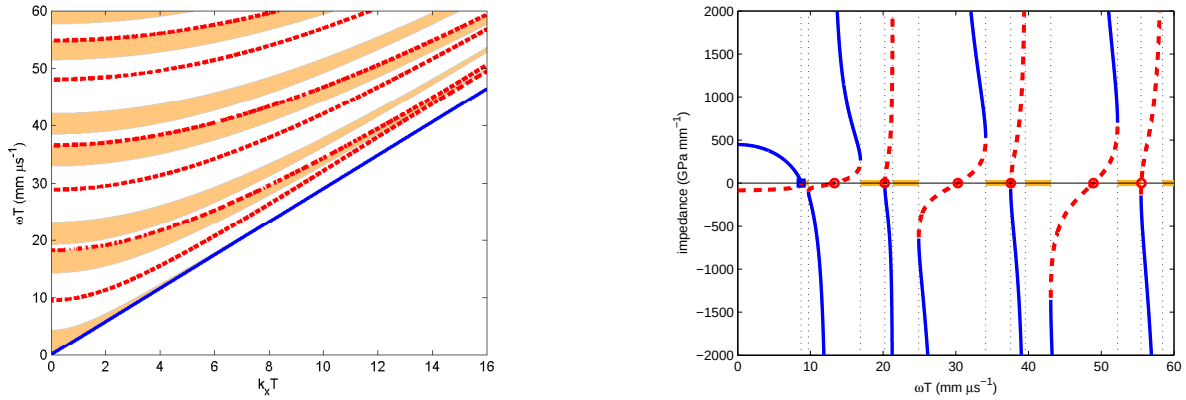

Figure 2.3: SH waves in the uncoated W-Al substrate. The left-hand diagram shows the dispersion spectrum where the fundamental branch is physical (solid line) and all upper branches are non-physical (dashed lines). Passband areas are shaded, stopband areas are blanc. The right-hand diagram shows the physical and non-physical impedances $Z_{s1}(\omega)$ and $Z_{s2}(\omega)$ (solid and dashed lines, like in Fig. 2.2) at fixed $k_xT = 3$. Shaded segments indicate passbands.

A complementary perspective based on the slowness $s = k/\omega$ is presented in Fig. 2.6. The slowness spectrum of the uncoated W-Al substrate where all supersonic branches $s(\omega)$ are non-physical (Fig. 2.6a corresponding to Fig. 2.3) is compared to the spectra $s(\omega)$ of the given substrate with relatively slow coating (Ag) and fast coating (Si), Figs. 2.6b and 2.6c. To this end, Fig. 2.6c shows the case of "isospeed coating" which implies taking the top W layer of the W-Al substrate to be thicker then all others. It is seen that such perturbation also gives rise to the branches of localised waves in the supersonic domain $s < c_{\mathrm{Al}}^{-1}$ where they cannot exist in the case of perfectly periodic W-Al substrate (cf. Fig. 2.3).

Note that the existence of the fundamental Love branch in Figs. 2.4, 2.5, 2.6b and its non-existence in Figs. 2.6c,d is correctly predicted by the sign of coefficient C defined in

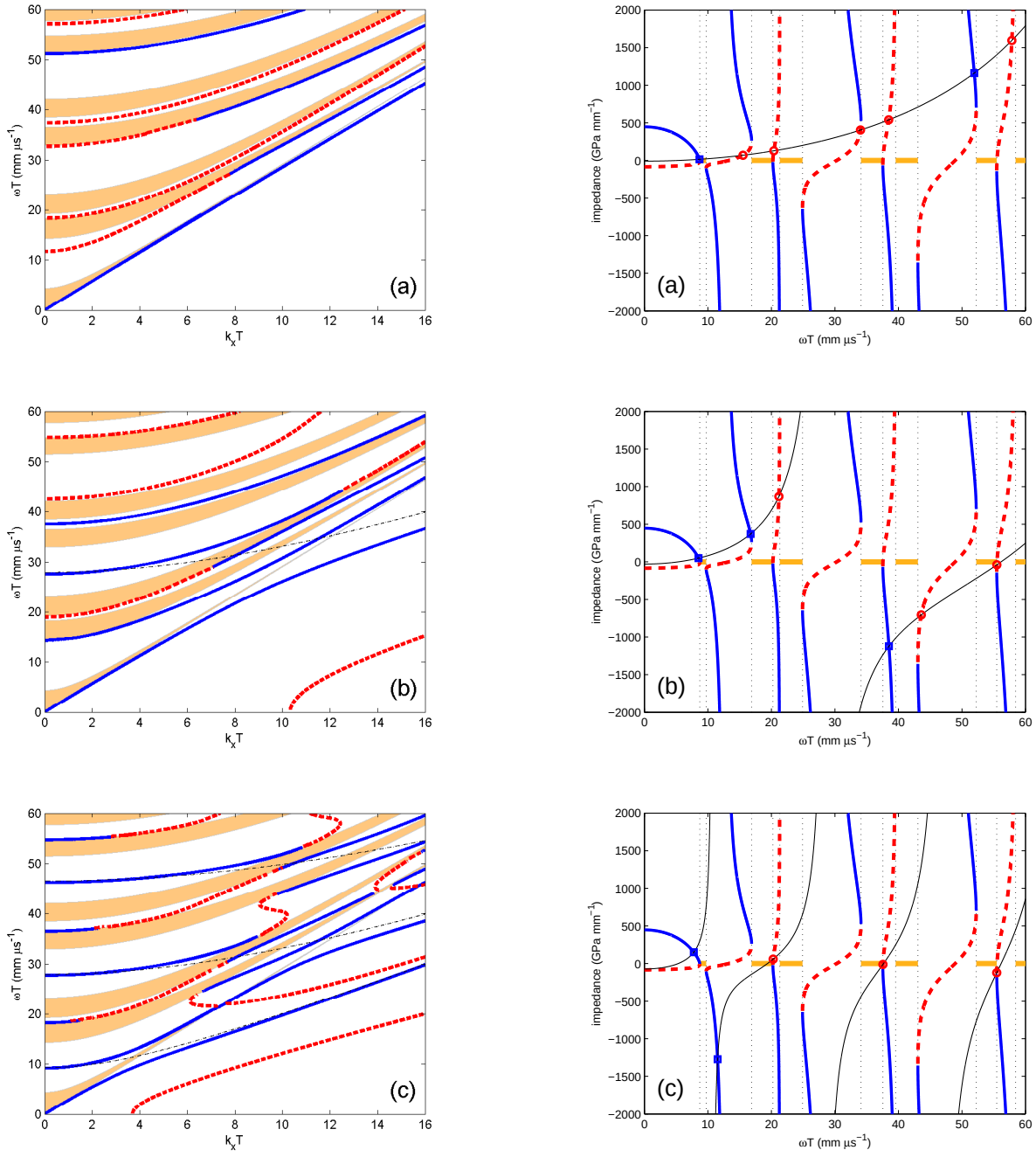

Figure 2.4: Love waves in the W-Al substrate coated by the Ag layer of thickness $d/T = 0.03$ (a), 0.1 (b) and 0.3 (c). The left-hand diagrams show physical and non-physical branches $\omega_L(k_x)$ and $\omega_{nL}(k_x)$ (solid and dashed lines, respectively). Thin line traces the pole of the coating layer impedance z_l. The right-hand diagrams show the substrate impedances $Z_{s\alpha}(\omega)$ (see Fig. 3) and the Ag layer impedance $z_l(\omega)$ (2.8) (thin solid line) at fixed $k_xT = 3$: their intersections are the roots ω_L and ω_{nL} (marked by squares and circles).

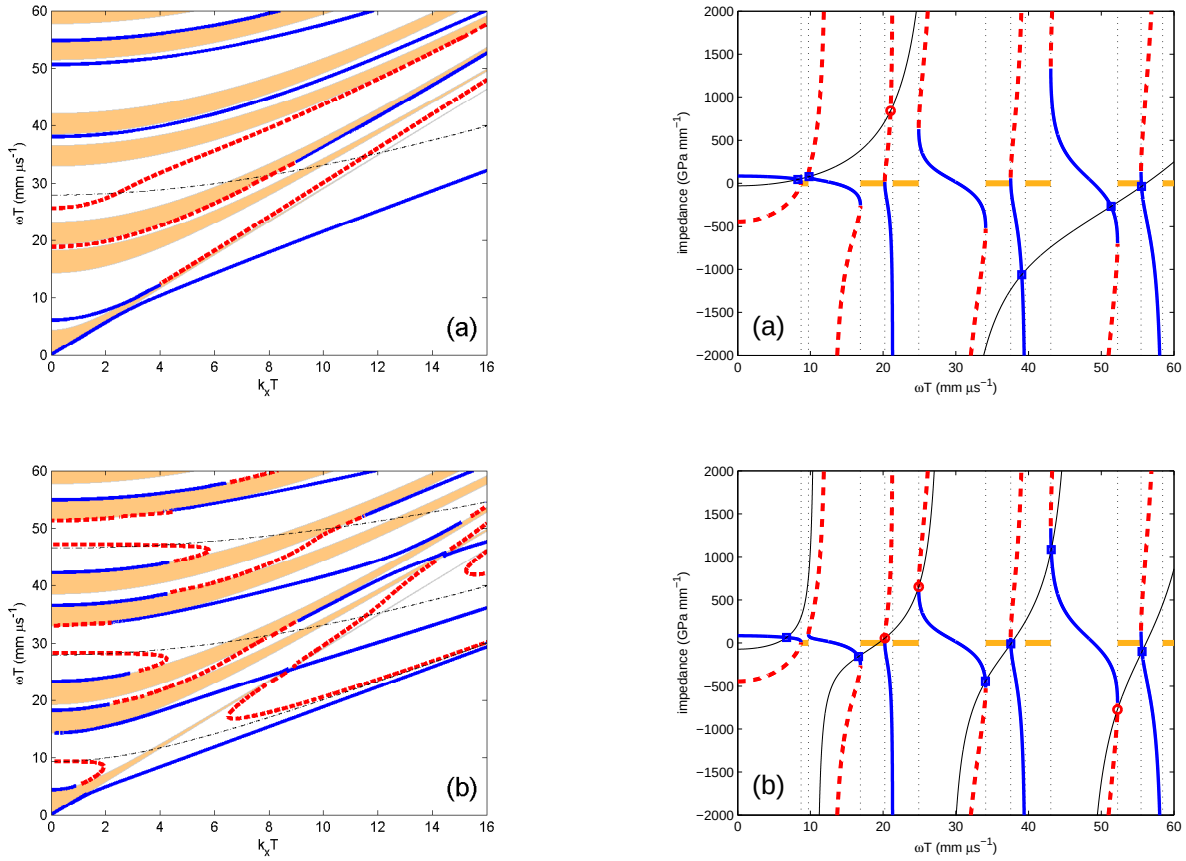

Figure 2.5: Love waves in the Al-W substrate coated by the Ag layer of thickness $d/T = 0.1$ (a) and 0.3 (b). The notations are the same as in Fig. 2.4.

(4.31) (with $d_1 = d_2 = T/2$ and $\langle \rho_l \rangle$, $\langle \mu_l \rangle$ being ρ, μ of Ag, Si or W for the corresponding cases in hand).

Finally consider the example of functionally graded materials. Numerical implementation of this case is based on the calculation of multiplicative integral defining the matricant $\mathbf{M}$, see (2.3). Assume a constant density $\rho_l = \rho_s = 1$ g/cm^3, denote $c_0 = 2$ mm/μs, and let the velocity profiles be $c_s(y) = c_0(1 - 0.65y/T)$ for the unit cell $y \in [0, T]$ of a piecewise continuous periodic substrate and $c_l(y) = (c_0/2)(1 + y/2d)$ for the coating layer $y \in [-d, 0]$ of thickness $d = T$. It was mentioned among other examples in [49] that a free periodic substrate with the above profile $c_s(y)$ disallows SH surface waves everywhere beyond a very narrow range of values of $\omega/k_x \approx c_0$ (see Fig. 4c of [49]). In this regard, emergence of extended branches of Love waves in the same substrate with coating (Fig.

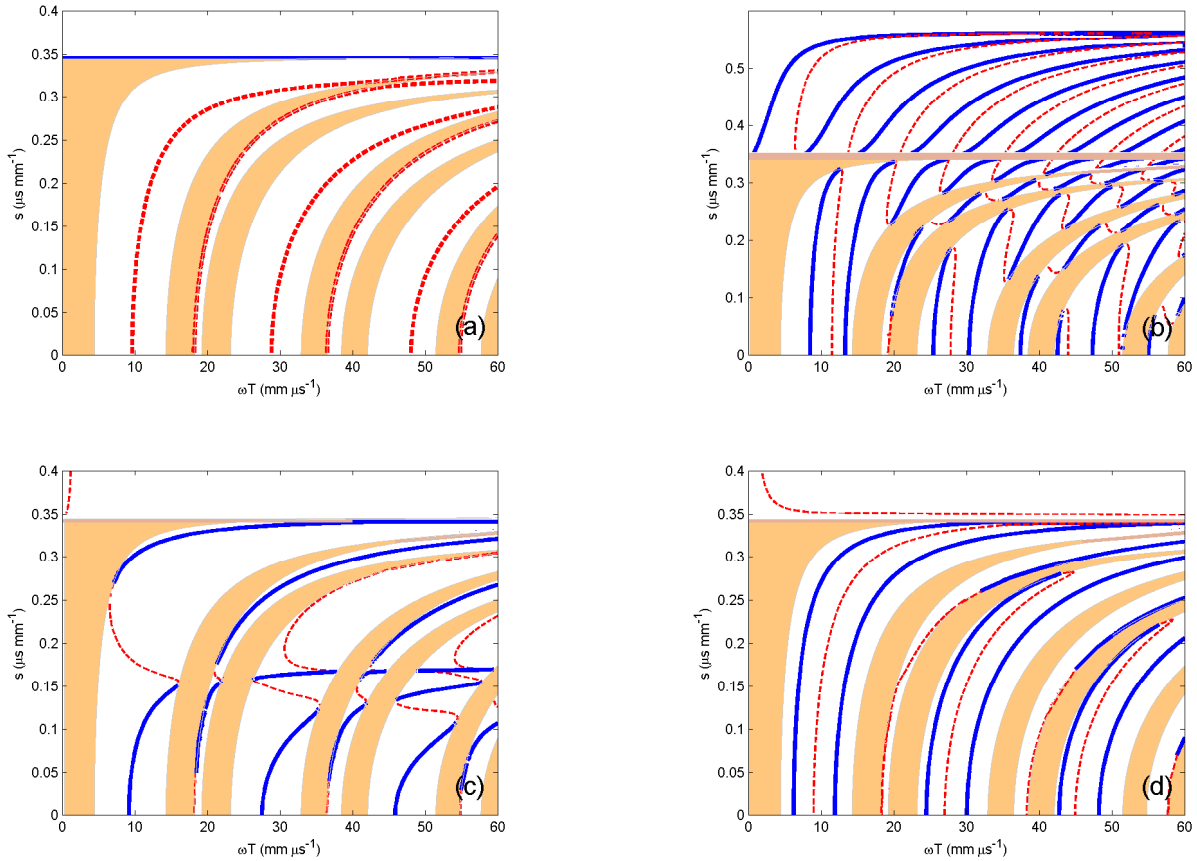

Figure 2.6: Slowness spectra $s(\omega)$ of SH waves (a) and Love waves (b-c) in the W-Al substrate without coating (a) and with $d/T = 1$ thick coating layer of Ag (b) and of Si (c), and with the top W layer being thicker than all others by $d/T = 1$ (d). As in the previous figures, passband and stopband areas are shaded and blanc, and physical and non-physical branches are solid and dashed, respectively.

2.7) demonstrates a prominent spectral effect of the coating.

2.6 Conclusion

Dispersion spectrum of SH Love waves in a coated periodic substrate has been studied. It is in many ways different from the classical case of coated homogeneous substrates. For instance, a periodic substrate admits localised waves emerging with finite frequencies at $k_x = 0$. Interestingly, their existence can essentially ramify the long-wave limit of transient problem comparatively to the case of classical Love waves (see [53]). Love waves in a

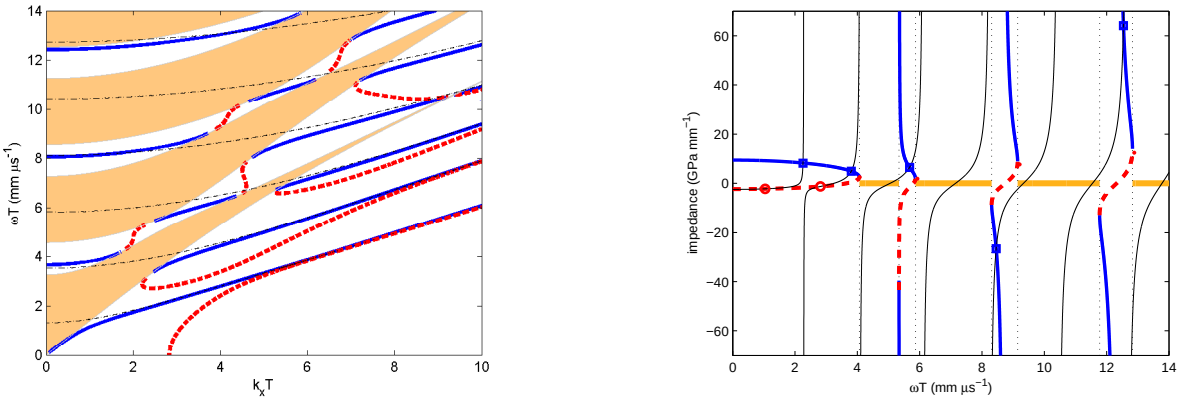

Figure 2.7: Love waves in the periodic functionally graded substrate coated by the functionally graded layer (their velocity profiles are given in the text). The right-hand diagram shows the impedances $Z_{s\alpha}(\omega)$ and $z_l(\omega)$ at fixed $k_x T = 3$. The notations are the same as in Fig. 2.4.

coated periodic substrate can also differ a lot from the SH surface waves in the same periodic substrate without coating. There is a general dissimilarity between these types of waves, which is that any stopband at fixed k_x cannot contain more than one SH surface wave whereas it may contain several Love waves (about as many, as many resonances of the coating layer fall within this stopband). Another significant effect of coating arises in a fairly typical case where a free periodic substrate admits SH surface waves only in a narrow velocity range - then even a weak perturbation by thin coating creates localised waves in the spectral domain where they could not exist for the uncoated substrate.

The methodology and results of this chapter can have useful implications. The impedance formalism can be appropriately adapted to the case of vector waves in a coated periodic substrate and/or in a periodic medium with different models of an embedded defect layer; see e.g. [10].

Chapter 3

Love waves for a 2D laterally periodic layer on a substrate

3.1 Introduction

Among various configurations following the pioneer work [54], the case of 2D periodic coating on a uniform substrate has recently been introduced and studied, see Refs. [11]-[21]. With the exception of Ref. [19], all these papers have been concerned with depth-independent coatings formed by periodically distributed finite pillars or holes. At the same time, no results seem to have been reported for the SH waves in the case of 2D depth-dependent coating and/or substrate. This situation is similar to the case of surface waves in a 2D periodic half-space in that the calculation for the depth-dependent structures is notably more involved.

In this Chapter we consider again the Love waves, but this time we let the SH waves propagate in the 2D depth-dependent coating layer on a substrate. More precisely, the layer consists of the laterally periodic roads parallel to the surface and the substrate can either be of the similar 2D structure or it can be uniform.

In contrast to Refs [11]-[21] which all used the finite element method, a new analyti-

cal approach of calculating the dispersion spectrum called the resolvent method is presented. Within this approach, the dispersion equation is formulated via the resolvent $\mathbf{R}_l$ of the layer and the spectral projector $\mathbf{P}_d$ on the decreasing ('physical') modes in the substrate. The projector is defined by the resolvent $\mathbf{R}_s$ through the unit cell of the substrate. The dispersion equation is stable, since $\mathbf{R}$ provides a numerically stable substitute of the unstable propagator $\mathbf{M}$. The advantage of using the resolvent is that it is, like the propagator $\mathbf{M}$, Fourier expanded only in lateral coordinate and keeps the exact integration in depth coordinate. Therefore the resolvent method gives a good accuracy and efficiency due to the smaller size of the input matrix of coefficients of the governing system of equations ($O(N)$ instead of $O(N^2)$ for PWE, where N is the number of Fourier harmonics). The advantage of using the spectral projector is that it extracts the decreasing ('physical') modes by accessing the spectrum of the propagator directly without solving the eigenvalue problem and without invoking several unit cells like in the supercell method. By these means, we calculate the subsonic spectrum of the Love waves for a 2D laterally periodic depth-dependent coating layer on a uniform or 2D periodic substrate.

The main motivation is to model low-frequency band gaps inside the Brillouin zone. Coating is chosen so that it provides multiple subsonic branches.

3.2 Problem statement

Consider an 2D elastically isotropic medium consisting of a half-space $\{\mathbf{x} = (x_1, x_2) : x_2 \geqslant 0\}$ coated by a layer $x_2 \in [-d, 0]$. We recall that the axes $X_1,\ X_2,\ X_3$ are introduced so that x_2 is the thickness coordinate. We assume that the medium is uniform along one of the lateral directions, which is taken as the axis X_3, periodic along the other lateral axis X_1 and generally heterogeneous along the thickness axis X_2. The halfspace and layer materials may be 2D periodic or not but at least the layer is laterally periodic (along X_1). A typical example is a uniform half-space coated by a layer composed of infinite bars

embedded into matrix material along the axis X_3, ; see Figs. 3.1a, 3.3a. The periodicity here is due to the 2D inclusions (bars). Denote the lateral period by T_1. For brevity, let $T_1 = 1$.

The medium is uniform along X_3 and hence yields uncoupled SH wave with the displacement $v_3(\mathbf{x}, t) = v(\mathbf{x})e^{-i\omega t}$. The problem consists of the scalar wave equation

$$\partial_1(\mu\partial_1 v) + \partial_2(\mu\partial_2 v) = -\rho\omega^2 v \tag{2.1}$$

with the traction-free boundary condition at the surface and the radiation condition into the depth given by

$$\partial_2 v \mid_{x_2=-d} = 0, \ \lim_{x_2\to\infty} v = 0, \tag{2.2}$$

where $\partial_i = \partial/\partial x_i$. The shear coefficient $\mu(\mathbf{x})$ and the density $\rho(\mathbf{x})$ are 1-periodic in x_1. Hence the function $v(\mathbf{x})$ satisfies the Floquet-Bloch form

$$v(\mathbf{x}) = u(\mathbf{x})e^{ik_1x_1}, \tag{2.3}$$

where $u(\mathbf{x})$ is 1-periodic in x_1 and $k_1 \in [-\pi, \pi]$ is the wave number lying in the Brillouin zone. Using (2.3), the wave equation (2.1) can be rewritten as

$$(\partial_1 + ik_1)\mu(\partial_1 + ik_1)u + \partial_2(\mu\partial_2 u) = -\rho\omega^2 u. \tag{2.4}$$

Next, we apply the Fourier series expansion to the functions μ, ρ and u which are 1-periodic in x_1:

$$\begin{gathered} f(\mathbf{x}) = \sum_{m=-\infty}^{\infty} \widehat{f}_m(x_2)e^{2\pi imx_1} \\ \text{with } \widehat{f}_m(x_2) = \int_{-1/2}^{1/2} f(\mathbf{x})e^{-2\pi imx_1}dx_1 \ \text{ for } f = \mu, \rho, u. \end{gathered} \tag{2.5}$$

As a result of the plane wave expansion in x_1, the partial differential equation (2.4) takes

the form of a system of ordinary differential equations in x_2, namely,

$$-(\boldsymbol{\partial}_1 + k_1)\boldsymbol{\mu}(\boldsymbol{\partial}_1 + k_1)\mathbf{u} + \partial_2(\boldsymbol{\mu}\partial_2\mathbf{u}) = -\boldsymbol{\rho}\omega^2\mathbf{u} \tag{2.6}$$

with the matrices and vector of Fourier coefficients

$$\begin{gathered}\boldsymbol{\mu}(x_2) = (\widehat{\mu}_{n-m}(x_2)),\ \boldsymbol{\rho}(x_2) = (\widehat{\rho}_{n-m}(x_2)),\\ \boldsymbol{\partial}_1 = \operatorname{diag}(2\pi m)\ \text{ and }\ \mathbf{u}(x_2) = (\widehat{u}_m(x_2)),\ \ n, m \in \mathbb{Z}.\end{gathered} \tag{2.7}$$

In practice all matrices and vectors are truncated by the number N of plane modes, so we have $(2N+1)\times(2N+1)$-matrices with $n, m \in [-N, N]$ in (2.7).

Finally, we recast the system (2.6) of differential equations of second order as the double-size system of differential equations of first order. Taking into account (2.2), this gives the initial value problem

$$\partial_2\boldsymbol{\eta} = \mathbf{Q}\boldsymbol{\eta},\ \ \boldsymbol{\eta}(-d) = \begin{pmatrix}\mathbf{u}(-d)\\ \mathbf{0}\end{pmatrix} \tag{2.8}$$

with the condition

$$\lim_{x_2\to\infty}\boldsymbol{\eta}(x_2) = 0. \tag{2.9}$$

Here we denote[1]

$$\boldsymbol{\eta} = \begin{pmatrix}\mathbf{u}\\ \boldsymbol{\mu}\partial_2\mathbf{u}\end{pmatrix},\quad \mathbf{Q} = \begin{pmatrix}\mathbf{0} & \boldsymbol{\mu}^{-1}\\ (\boldsymbol{\partial}_1 + k_1)\boldsymbol{\mu}(\boldsymbol{\partial}_1 + k_1) - \boldsymbol{\rho}\omega^2 & \mathbf{0}\end{pmatrix}. \tag{2.10}$$

In contrast to the plane wave expansion method (PWE), the expansion here has been applied along one coordinate only, while an exact integration is performed along the other

[1] In the 2D case, for numerical convenience we define $\boldsymbol{\eta}$ and $\mathbf{Q}$ without additional factor of the imaginary unit i in contrast to their conventional definition (2.2) in the 1D case. We also use here $x_1,\ x_2$ coordinates instead of, respectively, $x,\ y$ coordinates of the 1D case.

coordinate. This leads to a better accuracy of our method in comparison to the PWE.

3.3 The resolvent

The first-order differential system (2.8) with the initial condition has a unique solution provided by the propagator $\mathbf{M}$ via

$$\boldsymbol{\eta}(x_2) = \mathbf{M}(x_2, -d)\boldsymbol{\eta}(-d), \tag{3.11}$$

where the propagator $\mathbf{M}(b, a)$ satisfies

$$\partial_2 \mathbf{M} = \mathbf{Q}\mathbf{M}, \;\; \mathbf{M}(a, a) = \mathbf{I}, \tag{3.12}$$

as (2.8) implies.

However, recall that $\mathbf{M}$ for 2D is of $2(2N+1) \times 2(2N+1)$ size with large N. As a result the direct calculation of the propagator $\mathbf{M}$ via (3.12) is hindered by numerical instabilities due to exponential growth of $\mathbf{M}$ with growing N (see Appendix B). The key idea is to replace the propagator $\mathbf{M}$ with its resolvent

$$\mathbf{R}_z(b, a) = (z\mathbf{I} - \mathbf{M}(b, a))^{-1} \;\; (\text{for any fixed } z \in \mathbb{C} \setminus \operatorname{spec} \mathbf{M}), \tag{3.13}$$

which grows only linearly with growing N (see Appendix B). For brevity we will omit index $_z$. The condition $z \notin \operatorname{spec} \mathbf{M}(b, a)$ is fulfilled via taking any randomly chosen z far enough from the unit circle and the real axis. The differential equation for the resolvent $\mathbf{R}(x_2, a)$ is derived from the differential equation (3.12) for the propagator $\mathbf{M}(x_2, a)$ in the following way. Using the identity $\mathbf{A}' = -\mathbf{A}(\mathbf{A}^{-1})'\mathbf{A}$ which holds for any matrix $\mathbf{A}$ with

$\det \mathbf{A} \neq 0$, we obtain by $(\mathbf{R}^{-1})' = -\mathbf{QM}$ the equality

$$\partial_2 \mathbf{R} = \mathbf{RQMR}. \tag{3.14}$$

Note the identity

$$\mathbf{MR} = z\mathbf{R} - \mathbf{I} \tag{3.15}$$

derived from the resolvent definition (3.13) as $\mathbf{R}^{-1}\mathbf{R} = z\mathbf{R} - \mathbf{MR}$. Inserting (3.15) in (3.14) yields the Riccati differential equation

$$\partial_2 \mathbf{R} = \mathbf{RQ}(z\mathbf{R} - \mathbf{I}), \;\; \mathbf{R}(a, a) = \frac{1}{z-1}\,\mathbf{I}. \tag{3.16}$$

The resolvent $\mathbf{R}(x_2, a)$ can be computed as a root of (3.16) by standard numerical means such as the Runge-Kutta method. At the same time, if we have a partially uniform medium, there is a more efficient way of computation (see Appendix C for more details). First of all, the unit cell may be partitioned in several horizontal sublayers parallel to x_1 and then the overall resolvent $\mathbf{R}$ can be expressed via $\mathbf{R}_j$ of each sublayer according to the special chain rule. The point is that the calculation of $\mathbf{R}_j$ of each horizontal sublayer may be simplified depending on the type of this sublayer. If the sublayer is uniform along x_1 and x_2, then $\mathbf{R}_j$ can be evaluated explicitly. If the sublayer is heterogeneous along x_1 but uniform along x_2 (the system matrix $\mathbf{Q}_j$ is constant), then $\mathbf{R}_j$ can be calculated as a function of the matrix $\mathbf{Q}_j$. It is only in the general case, where the sublayer is heterogeneous along both x_1 and x_2, that we have to use that $\mathbf{R}_j$ satisfies the Riccati equation and hence can be computed by the Runge-Kutta method.

3.4 The spectral projector

To extract the waves fulfilling the radiation condition in a half-space (substrate), we apply the spectral projector (see [42] and [51]). A spectral projector $\mathbf{P}$ is a mathematical tool to distinguish the eigenvectors by means of the corresponding eigenvalues. It makes use of the location of the eigenvalues on the complex plane, whereas their explicit value is not necessary. In this section, we introduce the spectral projector for our problem, whereas the methods of its numerical implementation are detailed in Appendix C. In particular, we discuss there the case of a uniform or depth-independent substrate, where the system matrix $\mathbf{Q}_{\mathrm{sub}}$ is constant and the projector is found directly from $\mathbf{Q}_{\mathrm{sub}}$ bypassing $\mathbf{M}_{\mathrm{sub}}$.

3.4.1 The eigenspaces

Denote the eigenvalues and eigenvectors of the substrate propagator $\mathbf{M}_{\mathrm{sub}} \equiv \mathbf{M}_{\mathrm{sub}}(T_2, 0)$ over the period T_2 along the depth coordinate x_2 by $q_j \in \mathbb{C}$ and $\boldsymbol{w}_j$ with $1 \leqslant j \leqslant 2(2N+1)$. The wave field $\boldsymbol{\eta}(0)$ at the interface $x_2 = 0$ can be expressed as the superposition of the eigenvectors $\mathbf{w}_j$, i.e.

$$\boldsymbol{\eta}(0) = \sum_{j=1}^{2(2N+1)} \alpha_j \boldsymbol{w}_j, \;\; \alpha_j \in \mathbb{C}. \tag{4.17}$$

Hence any solution $\boldsymbol{\eta}(x_2)$ in the depth of the periodic structure is

$$\boldsymbol{\eta}(x_2) = \boldsymbol{\eta}(nT_2 + \widetilde{x}_2) = \mathbf{M}_{\mathrm{sub}}(\widetilde{x}_2, 0)\mathbf{M}_{\mathrm{sub}}^n \boldsymbol{\eta}(0) = \sum_{j=1}^{2(2N+1)} \alpha_j q_j^n \mathbf{M}_{\mathrm{sub}}(\widetilde{x}_2, 0)\boldsymbol{w}_j, \tag{4.18}$$

where $n \in \mathbb{Z}$ and $\widetilde{x}_2 \in [0, T_2)$. It is seen that $\boldsymbol{\eta}(x_2)$ is purely decreasing, increasing or propagating (bounded) in the depth of the substrate $n \to \infty$ iff the initial wave field $\boldsymbol{\eta}(0)$ consists only of the eigenvectors $\boldsymbol{w}_j$ with $|q_j| < 1$, $|q_j| > 1$ or $|q_j| = 1$, respectively. Let us state this in terms of the spans of eigenvectors of $\mathbf{M}_{\mathrm{sub}}$ and then define the projectors.

The full eigenspace of $\mathbf{M}_{\text{sub}}$, i.e.

$$E = \text{span}\{\boldsymbol{w} : \mathbf{M}_{\text{sub}}\boldsymbol{w} = q\boldsymbol{w} \text{ with } q \in \mathbb{C}\} = \mathbb{C}^{2(2N+1)}, \tag{4.19}$$

comprises the wave fields $\boldsymbol{w} = \boldsymbol{\eta}(0)$ giving rise to all types of behavior into the depth of the substrates. The subspace of E_d giving rise to decreasing modes is identified through the corresponding eigenvalues as

$$E_d := \text{span}\{\boldsymbol{w} : \mathbf{M}_{\text{sub}}\boldsymbol{w} = q\boldsymbol{w}, |q| < 1\}. \tag{4.20}$$

For brevity we will call the wave fields $\boldsymbol{w} = \boldsymbol{\eta}(0) \in E_d$ as simply decreasing modes (omitting 'giving rise to') in the sense that

$$\lim_{x_2 \to \infty} \boldsymbol{\eta}(x_2) = 0 \text{ iff } \boldsymbol{\eta}(0) \in E_d. \tag{4.21}$$

Similarly we define the subspaces E_i and E_p of the increasing and propagating modes as follows

$$E_i := \text{span}\{\boldsymbol{w} : \mathbf{M}_{\text{sub}}\boldsymbol{w} = q\boldsymbol{w}, |q| > 1\}, \tag{4.22}$$

$$E_p := \text{span}\{\boldsymbol{w} : \mathbf{M}_{\text{sub}}\boldsymbol{w} = q\boldsymbol{w}, |q| = 1\}. \tag{4.23}$$

Thus any wave field $\boldsymbol{w} \in E$ at the interface can be decomposed in a unique way into a sum of purely decreasing $\boldsymbol{w}_d$, increasing $\boldsymbol{w}_i$ and propagating $\boldsymbol{w}_p$ modes:

$$E = E_d + E_i + E_p \Rightarrow \boldsymbol{w} = \boldsymbol{w}_d + \boldsymbol{w}_i + \boldsymbol{w}_p \text{ with } \boldsymbol{w}_\gamma \in E_\gamma. \tag{4.24}$$

3.4.2 The spectral projector definition via propagator eigenvalues

Given the unique decomposition (4.24) of E into E_d, E_i and E_p, we can define the spectral projector as a map onto a corresponding subspace of the form

$$\mathbf{P}_\gamma \boldsymbol{w} = \boldsymbol{w}_\gamma,\ \mathbf{P}_\gamma : E \to E_\gamma,\ \text{ with } \gamma = d, i, p. \tag{4.25}$$

To define the spectral projector explicitly, we use the definitions (4.20), (4.22) and (4.23) of the E_γ in terms of the propagator eigenvalues q_j. This gives the definition

$$\boldsymbol{w} \in E_\gamma \ \Leftrightarrow\ \mathbf{P}_\gamma \boldsymbol{w} = \boldsymbol{w} \ \text{ with } \gamma = d, i, p \tag{4.26}$$

Hence, (4.25) and (4.26) together give

$$\mathbf{P}_\gamma^2 \boldsymbol{w} = \mathbf{P}_\gamma \boldsymbol{w}_\gamma = \boldsymbol{w}_\gamma = \mathbf{P}_\gamma \boldsymbol{w} \ \text{ with } \gamma = d, i, p, \tag{4.27}$$

which amounts to

$$\mathbf{P}_\gamma^2 = \mathbf{P}_\gamma \ \text{ with } \gamma = d, i, p. \tag{4.28}$$

The identity (4.28) proves that the eigenvalues p_j of $\mathbf{P}_\gamma$ satisfy $p_j^2 = p_j$ and take therefore either zero or unit values. Hence

$$\dim E_\gamma = \operatorname{trace} \mathbf{P}_\gamma. \tag{4.29}$$

Moreover, equations (4.24) and (4.25), (4.26) yield the following identity

$$\mathbf{P}_d + \mathbf{P}_p + \mathbf{P}_i = \mathbf{I}. \tag{4.30}$$

3.4.3 The alternative definition of the spectral projector via path integral

Projector as a function counting the required modes is defined by counting the resolvent poles inside a corresponding path. That is, the spectral projector $\mathbf{P}_d$ extracts the decreasing modes as the integral over a path, which is given by a circle smaller but close enough to the unite circle:

$$\mathbf{P}_d = \frac{1}{2\pi i}\oint_{|z|=1-0} \mathbf{R}_z dz, \tag{4.31}$$

where $\mathbf{R}_z = (z\mathbf{I} - \mathbf{M}_{\text{sub}})^{-1}$ is the substrate resolvent over a period. Here we select the eigenvalues of the propagator placed inside this closed path applying the Cauchy integral theorem (at the third equality):

$$\mathbf{P}_d \boldsymbol{w}_j = \frac{1}{2\pi i}\oint_{|z|=1-0} (z\mathbf{I} - \mathbf{M}_{sub})^{-1} dz \boldsymbol{w}_j = \frac{1}{2\pi i}\oint_{|z|=1-0} (z-q_j)^{-1} dz \boldsymbol{w}_j = \begin{cases} \boldsymbol{w}_j, & |q_j| < 1 \\ \mathbf{0}, & \text{elsewhere} \end{cases}. \tag{4.32}$$

Similarly to (4.31), $\mathbf{P}_p$ and $\mathbf{P}_i = \mathbf{I} - \mathbf{P}_d - \mathbf{P}_p$ are given by the path integrals close to the unit circle:

$$\mathbf{P}_p = \frac{1}{2\pi i}\left(\oint_{|z|=1+0} - \oint_{|z|=1-0}\right)\mathbf{R}_z dz \text{ and } \mathbf{P}_i = \mathbf{I} - \frac{1}{2\pi i}\oint_{|z|=1+0} \mathbf{R}_z dz. \tag{4.33}$$

3.5 The dispersion equation

The spectrum is given by the localized waves spectrum and the propagative waves spectrum.

3.5.1 Love wave spectrum

The solution at the interface is defined via the layer propagator (indicated by the subscript l):

$$\boldsymbol{\eta}(0) = \mathbf{M}_l \boldsymbol{\eta}(-d). \tag{5.34}$$

By the continuity of traction and displacement at the interface $x_2 = 0$ and the radiation condition $\lim_{x_2 \to \infty} \boldsymbol{\eta}(x_2) = 0$ at $x_2 \to \infty$, the solution is selected then via projector due to its decreasing behavior into the depth of the substrate:

$$\mathbf{P}_d \boldsymbol{\eta}(0) = \boldsymbol{\eta}(0). \tag{5.35}$$

Taking into the account traction-free boundary condition at $x_2 = -d$, i.e. $\boldsymbol{\eta}(-d) = (\mathbf{u}(-d), \mathbf{0})^T$, (5.34) and (5.35) give the dispersion equation in the form

$$\exists \mathbf{u}_0 \neq \mathbf{0} : \ (\mathbf{P}_d - \mathbf{I}) \mathbf{M}_l \begin{pmatrix} \mathbf{u}_0 \\ \mathbf{0} \end{pmatrix} = \mathbf{0}. \tag{5.36}$$

However (5.36) is numerically unstable due to the instability of the propagator (recall § 3.3). The key idea in this regard is to restate the identity (5.36) in terms of the product (see (3.15))

$$\mathbf{M}_l \mathbf{R}_l = z \mathbf{R}_l - \mathbf{I}, \tag{5.37}$$

which is numerically stable. Therefore our ansatz is to define the solution $\mathbf{u}_0$ at the surface in terms of the numerically stable resolvent $\mathbf{R}_l$ of the layer, i.e.

$$\begin{pmatrix} \mathbf{u}_0 \\ \mathbf{0} \end{pmatrix} = \mathbf{R}_l \begin{pmatrix} \mathbf{v}_0 \\ \widetilde{\mathbf{v}}_0 \end{pmatrix} \tag{5.38}$$

for some $\mathbf{v}_0,\ \widetilde{\mathbf{v}}_0$. From (5.38), it follows that

$$\widetilde{\mathbf{v}}_0 = -\mathbf{R}_{l4}^{-1}\mathbf{R}_{l3}\mathbf{v}_0, \tag{5.39}$$

where $\mathbf{R}_{l3}$ is the bottom left and $\mathbf{R}_{l4}$ is the bottom right blocks of $\mathbf{R}_l$. Note here that the inversion $\mathbf{R}_{l4}^{-1}$ of the resolvent block is numerically stable in contrast to the inversion of other two blocks $\mathbf{R}_{l2}^{-1}$ and $\mathbf{R}_{l3}^{-1}$; see explicit formulas in the Appendix B. Hence (5.37) and (5.39) together imply

$$\mathbf{M}_l \begin{pmatrix} \mathbf{u}_0 \\ \mathbf{0} \end{pmatrix} = \mathbf{M}_l\mathbf{R}_l \begin{pmatrix} \mathbf{v}_0 \\ \widetilde{\mathbf{v}}_0 \end{pmatrix} = (z\mathbf{R}_l - \mathbf{I}) \begin{pmatrix} \mathbf{I} \\ -\mathbf{R}_{l4}^{-1}\mathbf{R}_{l3} \end{pmatrix} \mathbf{v}_0. \tag{5.40}$$

Finally, inserting (5.40) in (5.36) yields

$$\begin{gathered} \exists \mathbf{v}_0 \neq \mathbf{0} :\ \mathbf{D}\mathbf{v}_0 = \mathbf{0} \\ \text{with}\ \ \mathbf{D} = (\mathbf{P}_d - \mathbf{I})(z\mathbf{R}_l - \mathbf{I}) \begin{pmatrix} -\mathbf{I} \\ \mathbf{R}_{l4}^{-1}\mathbf{R}_{l3} \end{pmatrix}. \end{gathered} \tag{5.41}$$

Since $\mathbf{D}$ is not a square matrix, we arrive at

$$\det \mathbf{D}^*\mathbf{D} = 0 \tag{5.42}$$

as the dispersion equation, where * hereafter means Hermitian conjugation. However the determinant of a large size square matrix is a numerically unstable object due to the large eigenvalues possibly presented even at its zero points. A stable calculation of its zeros can be ensured by the estimation of a minimal eigenvalue of the matrix. The Love wave

spectrum is therefore given in stable terms by

$$\lambda_{\min}(\mathbf{D}^*\mathbf{D}) = 0, \tag{5.43}$$

where $\lambda_{\min}(\cdot)$ is the minimal eigenvalue of the positive definite matrix in the brackets. The method based on eq. (5.43) provides fast and stable calculation for any configuration.

3.5.2 Projection of the spectrum of the propagating waves

The propagating wave spectrum (also called the Floquet spectrum) of a substrate is given by the Floquet eigenvalues $\omega(k_1, k_2)$ with $k_1, k_2 \in [-\pi, \pi]^2$ corresponding to the propagating modes and given by the identity $q(\omega, k_1) = e^{ik_2}$, where q is some eigenvalue of $\mathbf{M}_{\text{sub}}$.

We calculate the projection of the dispersion surface $\omega(k_1, k_2)$ on the plane (ω, k_1) in terms of the projector $\mathbf{P}_p$ on propagating modes. As follows from the projector definition (see (4.29)), its trace indicates the number $N_p(\omega, k_1)$ of the propagating modes, i.e.

$$N_p(\omega, k_1) = \operatorname{trace} \mathbf{P}_p. \tag{5.44}$$

Therefore, we determine the projections of the propagative spectra of the substrate at a given ω and k_1 by the condition

$$N_p(\omega, k_1) \geqslant 1. \tag{5.45}$$

However it is preferable to calculate the projection of the propagative spectra in terms of $\mathbf{P}_d$, since the latter is anyway calculated to obtain the localized spectrum (5.41). We utilize (5.45) with

$$N_p(\omega, k_1) = 2(2N + 1) - 2 \operatorname{trace} \mathbf{P}_d. \tag{5.46}$$

Equation (5.46) follows from (5.44) and the identity (A.2.10$_3$). Note that the number of

propagating modes therefore is always even.

3.6 Numerical examples

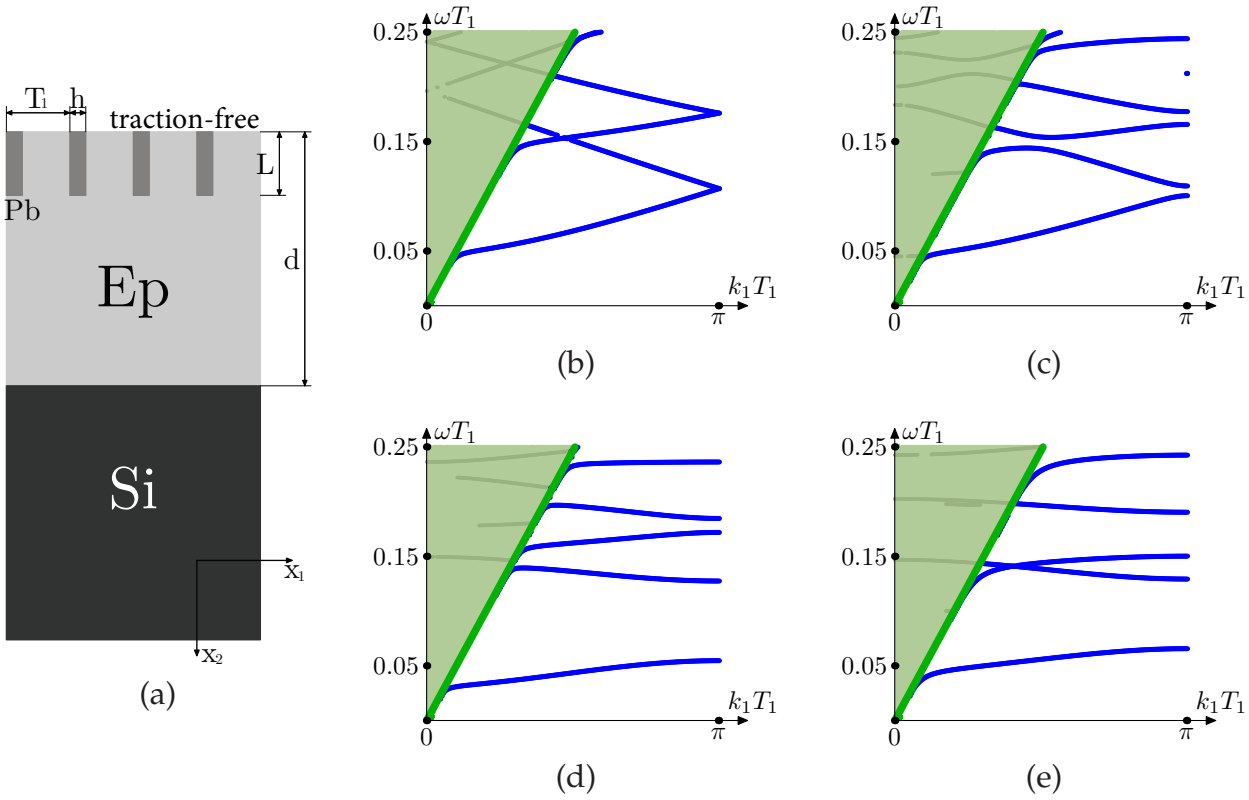

Figure 3.1: (a) Layer with laterally periodic depth-dependent baffles on the uniform substrate. (b) $L = 0$: reference (unperturbed) subsonic spectrum formally folded with respect to the subsequently imposed period T_1. Spectra for (c) $L = 0.1$; (d) $L = 3.5$; (e) $L = 6$. Shaded area bounded by the sound line of the substrate (Si) contains leaky branches (grey lines). The values of ωT_1 are in mm/μs.

We provide several numerical examples. To begin with, consider the perturbation by thin laterally periodic baffles of Pb ($\rho = 11.6$ g/cm^3, $\mu = 14.9$ GPa) embedded in the coating layer of epoxy ($\rho = 1.142$ g/cm^3, $\mu = 1.482$ GPa) lying on the uniform substrate of Si ($\rho = 2.33$ g/cm^3, $\mu = 79.9$ GPa), see Fig. 3.1a. The geometrical parameters are $T_1 = 1$ mm, $d = 6$ mm, and $h = 0.2$ mm. The layer depth to the horizontal period ratio d/T_1 is taken to be large enough to enable possibility to move inclusions up and down in the

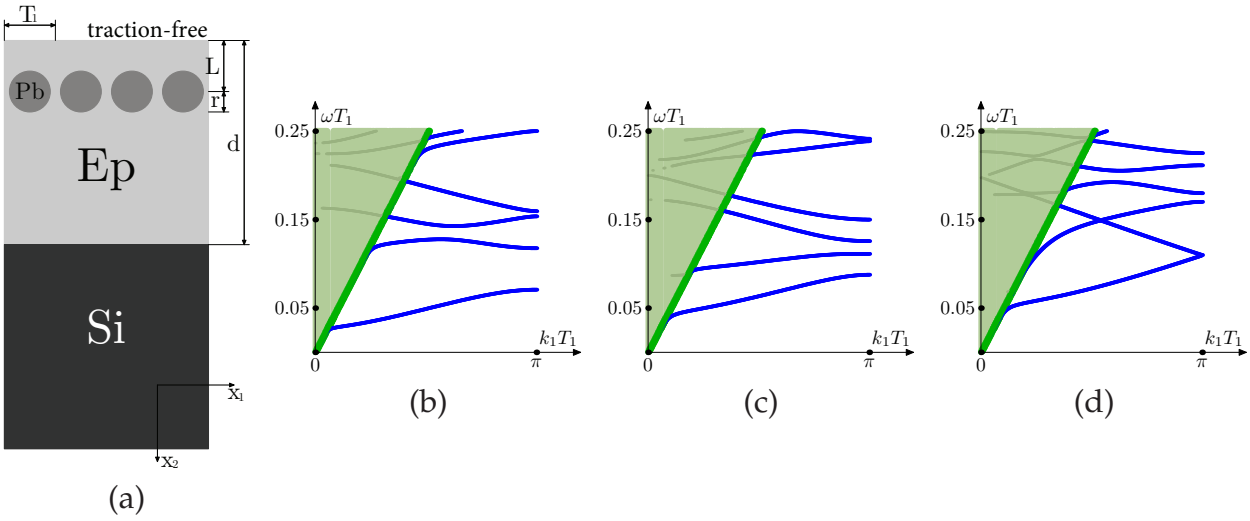

Figure 3.2: (a) Layer with laterally periodic cylindrical inclusions on the uniform substrate. Spectra for (b) $L = 0.5$ mm (c) $L = 4.5$ mm (d) $L = 5.5$ mm.

layer. The formally folded (unperturbed) spectrum is displayed in Fig. 3.1b. It is obtained from the 1D laterally homogeneous case by formal imposition of the periodic condition along the lateral coordinate. Figures 3.1c-e show that any considered perturbation creates band gaps at the edge of the Brillouin zone; at the same time, the low-frequency band gap, arising inside the Brillouin zone due to repulsion of the second and third dispersion branches, depends on the length L of the baffles: the gap opens up at $L > 0$ and closes at $L \gtrapprox 5.5$ mm. Note that a similar effect of the branch repulsion due to the laterally periodic loading has been discussed in Refs. [55] and [56]. It is seen from Fig. 2.2b that the upper branches either originate from the sound line (the Sezawa branches) or arise due to the folding at the edge of the Brillouin zone. The branches which initially arise from the folding tend to continue into the radiative region as the leaky branches, see Figs. 3.1c-e. Leaky branches are computed by adding one of the propagating modes into the projector $\mathbf{P}_d$ that formally corresponds to taking integral (4.31) along the closed contour half of which is $|z| = 1 + 0$ and the other half is $|z| = 1 - 0$. Real part of the leaky wave frequency is computed approximately, under the condition $\lambda_{\min} < 10^{-3}$, see eq. (5.43).

As another example, consider again a coating layer of epoxy on the uniform substrate

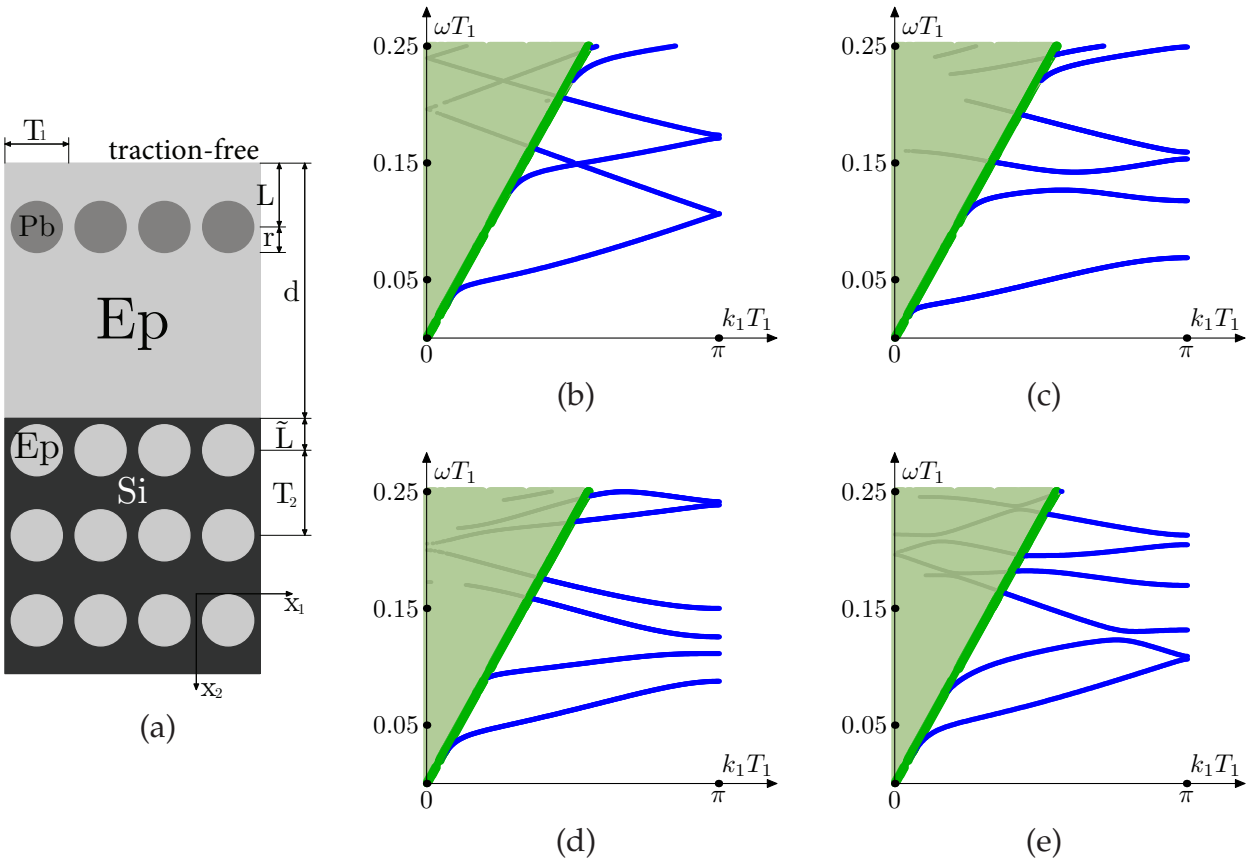

Figure 3.3: (a) Layer with laterally periodic cylindrical inclusions on the substrate with 2D periodic cylindrical inclusions. Spectra for (b) the uniform coating layer (c) $L = 0.5$ mm (d) $L = 4.5$ mm (e) $L = 5.5$ mm. Shaded area is bounded by the sound line which corresponds to the effective speed of the Si/Epoxy substrate along x_1.

of Si and assume now that the layer contains laterally periodic cylindrical inclusions of Pb with the radius $r = 0.45$ mm, see Fig. 3.2a. Let the inclusions move away from the surface towards the interface. The two formerly intersecting dispersion branches repulse each other (Figs. 3.2b,c) until the inclusions reach the interface which fact leads to the abrupt closure of the low-frequency gaps both at the edge and inside the Brillouin zone, see Figs. 3.2d. Upper branches give rise to the leaky branches above the sound line, similarly as in Fig. 3.1.

Next we demonstrate a similar evolution in the case where not only the layer but also the substrate contains cylindrical inclusions (epoxy; $T_2 = 3$ mm, $\widetilde{L} = 0.5$ mm). Let the inclusions in the layer move towards the interface. Only a little difference is observed

between the spectra in Figs. 3.2b-d and Figs. 3.3c-e (except that there remains a narrow gap inside the Brillouin zone in Fig. 3.3e that is in contrast to Fig. 3.2d). This may be related to the fact that the Love wave is localized mainly in the layer and so the 2D periodicity of the substrate does not matter that much. To highlight this point, we present the subsonic spectrum for a 2D periodic substrate coated by a thick uniform layer, Fig. 3.3b. It is seen that this spectrum is perfectly similar to the initial unperturbed spectrum for a uniform substrate, cf. Fig. 3.1b.

3.7 Conclusion

The original method of calculation of the dispersion spectra has been proposed which proves to be efficient and versatile, i.e. applicable to any configuration of 2D solid/solid PC layer on a substrate. To state a dispersion equation, the two main steps are to carry the initial solution through the layer and then to identify the solution at the interface as a solution decreasing into the depth of the substrate. Both steps follow in terms of the layer and substrate resolvents $\mathbf{R}_l$ and $\mathbf{R}_s$, since the large size propagator matrices $\mathbf{M}_l$ and $\mathbf{M}_s$ are numerically unstable. First we substitute $\mathbf{R}_l$ instead of $\mathbf{M}_l$. We consider a new initial solution $\widetilde{\boldsymbol{\eta}}(-d)$ on the traction-free surface premultiplied by $\mathbf{R}_l$, i.e. $\boldsymbol{\eta}(-d) = \mathbf{R}_l\widetilde{\boldsymbol{\eta}}(-d)$. The premultiplied solution gives a numerically stable propagated solution $\mathbf{M}_l\boldsymbol{\eta} = \mathbf{M}_l\mathbf{R}_l\widetilde{\boldsymbol{\eta}}$, since the product $\mathbf{M}_l\mathbf{R}_l = z\mathbf{R}_l - \mathbf{I}$ expressed in terms of the resolvent is numerically stable. Secondly, we qualify the solution $\boldsymbol{\eta}(0)$ at the interface between the layer and the substrate as a decreasing solution by applying the projector $\mathbf{P}_d$ on the decreasing modes. The solution is decreasing iff. $\boldsymbol{\eta}(0) = \mathbf{P}_d\boldsymbol{\eta}(0)$. That is, a projector can be considered as a kind of filter maintaining only the chosen kind of waves (e.g. decreasing) and rejecting the rest. Moreover, the projection of the spectrum of the propagating waves on the plane (ω, k_1) is also given by the projector, more precisely by $\mathrm{trace}\,\mathbf{P}_d$.

We have presented subsonic spectra of Love SH waves in 2D phononic crystals, where

either the coating or the substrate or both are laterally periodic, heterogeneous along two in-plane directions and uniform along the out-of-plane direction. It is demonstrated that the intersection of the folded subsonic branches inside the Brillouin zone is likely to break up provided that the laterally periodic inclusion in the coating is depth dependent and is deposited close enough to its free surface whereas the substrate may stay either 2D periodic or uniform. The low-frequency band gaps are the bigger, the closer are the inclusions to the traction-free surface and the bigger are the inclusions themselves.

Chapter 4

Plate waves in a free 2D laterally periodic plate

4.1 Introduction

The recent studies treating a broad variety of plate structures (depth-independent, depth-dependent and so on) are restricted to a limited number of numerical means such as the finite element method, supercell method or plane wave expansion.

We propose here the resolvent method for the 2D PC plate. The starting point is the dispersion equation written via $2(2N+1) \times 2(2N+1)$ propagator $\mathbf{M}$ through the unit cell (the monodromy matrix) which is obtained by PWE in lateral coordinate x_1 and exact integration in depth coordinate x_2. This formulation is, however, not satisfactory, since $\mathbf{M}$ grows exponentially at growing N. In this regard, the dispersion equation is easily recast in terms of the resolvent $\mathbf{R} = (z\mathbf{I} - \mathbf{M})^{-1}$, which is numerically stable at a growing N.

Another aspect of the study in this Chapter is concerned with symmetric/antisymmetric dispersion branches. We prove that if the profile of the unit cell is mirror symmetric with

respect to the horizontal midplane, then the dispersion spectrum splits into uncoupled symmetric and antisymmetric branches which can intersect with each other. Asymmetric perturbation of the profile breaks up these intersections and thus creates band gaps inside the Brillouin zone.

We model the absolute low-frequency band gaps. The plate width is taken bigger than the horizontal period, i.e. $d > T_1$, in order to allow the intersection of the dispersion branches for a uniform plate (considered formally as periodic) at a lowest possible frequency inside the Brillouin zone. Different geometries and material properties are considered to analyze their influence on the stopband/passband pattern.

Finally, the displacement and traction fields are recast in terms of the initial field and two resolvents, the resolvent taken at the corresponding depth of the plate and the resolvent through the rest of the plate.

4.2 Problem statement

Consider 2D PC laterally periodic plate of thickness d with traction-free faces. Similarly as for the structure in Chapter 3, we assume that the plate is uniform along one of the lateral directions, e.g. X_3, periodic along the other lateral axis X_1 and generally heterogeneous along the thickness axis X_2. A typical example is a plate composed of infinite bars embedded into matrix material along the axis X_3.

Since the plate is uniform along X_3, it admits propagation of the SH wave with the displacement $v_3(\mathbf{x}, t) = v(\mathbf{x})e^{-i\omega t}$ parallel to X_3. The problem consists of the scalar wave equation

$$\partial_1(\mu\partial_1 v) + \partial_2(\mu\partial_2 v) = -\rho\omega^2 v \tag{2.1}$$

with the traction-free boundary conditions at the upper and lower faces given by

$$\partial_2 v \mid_{x_2=0} = 0,\ \partial_2 v \mid_{x_2=d} = 0, \tag{2.2}$$

where $\partial_i = \partial/\partial x_i$. The shear coefficient $\mu(\mathbf{x})$ and the density $\rho(\mathbf{x})$ are 1-periodic in x_1. Hence the function $v(x)$ satisfies the Floquet-Bloch form (2.3). Similarly as in §3.2, we apply the plane wave expansion in x_1 and recast the system of differential equations of second order as the double-size system of differential equations of first order (cf. $(2.8)_1$)

$$\partial_2 \boldsymbol{\eta} = \mathbf{Q}\boldsymbol{\eta} \tag{2.3}$$

with the boundary conditions

$$\boldsymbol{\eta}(0) = \begin{pmatrix} \mathbf{u}_0 \\ \mathbf{0} \end{pmatrix}, \quad \boldsymbol{\eta}(d) = \begin{pmatrix} \widetilde{\mathbf{u}}_0 \\ \mathbf{0} \end{pmatrix}. \tag{2.4}$$

Here we have $\boldsymbol{\eta} = (\mathbf{u},\ \boldsymbol{\mu}\partial_2\mathbf{u})^T$ and $\mathbf{Q}$ given by (2.10) in terms of the Fourier coefficients (2.7); see §3.2.

4.3 The dispersion equation in terms of the propagator

The first-order differential system of the form (2.3) with the initial condition (2.4) has a unique solution provided by the propagator M via

$$\boldsymbol{\eta}(x_2) = \mathbf{M}(x_2, 0)\boldsymbol{\eta}(0). \tag{3.5}$$

Therefore (3.5) and (2.4) lead to the identity

$$\mathbf{M}(d, 0) \begin{pmatrix} \mathbf{u}_0 \\ \mathbf{0} \end{pmatrix} = \begin{pmatrix} \widetilde{\mathbf{u}}_0 \\ \mathbf{0} \end{pmatrix}, \tag{3.6}$$

which gives

$$\mathbf{M}_3(d, 0)\mathbf{u}_0 = \mathbf{0} \tag{3.7}$$

with $\mathbf{M}_3$ denoting the left lower block of $\mathbf{M}$. Hence the dispersion equation for the free plate takes the well known form

$$\det \mathbf{M}_3(d,0) = 0. \tag{3.8}$$

However, direct calculation of the propagator $\mathbf{M}$ via (3.12) is hindered by numerical instabilities due to exponential growth of $\mathbf{M}$ with the growing number of Fourier harmonics N (see Appendix B). So the standard dispersion equation (3.8) should be restated in terms of the resolvent which is numerically stable.

4.4 The dispersion equation in terms of the resolvent

Now we state the dispersion equation in stable terms. From (3.6) it follows that

$$(z\mathbf{I} - \mathbf{M}(d,0)) \begin{pmatrix} \mathbf{u}_0 \\ \mathbf{0} \end{pmatrix} = \begin{pmatrix} z\mathbf{u}_0 - \widetilde{\mathbf{u}}_0 \\ \mathbf{0} \end{pmatrix} \tag{4.9}$$

and therefore by the definition (3.13) of the resolvent we have

$$\begin{pmatrix} \mathbf{u}_0 \\ \mathbf{0} \end{pmatrix} = \mathbf{R}(d,0) \begin{pmatrix} z\mathbf{u}_0 - \widetilde{\mathbf{u}}_0 \\ \mathbf{0} \end{pmatrix}. \tag{4.10}$$

This gives

$$\mathbf{R}_3(d,0)(z\mathbf{u}_0 - \widetilde{\mathbf{u}}_0) = \mathbf{0} \tag{4.11}$$

with $\mathbf{R}_3$ denoting the left lower block of the matrix $\mathbf{R}$. Hence we arrive at

$$\det \mathbf{R}_3(d,0) = 0 \tag{4.12}$$

instead of (3.8) as dispersion equation. Similarly as in § 3.7.1, eq. (4.12) is recast as

$$\lambda_{\min}(\mathbf{R}_3^*(d,0)\mathbf{R}_3(d,0)) = 0, \tag{4.13}$$

where $\lambda_{\min}(\cdot)$ is the minimal eigenvalue of the positive definite matrix in the brackets and * Hermitian conjugation. The method based on eq. (4.13) provides fast and stable calculation for any configuration.

4.5 The dispersion spectrum for mirror symmetric profiles

We show that the dispersion spectrum of the mirror symmetric plate is a union of two dispersion spectra – for the symmetric and antisymmetric waves. The key idea to prove this is to decompose the free plate problem into two independent problems. The dispersion equations obtained for symmetric and antisymmetric waves are not directly related to the overall free plate dispersion equation. However their solutions (zeros) are correlated.

4.5.1 Problem decomposition for symmetric and antisymmetric waves

We restate the free plate problem in terms of symmetric and antisymmetric waves. Introducing the solution $\boldsymbol{\eta}_1 = (\mathbf{u}_1, \boldsymbol{\sigma}_1)^T$ with $\boldsymbol{\sigma}_1 \equiv \boldsymbol{\mu}\boldsymbol{\partial}_2\mathbf{u}_1$ in the middle of the plate $x_2 = d/2$, we link it through the propagator to the lower boundary condition at $x_2 = d$ via

$$\mathbf{M}(d, \frac{d}{2}) \begin{pmatrix} \mathbf{u}_1 \\ \boldsymbol{\sigma}_1 \end{pmatrix} = \begin{pmatrix} \tilde{\mathbf{u}}_0 \\ \mathbf{0} \end{pmatrix} \tag{5.14}$$

and to the upper boundary condition at $x_2 = 0$ via

$$\mathbf{M}(0, \frac{d}{2}) \begin{pmatrix} \mathbf{u}_1 \\ \boldsymbol{\sigma}_1 \end{pmatrix} = \begin{pmatrix} \mathbf{u}_0 \\ \mathbf{0} \end{pmatrix}. \tag{5.15}$$

Due to the profile symmetry, the propagator $\mathbf{M}$ satisfies the identity (A.3.5) with $[a_1, b_1] = [0, d/2]$ and $[a_2, b_2] = [d/2, d]$, namely,

$$\mathbf{M}(0, \frac{d}{2}) = \mathbf{S}\mathbf{M}(d, \frac{d}{2})\mathbf{S}^{-1} = \begin{pmatrix} \mathbf{M}_1 & -\mathbf{M}_2 \\ -\mathbf{M}_3 & \mathbf{M}_4 \end{pmatrix} \text{ with } \mathbf{M}(d, \frac{d}{2}) = \begin{pmatrix} \mathbf{M}_1 & \mathbf{M}_2 \\ \mathbf{M}_3 & \mathbf{M}_4 \end{pmatrix} \tag{5.16}$$

Using the identity (5.16), the system (5.14), (5.15) can be recast equivalently via taking difference and sum of (5.14) and (5.15), which leads to

$$\begin{pmatrix} \mathbf{0} & 2\mathbf{M}_2 \\ 2\mathbf{M}_3 & \mathbf{0} \end{pmatrix} \begin{pmatrix} \mathbf{u}_1 \\ \boldsymbol{\sigma}_1 \end{pmatrix} = \begin{pmatrix} \tilde{\mathbf{u}}_0 - \mathbf{u}_0 \\ \mathbf{0} \end{pmatrix} \tag{5.17}$$

and

$$\begin{pmatrix} 2\mathbf{M}_1 & \mathbf{0} \\ \mathbf{0} & 2\mathbf{M}_4 \end{pmatrix} \begin{pmatrix} \mathbf{u}_1 \\ \boldsymbol{\sigma}_1 \end{pmatrix} = \begin{pmatrix} \tilde{\mathbf{u}}_0 + \mathbf{u}_0 \\ \mathbf{0} \end{pmatrix}. \tag{5.18}$$

Equation (5.17) gives the solution $\mathbf{M}_3\mathbf{u}_1 = \mathbf{0}$ which is equivalent to

$$\det \mathbf{M}_3 = 0 \text{ or } \mathbf{u}_1 = \mathbf{0}. \tag{5.19}$$

In turn, (5.18) gives the solution $\mathbf{M}_4\boldsymbol{\sigma}_1 = \mathbf{0}$ which is equivalent to

$$\det \mathbf{M}_4 = 0 \text{ or } \boldsymbol{\sigma}_1 = \mathbf{0}. \tag{5.20}$$

The two solutions obtained (5.19) and (5.20) are linearly independent. The main idea therefore is to decompose the Neumann/Neumann boundary problem (5.14), (5.15) as the following two independent problems for a half-plate: the Neumann boundary problem

$$\det \mathbf{M}_3 = 0 \text{ and } \boldsymbol{\sigma}_1 = \mathbf{0}, \text{ i.e., } \boldsymbol{\eta}(\frac{d}{2}) = \begin{pmatrix} \mathbf{u}_1 \\ \mathbf{0} \end{pmatrix} \tag{5.21}$$

and the Dirichlet boundary problem

$$\det \mathbf{M}_4 = 0 \text{ and } \boldsymbol{u}_1 = \mathbf{0}, \text{ i.e., } \boldsymbol{\eta}(\frac{d}{2}) = \begin{pmatrix} \mathbf{0} \\ \boldsymbol{\sigma}_1 \end{pmatrix}. \tag{5.22}$$

Here the equations $\det \mathbf{M}_3 = 0$ and $\det \mathbf{M}_4 = 0$ ensure traction-free conditions at the plate faces $x_2 = 0$ and $x_2 = d$.

We observe that (5.21) gives the symmetric and (5.22) the antisymmetric waves, correspondingly. It can be verified as follows e.g. for (5.21). On the one hand, we have

$$\mathbf{M}(\frac{d}{2} + x_2, \frac{d}{2}) \begin{pmatrix} \mathbf{u}_1 \\ \mathbf{0} \end{pmatrix} = \begin{pmatrix} \mathbf{M}_1 & \mathbf{M}_2 \\ \mathbf{M}_3 & \mathbf{M}_4 \end{pmatrix} \begin{pmatrix} \mathbf{u}_1 \\ \mathbf{0} \end{pmatrix} = \begin{pmatrix} \mathbf{M}_1 \\ \mathbf{M}_3 \end{pmatrix} \mathbf{u}_1 = \begin{pmatrix} \mathbf{u}(\frac{d}{2} + x_2) \\ \boldsymbol{\sigma}(\frac{d}{2} + x_2) \end{pmatrix} \tag{5.23}$$

for any $0 \leqslant x_2 \leqslant \frac{d}{2}$. On the other hand, it holds

$$\mathbf{M}(\frac{d}{2} - x_2, \frac{d}{2}) \begin{pmatrix} \mathbf{u}_1 \\ \mathbf{0} \end{pmatrix} = \begin{pmatrix} \mathbf{M}_1 & -\mathbf{M}_2 \\ -\mathbf{M}_3 & \mathbf{M}_4 \end{pmatrix} \begin{pmatrix} \mathbf{u}_1 \\ \mathbf{0} \end{pmatrix} = \begin{pmatrix} \mathbf{M}_1 \\ -\mathbf{M}_3 \end{pmatrix} \mathbf{u}_1 = \begin{pmatrix} \mathbf{u}(\frac{d}{2} - x_2) \\ \boldsymbol{\sigma}(\frac{d}{2} - x_2) \end{pmatrix}, \tag{5.24}$$

where the first equality in (5.24) uses the identity (A.3.5) with $[a_1, b_1] = [d/2 - x_2, d/2]$ and $[a_2, b_2] = [d/2, d/2 + x_2]$. The identities (5.23) and (5.24) together give the waves with symmetric displacement and antisymmetric traction at any $0 \leqslant x_2 \leqslant \frac{d}{2}$, i.e.

$$\mathbf{u}(\frac{d}{2} + x_2) = \mathbf{u}(\frac{d}{2} - x_2) \text{ and } \boldsymbol{\sigma}(\frac{d}{2} + x_2) = -\boldsymbol{\sigma}(\frac{d}{2} - x_2). \tag{5.25}$$

These are the symmetric waves. Correspondingly, equation (5.22) defines antisymmetric waves with antisymmetric displacement and symmetric traction, i.e.

$$\mathbf{u}(\frac{d}{2} + x_2) = -\mathbf{u}(\frac{d}{2} - x_2) \text{ and } \boldsymbol{\sigma}(\frac{d}{2} + x_2) = \boldsymbol{\sigma}(\frac{d}{2} - x_2). \tag{5.26}$$

Thus the dispersion spectrum of the mirror symmetric free plate is the union of two spectra (5.21) for the symmetric and (5.22) for the antisymmetric waves.

4.5.2 Dispersion equations in stable terms

The problems (5.21) and (5.22) include equations with numerically unstable propagator. We restate the both problems in numerically stable terms. For the symmetric case (5.21), the dispersion equation in stable terms is given similarly to the free plate dispersion equation (4.12) by the resolvent $\mathbf{R}(d, \frac{d}{2})$ of the half-width propagator:

$$\det \mathbf{R}_3(d, \frac{d}{2}) = 0. \tag{5.27}$$

For the antisymmetric case (5.21), we derive the dispersion equation in stable terms as follows. From

$$\mathbf{M}(d, \frac{d}{2}) \begin{pmatrix} \mathbf{0} \\ \boldsymbol{\sigma}_1 \end{pmatrix} = \begin{pmatrix} \tilde{\mathbf{u}}_0 \\ \mathbf{0} \end{pmatrix} \tag{5.28}$$

we obtain

$$(z\mathbf{I} - \mathbf{M}(d, \frac{d}{2})) \begin{pmatrix} \mathbf{0} \\ \boldsymbol{\sigma}_1 \end{pmatrix} = \begin{pmatrix} -\tilde{\mathbf{u}}_0 \\ z\boldsymbol{\sigma}_1 \end{pmatrix}, \tag{5.29}$$

which implies

$$\begin{pmatrix} \mathbf{0} \\ \boldsymbol{\sigma}_1 \end{pmatrix} = \mathbf{R}(d, \frac{d}{2}) \begin{pmatrix} -\tilde{\mathbf{u}}_0 \\ z\boldsymbol{\sigma}_1 \end{pmatrix} \equiv \begin{pmatrix} \mathbf{R}_1 & \mathbf{R}_2 \\ \mathbf{R}_3 & \mathbf{R}_4 \end{pmatrix} \begin{pmatrix} -\tilde{\mathbf{u}}_0 \\ z\boldsymbol{\sigma}_1 \end{pmatrix}. \tag{5.30}$$

Therefore

$$\tilde{\mathbf{u}}_0 = z\mathbf{R}_1^{-1}\mathbf{R}_2\boldsymbol{\sigma}_1,$$

$$\boldsymbol{\sigma}_1 = -\mathbf{R}_3\tilde{\mathbf{u}}_0 + z\mathbf{R}_4\boldsymbol{\sigma}_1. \tag{5.31}$$

This yields

$$\det(\mathbf{I} + z\mathbf{R}_3\mathbf{R}_1^{-1}\mathbf{R}_2 - z\mathbf{R}_4) = 0 \tag{5.32}$$

as the dispersion equation for the antisymmetric waves.

Note that alternatively to the dispersion equations (5.27) and (5.32) we can calculate the aggregate spectrum by means of the resolvent $\mathbf{R}(d, 0)$ for the entire plate propagator.

4.6 Numerical examples

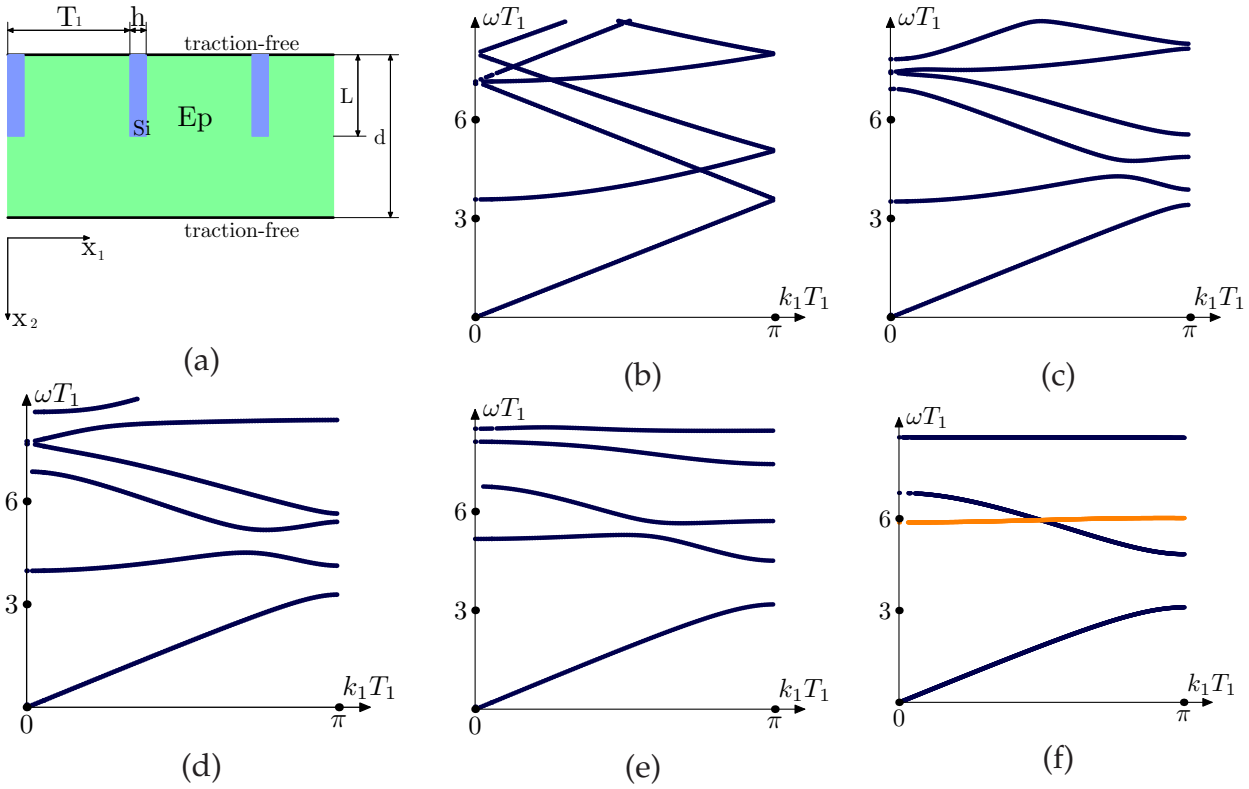

Figure 4.1: (a) Free plate with laterally periodic baffles. (b) $L = 0$: reference (unperturbed) subsonic spectrum formally folded with respect to the subsequently imposed period T_1. Spectra for (c) $L = 0.25$ mm, (d) $L = 0.5$ mm, (e) $L = 0.75$ mm, (f) $L = d = 1$ mm. In Fig. (f), the black and grey lines are symmetric and antisymmetric wave dispersion branches, respectively. In all figures, the values of ωT_1 are in mm/μs.

4.6.1 One array of inclusions

As the first example, consider the free plate of epoxy ($\rho = 1.142$ g/cm^3, $\mu = 1.482$ GPa) with embedded thin laterally T_1-periodic baffles of silicium ($\rho = 2.33$ g/cm^3, $\mu = 79.9$

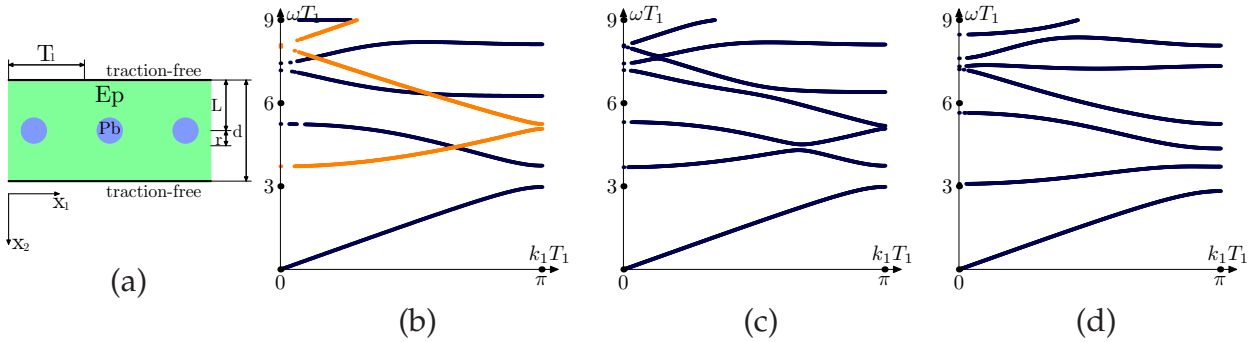

Figure 4.2: (a) Free plate with laterally periodic cylindrical inclusions. Spectra for (b) $L = 0.5$ mm, (c) $L = 0.55$ mm and (d) $L = 0.9$ mm. In Fig. (b), the black and grey lines are symmetric and antisymmetric wave dispersion branches, respectively.

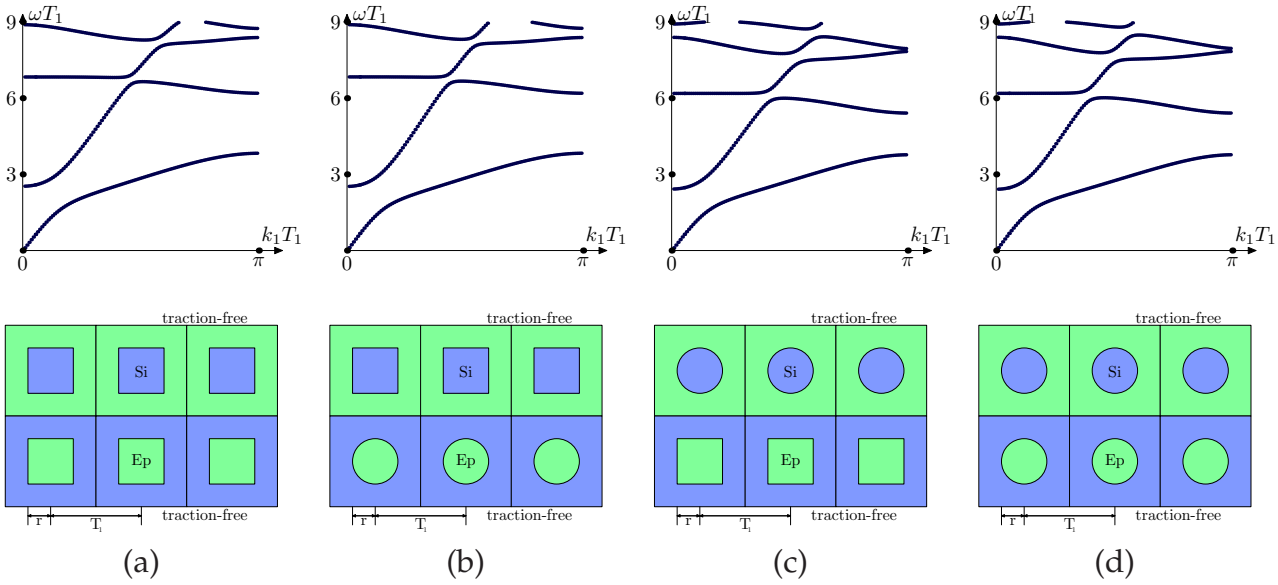

Figure 4.3: The spectra and the corresponding bilayer plate profiles.

GPa); see Fig. 4.1(a). The geometrical parameters are $d = T_1 = 1$ mm, $h = 0.2$ mm. Figs. 4.1(b)-(f) show the evolution of the dispersion spectrum as the length L of baffles varies from $L = 0$ to $L = d$. First, we present in Fig. 4.1(b) the formally folded spectrum of the homogeneous plate. The following Figs. 4.1(c)-(f) show that insertion of baffles of any length L creates a low frequency absolute band gap due to repulsion of the first and the second dispersion branches at the edge of the Brillouin zone. The bigger the inclusions are, the bigger the gap is. At the same time, the structure of the spectrum displayed in Figs. 4.1(c)-(e) and Fig. 4.1(f) has a significant difference. On the one hand, the spectra

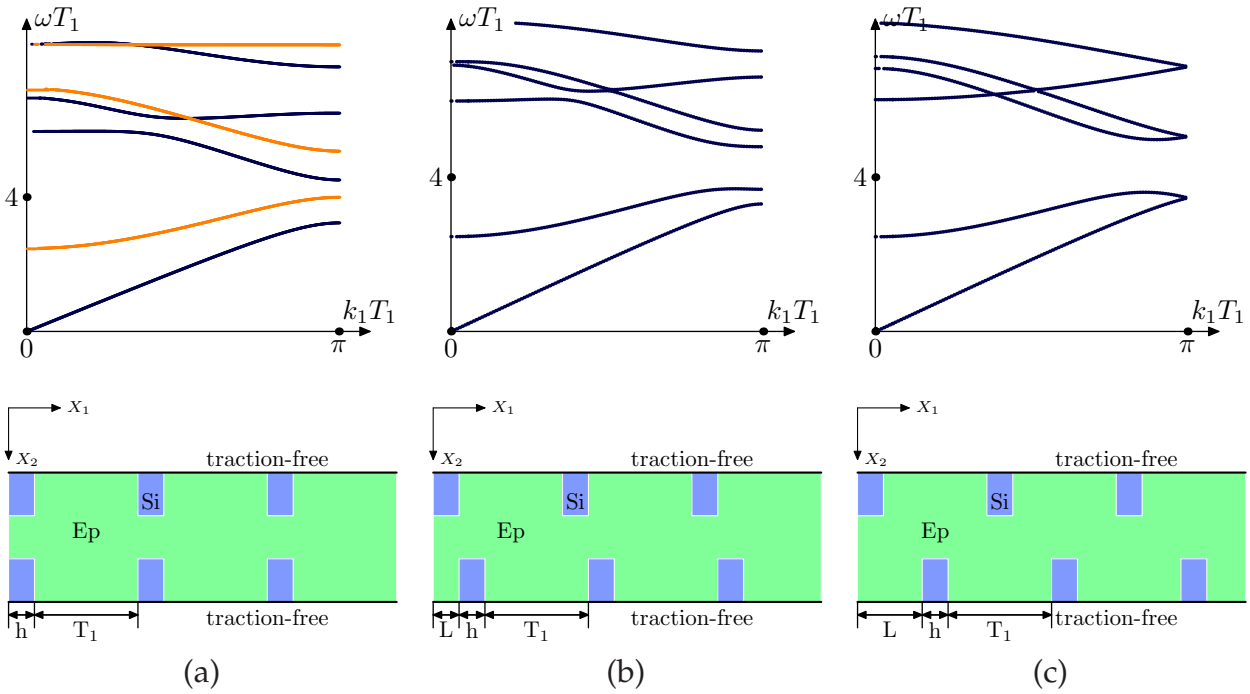

Figure 4.4: Free plate with two arrays of laterally periodic baffles. Spectra and profiles for (a) $L = 0$, (b) $L = 0.3$ mm, (c) $L = 0.5$ mm. In Fig. (a), the black and grey lines are symmetric and antisymmetric wave dispersion branches, respectively.

in Figs. 4.1(c)-(e) compared to the unperturbed spectrum in Fig. 4.1(b) exhibit repulsion of the second and the third dispersion branches at their former intersection inside the Brillouin zone giving rise to the second low-frequency absolute band gap. On the other hand, if the mirror symmetry arises, as it is the case for the profile (f), the dispersion spectrum consists of uncoupled families of symmetric and antisymmetric branches (see §4.5). These spectra intersect, and so the low-frequency gaps arise here by repulsion of the dispersion curves only at the edge of the Brillouin zone.

Consider again the epoxy plate with laterally T_1-periodic Pb ($\rho = 11.6$ g/cm^3, $\mu = 14.9$ GPa) inclusions, which are given this time by the cylindrical bars parallel to the surface; see Fig. 4.2(a). The corresponding geometrical parameters are $d = T_1 = 1$ mm, $r = 0.08$ mm. As in the previous example, we compare the spectrum for the mirror-symmetric profile (Fig. 4.2(b)) and the spectra for non-symmetric profiles obtained by shifting the bars from the midplane position (Figs. 4.2 (c),(d)). The first low-frequency band gap is

observed for any perturbed profile. At the same time, the low-frequency gaps created by the repulsed dispersion branches inside the Brillouin zone are presented only for the non-symmetric profiles, see Figs. 4.2(c),(d). These gaps are the bigger, the closer the cylinders are to the surface: the gap opens up at $L > d/2$ and grows until the inclusions reach the interface at $L = d - r$.

4.6.2 Two arrays of inclusions

The next example is a bilayer plate with both the square and the cylindrical bars. Here we observe how the geometrical shape of inclusions affects the spectral structure. The materials are combined in a complementary way. That is, the bilayer consists of the upper epoxy layer with Si inclusions and the lower Si layer with epoxy inclusions; see the profiles depicted in Figs. 4.3(a)-(d). The geometrical parameters are $T_1 = 1$ mm, $r = 0.25$ mm and the thickness of each layer is $d = 1$ mm. The spectral pattern in the first two Figs. 4.3(a),(b) and in the second two Figs. 4.3(c),(d) are similar, since the shape of the soft epoxy inclusions has no strong influence on the spectral structure. The absolute stop bands exist for any configuration; see Figs. 4.3(a)-(d). They are produced by the repulsion of the dispersion branches inside the Brillouin zone due to asymmetry of the profiles.

In conclusion, we note that the mirror-symmetry of the unit cell profile with respect to the horizontal midplane is not the only cause for intersection of dispersion branches. For example, consider the epoxy plate with two arrays of T_1-periodically embedded rectangular Si bars of the fixed depth 0.5 mm inserted at the both surfaces (the total width of plate is 1.5 mm), see Fig. 4.4(a); other profile parameters are $T_1 = 1$ mm, $h = 0.2$ mm. In Fig. 4.4(a), we observe the intersection of the symmetric and antisymmetric branches in accordance with the symmetry of the profile about the horizontal midplane. This symmetry is destroyed in Fig. 4.4(b), where one array is slightly shifted with respect to the other; however, the intersection persists. Moreover, in Fig. 4.4(c), where the unit cell profile is

symmetric about the vertical midplane, there appear several intersections. Thus the issue of the impact of symmetries on the intersection of branches deserves further analysis.

4.7 The displacement and traction field

4.7.1 The wave field equation

The initial displacement field is calculated via the eigenvectors of the overall plate wave disperison equation $\det \mathbf{R}_3(d,0) = 0$; see (4.12). The propagating displacement and traction field is calculated by combining the straightforward formulation via the propagator $\mathbf{M}(x_2,0)$ at the corresponding depth $x_2 \in [0,d]$ of the plate with the resolvent chain rule.

First recall (cf. (4.9), (4.10)) that the identity

$$(z - \mathbf{M}(d,0)) \begin{pmatrix} \mathbf{u}_0 \\ \mathbf{0} \end{pmatrix} = \begin{pmatrix} z\mathbf{u}_0 - \widetilde{\mathbf{u}}_0 \\ \mathbf{0} \end{pmatrix}, \tag{7.33}$$

yields

$$\begin{pmatrix} \mathbf{u}_0 \\ \mathbf{0} \end{pmatrix} = \begin{pmatrix} \mathbf{R}_1 & \mathbf{R}_2 \\ \mathbf{R}_3 & \mathbf{R}_4 \end{pmatrix} \begin{pmatrix} z\mathbf{u}_0 - \widetilde{\mathbf{u}}_0 \\ \mathbf{0} \end{pmatrix}. \tag{7.34}$$

giving $z\mathbf{u}_0 - \widetilde{\mathbf{u}}_0$ by

$$\mathbf{R}_3(z\mathbf{u}_0 - \widetilde{\mathbf{u}}_0) = \mathbf{0}. \tag{7.35}$$

To calculate the propagating displacement and traction field $\boldsymbol{\eta} \equiv \begin{pmatrix} \mathbf{u}(x_2) & \boldsymbol{\sigma}(x_2) \end{pmatrix}^T$ we apply the resolvent chain rule (for more details see Appendix A, (A.1.3)):

$$\mathbf{R}(d,0) = \mathbf{R}(x_2,0)(z(1-z)\mathbf{R}(d,x_2)\mathbf{R}(x_2,0) + z\mathbf{R}(d,x_2) + z\mathbf{R}(x_2,0) - \mathbf{I})^{-1}\mathbf{R}(d,x_2). \tag{7.36}$$

Inserting (7.36) in the formulation via the propagator

$$\boldsymbol{\eta} = \mathbf{M}(x_2, 0) \begin{pmatrix} \mathbf{u}_0 \\ \mathbf{0} \end{pmatrix} = \mathbf{M}(x_2, 0)\mathbf{R}(d, 0) \begin{pmatrix} z\mathbf{u}_0 - \widetilde{\mathbf{u}}_0 \\ \mathbf{0} \end{pmatrix} \tag{7.37}$$

gives the numerically stable expression in terms of the resolvent $\mathbf{R}_f \equiv \mathbf{R}(x_2, 0)$ at the corresponding depth $x_2 \in [0, d]$ of the plate and the resolvent $\mathbf{R}_r \equiv \mathbf{R}(d, x_2)$ through the rest of the plate:

$$\boldsymbol{\eta} = (z\mathbf{R}_f - \mathbf{I})(z(1-z)\mathbf{R}_r\mathbf{R}_f + z\mathbf{R}_r + z\mathbf{R}_f - \mathbf{I})^{-1}\mathbf{R}_r \begin{pmatrix} z\mathbf{u}_0 - \widetilde{\mathbf{u}}_0 \\ \mathbf{0} \end{pmatrix}, \tag{7.38}$$

where $z\mathbf{u}_0 - \widetilde{\mathbf{u}}_0$ is obtained from (7.35).

4.7.2 Numerical examples

We compare two complementary examples. First, consider the plate of epoxy ($\rho = 1.142$ g/cm^3, $\mu = 1.482$ GPa) with embedded thin laterally T_1-periodic square ($h = 0.5$ mm) bars of silicium ($\rho = 2.33$ g/cm^3, $\mu = 79.9$ GPa); see Fig. 4.5(a). The geometrical parameters are $d = 1.8$ mm, $L = 2 * r = 0.6$ mm and $T_1 = 1$ mm. Displacement has the highest positive or negative amplitude (depicted in red and blue) moving along the interfaces inside the soft matrix, decreasing towards the midplane of the plate (depicted in light green) and completely vanishing (depicted in black) on the stiff inclusions in the center of the plate. This behavior detects the rectangular form of inclusions, the (black) areas with zero displacement surrounded by (light green) minor displacement wave field. Traction field has the biggest and lowest amplitude values (depicted in red and blue) on the stiff inclusions, keeps near zero (depicted in light green) inside the soft matrix and vanishes completely (depicted in black) between the inclusions and towards the upper and lower surfaces. Therefore the traction field also recognizes the inclusions.

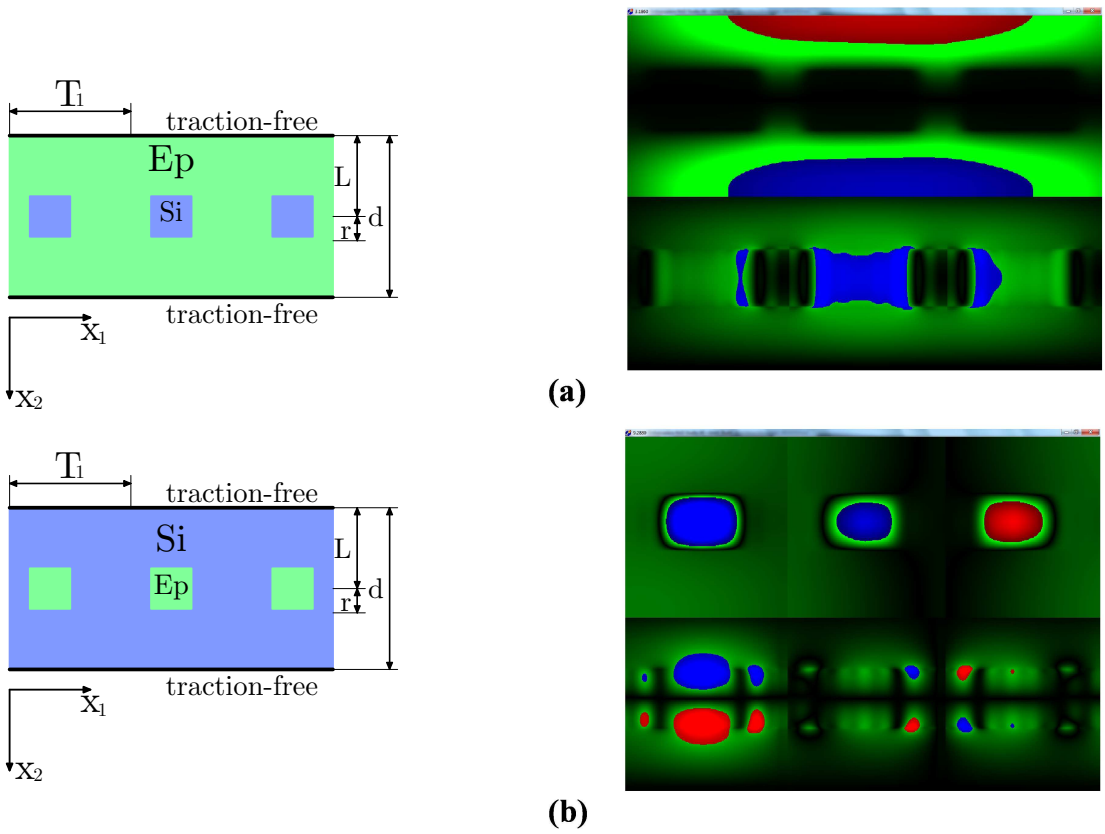

Figure 4.5: The left-hand diagrams show free plate with laterally periodic square bars with the matrix/inclusions materials (a) Ep/Si and (b) Si/Ep. The right-hand diagrams show the real part of displacement and traction field at the same time, $\mathrm{Re}(u)$ and $\mathrm{Re}(\sigma)$ (upper and lower part of the diagram, respectively) for the corresponding free plate with $k_1 T_1 = 0.4\pi$ and (a) $\omega T_1 = 3.19$, (b) $\omega T_1 = 9.3$. Here, black corresponds to zero wave field, green to near-zero (with values (a) $0 < |\mathrm{Re}(u)| < 0.1mm \equiv u_{Re}$, $0 < |\mathrm{Re}(\sigma)| < 0.5GPa \equiv s_{Re}$ and (b) $u_{Re} = 0.2mm$, $s_{Re} = 0.7GPa$) wave field, red and blue (with (a) $u_{Re} < |\mathrm{Re}(u)| < 1mm$, $s_{Re} < |\mathrm{Re}(\sigma)| < 0.9GPa$ and (b) $u_{Re} < |\mathrm{Re}(u)| < 1.1mm$, $s_{Re} < |\mathrm{Re}(\sigma)| < 1.5GPa$) to bigger positive and negative wave field amplitudes.

Secondly, consider the plate with the same parameters, but oppositely chosen materials, silicium plate with epoxy inclusions; see Fig. 4.5(b). Here, the propagation of displacement wave field is concentrated on the soft inclusions, where it achieves the highest positive or negative phase (depicted in red and blue), taking only minor values (depicted

in light green) inside the stiff matrix. Traction field has the highest and lowest amplitude values on the interfaces between matrix and inclusions and on the edges of inclusions (depicted in red and blue), keeps near zero around these areas and vanishes completely elsewhere, in particular towards the upper and lower surfaces.

4.8 Conclusion

The dispersion equation in terms of the layer resolvent $\mathbf{R}$ is obtained by a direct substitution of the exponentially growing propagator $\mathbf{M}$. Next, the dispersion relations for the mirror-symmetric plate with respect to the horizontal midplane are derived. We show that the dispersion spectrum of the mirror-symmetric plate is a union of two dispersion spectra – for the symmetric and antisymmetric waves. The key idea to prove this is to decompose the free plate problem into two independent problems. The dispersion equations obtained for symmetric and antisymmetric waves are not directly related to the overall free plate dispersion equation. However their solutions (zeros) are correlated.

We illustrate the analytical results by comparing the spectra of the mirror-symmetric profiles with their asymmetric perturbations. One observes that mirror symmetry gives no gaps inside the Brillouin zone, whereas its asymmetric perturbation causes repulsion of the dispersion branches inside the Brillouin zone producing a stop band. Next, we consider structures with absolute stop bands modelled by varying position, size, shape and material of the inclusions. The closer we place the inclusion to the surface and the bigger we make the inclusions, the bigger gaps we obtain. At the same time, the shape of the, specifically, soft inclusion has no strong influence on the spectral structure.

Finally, we calculate the wave field in terms of the initial field and two resolvents. The initial field $\widetilde{\boldsymbol{\eta}}(0)$ is obtained as an eigenvector corresponding to the dispersion eigenvalue problem. The two resolvents are the resolvent taken at the corresponding depth of the plate and the resolvent through the rest of the plate. The starting point of this approach is

to recast the initial field $\boldsymbol{\eta}(0)$ in terms of the resolvent $\mathbf{R}(d,0)$ of the whole plate, i.e. $\boldsymbol{\eta}(0) = \mathbf{R}(d,0)\widetilde{\boldsymbol{\eta}}(0)$. This yields a numerically stable expression $\boldsymbol{\eta}(x_2) = \mathbf{M}(x_2,0)\mathbf{R}(d,0)\widetilde{\boldsymbol{\eta}}(0)$ for the whole field. The crucial point here is that the product $\mathbf{M}(x_2,0)\mathbf{R}(d,0)$ is numerically stable for $x_2 \in [0,d]$, since we can decompose $\mathbf{R}(d,0)$ into $\mathbf{R}(d,x_2)$ and $\mathbf{R}(x_2,0)$ using the resolvent chain rule.

In numerical examples for the wave field, we consider the plates with highly contrasting matrix/inclusions stiffness values. This allows us to recognize well the plate geometry by observing the amplitudes of the displacement and traction fields. For example, a stiff inclusion in a soft matrix can be detected as an area with zero displacement values and at the same time maximal traction field values.

Chapter 5

Guided waves for a 2D layer between two 2D substrates

5.1 Introduction

We propose for the 2D-periodic plate sandwiched between two 2D-periodic substrates the resolvent method based on an analytical approach. Other works on this subject use the classical numerical means such as extended PWE (suitable only for uniform substrates), supercell method in combination with FEM, FDM or PWE (suitable for any substrate: uniform, depth-uniform or 2D-periodic). Our approach applies exact integration in the depth coordinate and reduces the problem to the unit cell of the periodic structure in contrast to other methods involving truncation in all coordinates and consideration of several unit cells. Thus the advantages of the resolvent method are accuracy and efficiency due to the smaller size of the input matrix of coefficients of the governing system of equations ($O(N)$ instead of $O(N^2)$ for other methods).

The guided wave in the sandwiched plate propagates along the plate decreasing in the lower and upper substrates. This calls for a projector on the decreasing waves in the lower substrate like for the Love wave problem (see Chapter 3). Additionally, the modes in the

upper substrate decreasing in the direction opposite to the direction of reference are given by the projector on the increasing modes. Hence, it is convenient to keep subscripts 'd' and 'i' for the projectors on the modes decreasing in the direction $x_2 \to +\infty$ and in the opposite direction $x_2 \to -\infty$, respectively. We use a tilde to distinguish the upper half-space. Thus, by the lower half-space projector $\mathbf{P}_d$, we extract the modes decreasing in the lower half-space for $x_2 \to +\infty$. In turn, by the projector $\widetilde{\mathbf{P}}_i$, we extract the modes decreasing in the upper half-space for $x_2 \to -\infty$. At the same time, the propagation through the plate is provided by the layer resolvent $\mathbf{R}_l$. As a result, the dispersion equation for the sandwiched plate is stated in terms of $\mathbf{R}_l$, $\mathbf{P}_d$ and $\widetilde{\mathbf{P}}_i$.

Apart from the general type, the mirror-symmetric sandwiched plate with respect to the horizontal midplane is considered. As in the case of the plate waves (see Chapter 4), the problem for the mirror-symmetric profile can be split up into two independent problems for symmetric and antisymmetric waves.

Numerical examples are discussed for sandwiched plate with identical and dissimilar substrates. Moving the inclusions in the plate, we perturb the mirror symmetry (of the whole structure or only of the plate). This provides useful observations on the existence and width of the band gaps. As in the rest of the work, the plate width is taken such that it admits several subsonic branches.

The displacement and traction field for the sandwiched plate are obtained, on the one hand, by using the wave field calculation method for the free plate (see Chapter 4) in terms of resolvents and, on the other hand, by introducing two particular propagators. These propagators are the propagator $\mathbf{M}_d$ for decreasing modes in the lower substrate and the propagator $\widetilde{\mathbf{M}}_{dop}$ for decreasing modes in the opposite direction in the upper substrate. We define $\mathbf{M}_d$ and $\widetilde{\mathbf{M}}_{dop}$ as the modified spectral projector $\mathbf{P}_d$.

5.2 Problem statement

Consider a 2D PC layer $\{\mathbf{x} = (x_1, x_2) : \ 0 \leqslant x_2 \leqslant d\}$ of thickness d embedded in between two 2D half-spaces $x_2 \in (-\infty, 0]$ and $x_2 \in [d, \infty)$; see Fig. 5.1. Both the layer and the half-spaces are assumed to be of the same horizontal period $T_1 = 1$ along the axis X_1. The vertical periods of the upper and lower half-spaces along the axis X_2 are T_2 and $\widetilde{T}_2$, respectively. As in the rest of the work, we assume that the PC structure is uniform along the axis X_3.

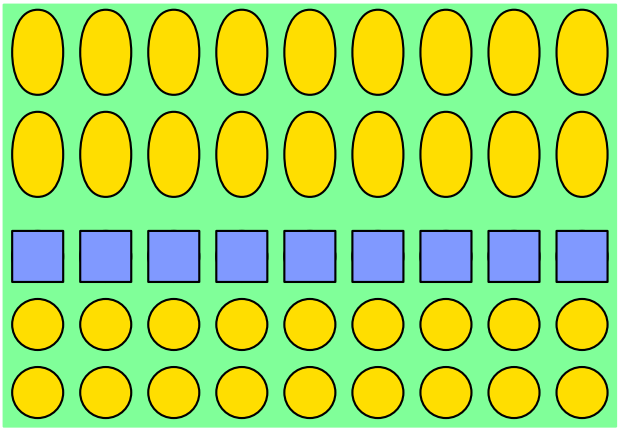

Figure 5.1: Example of a 2D PC plate embedded between two semi-infinite substrates

The SH wave has the form $v_3(\mathbf{x}, t) = v(\mathbf{x})e^{-i\omega t}$. The problem for the plate between two substrates consists of the scalar wave equation

$$\partial_1(\mu\partial_1 v) + \partial_2(\mu\partial_2 v) = -\rho\omega^2 v \tag{2.1}$$

with the displacement continuity conditions at the interfaces $x_2 = 0$ and $x_2 = d$ and the radiation conditions into the depths of both substrates given by

$$\lim_{x_2\to+\infty} v(x_2) = 0, \quad \lim_{x_2\to-\infty} v(x_2) = 0. \tag{2.2}$$

The shear coefficient $\mu(\mathbf{x})$ and the density $\rho(\mathbf{x})$ are 1-periodic in x_1. Hence the SH wave

has the Floquet-Bloch form $v(\mathbf{x}) = u(\mathbf{x})e^{ik_1x_1}$ with $u(\mathbf{x})$ 1-periodic in x_1 and the wave number $k_1 \in [-\pi, \pi]$. Similarly as in §3.2, after plane wave expansion in x_1, equations (2.1) and (2.2) can be recast in the system of the first order ordinary differential equations

$$\partial_2 \boldsymbol{\eta} = \mathbf{Q}\boldsymbol{\eta} \tag{2.3}$$

with the radiation conditions

$$\lim_{x_2 \to \pm\infty} \boldsymbol{\eta}(x_2) = 0. \tag{2.4}$$

Here, $\boldsymbol{\eta} = (\mathbf{u},\ \boldsymbol{\mu}\partial_2\mathbf{u})^T$ and $\mathbf{Q}$ are given by (2.10) in terms of Fourier coefficients (2.7).

5.3 Dispersion equation with resolvent and projector

The spectrum is given by the localized waves spectrum and the propagative waves spectrum.

5.3.1 The localized waves spectrum

We restate the sandwiched plate problem (2.3) and (2.4). The wave $\boldsymbol{\eta}(0)$ taken at the interface $x_2 = 0$ between the layer and the upper half-space is decreasing for $x_2 \to -\infty$ in the upper half-space and for $x_2 \to +\infty$ in the lower half-space after propagating through the layer. This calls for a projector on the decreasing waves in the lower substrate like for the Love wave problem (see Chapter 3). Additionally, the modes decreasing in the direction opposite to the direction of reference are given by the projector on the increasing modes. Hence, it is convenient to keep subscripts 'd' and 'i' for the projectors on the modes decreasing in the direction $x_2 \to +\infty$ and in the opposite direction $x_2 \to -\infty$, respectively. We use a tilde to distinguish the upper half-space. Thus, by the lower half-space projector $\mathbf{P}_d$ applied to $\boldsymbol{\eta}(d) = \mathbf{M}_l\boldsymbol{\eta}(0)$, where $\mathbf{M}_l$ is the layer propagator, we extract

the modes decreasing in the lower half-space for $x_2 \to +\infty$. In turn, by the projector $\widetilde{\mathbf{P}}_i$ applied to $\boldsymbol{\eta}(0)$ we extract the modes decreasing in the upper half-space for $x_2 \to -\infty$. This gives the dispersion system

$$\begin{aligned} &(\widetilde{\mathbf{P}}_i - \mathbf{I})\boldsymbol{\eta}(0) = 0 \text{ and} \\ &(\mathbf{P}_d - \mathbf{I})\mathbf{M}_l\boldsymbol{\eta}(0) = 0. \end{aligned} \tag{3.5}$$

To circumvent the instabilities of the propagator $\mathbf{M}_l$, our ansatz is, as for the Love wave problem (see § 3.5.1), to define the solution $\boldsymbol{\eta}(0)$ in terms of the layer resolvent $\mathbf{R}_l$, i.e.

$$\boldsymbol{\eta}(0) = \mathbf{R}_l\widetilde{\boldsymbol{\eta}}. \tag{3.6}$$

Then, using the identity $\mathbf{M}_l\mathbf{R}_l = z\mathbf{R}_l - \mathbf{I}$ (see (3.15)), the system (3.5) is stated in numerically stable terms as

$$\begin{aligned} \mathbf{D}_1\widetilde{\boldsymbol{\eta}} &\equiv (\widetilde{\mathbf{P}}_i - \mathbf{I})\mathbf{R}_l\widetilde{\boldsymbol{\eta}} = 0 \text{ and} \\ \mathbf{D}_2\widetilde{\boldsymbol{\eta}} &\equiv (\mathbf{P}_d - \mathbf{I})(z\mathbf{R}_l - \mathbf{I})\widetilde{\boldsymbol{\eta}} = 0. \end{aligned} \tag{3.7}$$

Next to evaluate the both equations simultaneously, we first rewrite the system (3.7) as a unique equality

$$\mathbf{D}\widetilde{\boldsymbol{\eta}} = 0 \text{ with } \mathbf{D} = \mathbf{D}_1^*\mathbf{D}_1 + \mathbf{D}_2^*\mathbf{D}_2, \tag{3.8}$$

which yields

$$\det \mathbf{D} = 0. \tag{3.9}$$

This leads to the dispersion equation in the final numerically stable form (see the remark to (5.42)) via the minimal eigenvalue of the corresponding positive definite matrix $\mathbf{D}$ as:

$$\lambda_{min}(\mathbf{D}) = 0. \tag{3.10}$$

5.3.2 Projection of the spectrum of the propagating waves

Similarly as for the Love wave problem (see § 3.5.2), we calculate the projection of the dispersion surface $\omega(k_1, k_2)$ on the plane (ω, k_1) in terms of the projectors $\mathbf{P}_p$ and $\widetilde{\mathbf{P}}_p$ on propagating modes corresponding to the upper and lower half-spaces. As follows from the projector definition (see (4.29)), their trace indicates the number $N_p(\omega, k_1)$ of the propagating modes, i.e.

$$N_p(\omega, k_1) = \operatorname{trace} \mathbf{P}_p, \quad \widetilde{N}_p(\omega, k_1) = \operatorname{trace} \widetilde{\mathbf{P}}_p. \tag{3.11}$$

Therefore, we determine the projections of the propagative spectra of the upper and lower half-space at a given ω and k_1 by the condition

$$N_p(\omega, k_1) \geqslant 1 \ \text{ or } \ \widetilde{N}_p(\omega, k_1) \geqslant 1. \tag{3.12}$$

To calculate the projection of the propagative spectra in terms of $\mathbf{P}_d$, we specify (5.45) by

$$N_p(\omega, k_1) = 2(2N+1) - 2 \operatorname{trace} \mathbf{P}_d, \quad \widetilde{N}_p(\omega, k_1) = 2(2N+1) - 2 \operatorname{trace} \widetilde{\mathbf{P}}_d \tag{3.13}$$

using (3.11) and the identity (A.2.10$_3$).

5.4 The dispersion equation for the mirror-symmetric case

5.4.1 Problem decomposition for symmetric and antisymmetric waves

Assume that the waveguide consisting of the layer embedded between two semi-infinite substrates is mirror-symmetric. This implies that the system matrix $\mathbf{Q}_l$ is an even function and $\mathbf{Q}_{\text{sub}}$, $\widetilde{\mathbf{Q}}_{\text{sub}}$ are mirror-symmetric with respect to the midplane $x_2 = d/2$ of the waveguide structure. Then, according to the identities (A.3.5) and (A.3.7), the propagator

and the projectors are related as follows:

$$\mathbf{M}_l(0,d/2)=\mathbf{S}\mathbf{M}_l(d,d/2)\mathbf{S}^{-1},\ \ \widetilde{\mathbf{P}}_i=\mathbf{S}\mathbf{P}_d\mathbf{S}^{-1}. \tag{4.14}$$

Introducing the solution $\boldsymbol{\eta}_1=(\mathbf{u}_1,\boldsymbol{\sigma}_1)^T$ at the midplane $x_2=d/2$ we rewrite the dispersion equation (3.5) in the form

$$\begin{aligned}(\widetilde{\mathbf{P}}_i-\mathbf{I})\mathbf{M}_l(0,d/2)\boldsymbol{\eta}_1=\mathbf{0},\\ (\mathbf{P}_d-\mathbf{I})\mathbf{M}_l(d,d/2)\boldsymbol{\eta}_1=\mathbf{0}.\end{aligned} \tag{4.15}$$

Denoting the matrix

$$(\widetilde{\mathbf{P}}_i-\mathbf{I})\mathbf{M}_l(0,d/2)\equiv\mathbf{A}=\begin{pmatrix}\mathbf{A}_1 & \mathbf{A}_2\\ \mathbf{A}_3 & \mathbf{A}_4\end{pmatrix} \tag{4.16}$$

and using (4.14), we observe that (4.15) is equivalent to

$$\begin{pmatrix}\mathbf{A}_1 & \mathbf{A}_2\\ \mathbf{A}_3 & \mathbf{A}_4\end{pmatrix}\begin{pmatrix}\mathbf{u}_1\\ \boldsymbol{\sigma}_1\end{pmatrix}=\begin{pmatrix}\mathbf{0}\\ \mathbf{0}\end{pmatrix}\ \text{ and }\ \begin{pmatrix}\mathbf{A}_1 & -\mathbf{A}_2\\ -\mathbf{A}_3 & \mathbf{A}_4\end{pmatrix}\begin{pmatrix}\mathbf{u}_1\\ \boldsymbol{\sigma}_1\end{pmatrix}=\begin{pmatrix}\mathbf{0}\\ \mathbf{0}\end{pmatrix}. \tag{4.17}$$

Adding and subtracting these two equalities yields

$$\begin{pmatrix}\mathbf{A}_1 & \mathbf{0}\\ \mathbf{0} & \mathbf{A}_4\end{pmatrix}\begin{pmatrix}\mathbf{u}_1\\ \boldsymbol{\sigma}_1\end{pmatrix}=\begin{pmatrix}\mathbf{0}\\ \mathbf{0}\end{pmatrix}\ \text{ and }\ \begin{pmatrix}\mathbf{0} & \mathbf{A}_2\\ \mathbf{A}_3 & \mathbf{0}\end{pmatrix}\begin{pmatrix}\mathbf{u}_1\\ \boldsymbol{\sigma}_1\end{pmatrix}=\begin{pmatrix}\mathbf{0}\\ \mathbf{0}\end{pmatrix}. \tag{4.18}$$

Let $\mathbf{u}_1=\mathbf{0}$, then $\mathbf{A}_2\boldsymbol{\sigma}_1=0$ and $\mathbf{A}_4\boldsymbol{\sigma}_1=0$. Let $\boldsymbol{\sigma}_1=\mathbf{0}$, then $\mathbf{A}_1\mathbf{u}_1=0$ and $\mathbf{A}_3\mathbf{u}_1=0$. Thus we obtain the equivalent form of (4.17) as the union of two independent problems[1]

$$\mathbf{u}_1=\mathbf{0}\ \text{ and }\ \det(\mathbf{A}_2^*\mathbf{A}_2+\mathbf{A}_4^*\mathbf{A}_4)=0 \tag{4.19}$$

and

$$\boldsymbol{\sigma}_1=\mathbf{0}\ \text{ and }\ \det(\mathbf{A}_1^*\mathbf{A}_1+\mathbf{A}_3^*\mathbf{A}_3)=0. \tag{4.20}$$

[1]The case $\mathbf{u}_1\neq\mathbf{0}$, $\boldsymbol{\sigma}_1\neq\mathbf{0}$ is exceptional corresponding to the intersection of (4.19) and (4.20).

The problems (4.19) and (4.20) give independent families of dispersion branches. The union of all these branches composes the whole set of dispersion branches for guided spectrum. Similarly as in §4.5.1, it follows that eq. (4.19) defines the waves with the antisymmetric displacement $\mathbf{u}(d/2+x_2) = -\mathbf{u}(d/2-x_2)$ and symmetric traction $\boldsymbol{\sigma}(d/2+x_2) = \boldsymbol{\sigma}(d/2-x_2)$ with $x_2 \in [0, d/2]$, while eq. (4.19) defines the waves with symmetric displacement and antisymmetric traction. This is the same conclusion as for the free symmetric plates. Finally, we note that the propagative spectra for the mirror-symmetric upper and low substrates are the same $N_p(\omega, k_1) = \widetilde{N}_p(\omega, k_1)$. This follows from the fact that $\operatorname{trace} \mathbf{P}_p$ is invariant under the mirror-symmetry.

5.4.2 Dispersion equations in stable terms

Equations (4.19) and (4.20) include numerically unstable propagator. Let us restate them in stable terms. As for the Love wave problem in § 3.5, we assume that $\boldsymbol{\eta}_1 = \mathbf{R}_l(d, d/2)\boldsymbol{\eta}_0$ and then rewrite the second equation in (4.15) as follows

$$(\mathbf{P}_d - \mathbf{I})(z\mathbf{R}_l(d, d/2) - \mathbf{I})\boldsymbol{\eta}_0 = \mathbf{0}. \tag{4.21}$$

Denoting

$$\mathbf{R}_l(d, d/2) \equiv \mathbf{R} = \begin{pmatrix} \mathbf{R}_1 & \mathbf{R}_2 \\ \mathbf{R}_3 & \mathbf{R}_4 \end{pmatrix}, \quad \boldsymbol{\eta}_0 = \begin{pmatrix} \mathbf{u}_0 \\ \boldsymbol{\sigma}_0 \end{pmatrix}, \tag{4.22}$$

the condition $\mathbf{u}_1 = \mathbf{0}$ in (4.19) via $\boldsymbol{\eta}_1 = \mathbf{R}\boldsymbol{\eta}_0$ leads to $\mathbf{u}_0 = -\mathbf{R}_1^{-1}\mathbf{R}_2\boldsymbol{\sigma}_0$, which on substituting in (4.21) gives us the dispersion equation for the antisymmetric waves

$$\lambda_{\min}(\mathbf{D}^*_{asym}\mathbf{D}_{asym}) = 0, \quad \text{where } \mathbf{D}_{asym} \equiv (\mathbf{P}_d - \mathbf{I})(z\mathbf{R} - \mathbf{I}) \begin{pmatrix} \mathbf{R}_1^{-1}\mathbf{R}_2 \\ -\mathbf{I} \end{pmatrix}. \tag{4.23}$$

By analogy, the dispersion equation for the symmetric waves is obtained in the form

$$\lambda_{\min}(\mathbf{D}^*_{sym}\mathbf{D}_{sym}) = 0, \quad \text{where } \mathbf{D}_{sym} \equiv (\mathbf{P}_d - \mathbf{I})(z\mathbf{R} - \mathbf{I}) \begin{pmatrix} -\mathbf{I} \\ \mathbf{R}_4^{-1}\mathbf{R}_3 \end{pmatrix}. \tag{4.24}$$

5.5 Numerical examples

5.5.1 Square inclusions and 2D substrates

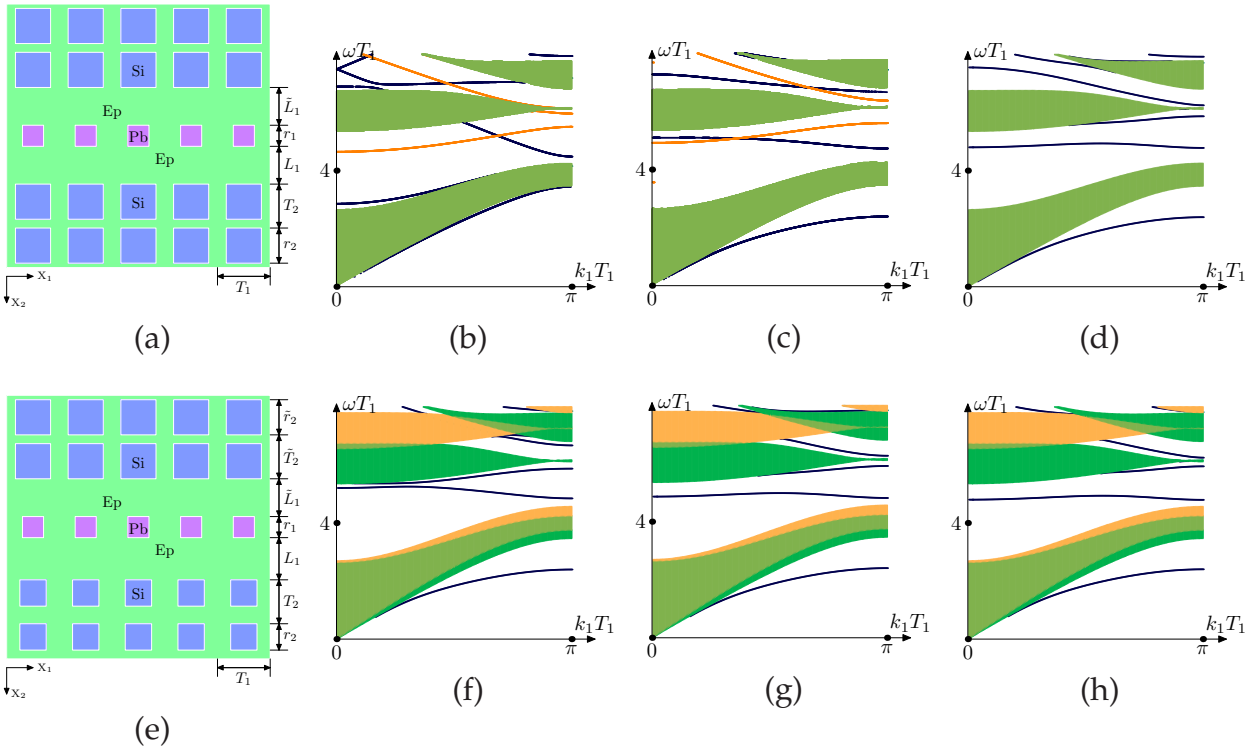

Figure 5.2: (a) Layer between two identical half-spaces. The spectra for (a) with (b) the uniform plate (c) $L_1 = 0.6$ mm; (d) $L_1 = 0.7$. In Figs. (b) and (c), the black and grey (dark blue and orange online) lines are dispersion branches for symmetric and antisymmetric waves. (e) Layer between two dissimilar half-spaces. The spectra for (e) with (f) $L_1 = 0.6$ mm, (g) $L_1 = 0.7$ mm, (h) $L_1 = 0.5$ mm. The light grey and dark grey areas (yellow and dark green online) correspond to the spectra of the propagating waves in the upper and lower substrate, correspondingly. The grey areas (light green online) correspond to the superposition of these spectra.

Consider the layer of epoxy of thickness $d = L_1 + r_1 + \widetilde{L}_1 = 1.6$ mm located between

the two periodic half-spaces consisting of silicium square rods inside epoxy matrix. The rods can be of equal ($r_2 = 0.6$ mm) or different ($r_2 = 0.6$ mm, $\widetilde{r}_2 = 0.7$ mm) size; see the structures in Fig. 5.2. (a),(e). The geometrical parameters are $T_1 = 1$ mm and $T_2 = \widetilde{T}_2 = 1.2$ mm. Assume first that half-spaces are identical (Fig. 5.2. (a)) and hence have the same propagative spectra, see Figs. 5.2 (b)-(d). The layer is either uniform ($r_1 = 0$) or it includes periodic square rods of Pb ($r_1 = 0.4$ mm) which are placed either at the layer midplane ($L_1 = \widetilde{L}_1$) or not ($L_1 \neq \widetilde{L}_1$). The first two cases imply the mirror symmetry of the structure, therefore symmetric and antisymmetric branches (see Figs. 5.2 (b),(c)) hinder existence of the absolute gaps, since these branches intersect each other. In Fig. 5.2 (d), the shift of layer inclusions destroys the mirror symmetry, therefore the branches split and the absolute gap opens up. Next let the substrates be dissimilar; see Fig. 5.2 (e). Now the propagative spectra of the upper and lower substrates differ from each other; see Figs. 5.2 (f)-(h). Since the overall structure is asymmetric, the dispersion branches of the localized spectrum do not intersect and create an absolute gap regardless of whether the layer inclusions are symmetric (Fig. 5.2 (f)) or asymmetric (Fig. 5.2 (g),(h)). In the latter case the gap is wider.

5.5.2 Circular inclusions and layered substrates

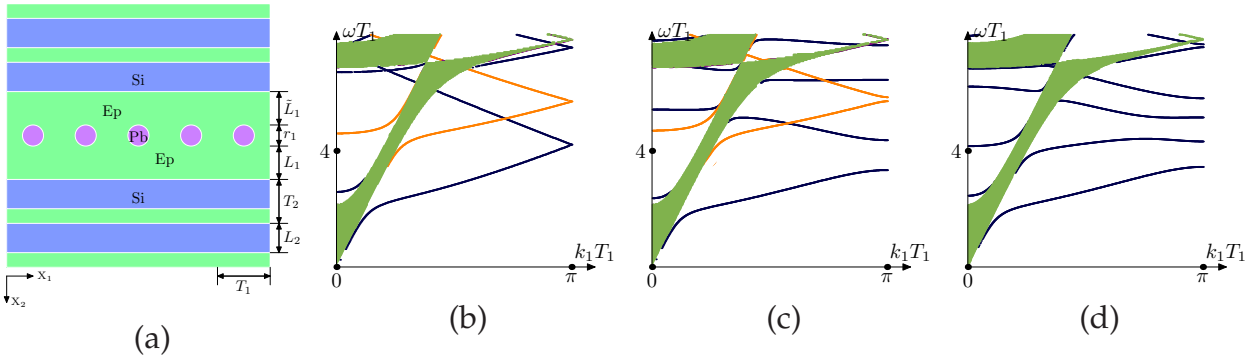

(a) (b) (c) (d)

Figure 5.3: (a) Layer between two mirror-symmetric half-spaces. The spectra for (a) with (b) the uniform layer, (c) $L_1 = 0.8$ mm, (d) $L_1 = 1.1$ mm.

Consider again the layer of epoxy of thickness $d = L_1 + r_1 + \widetilde{L}_1 = 1.6$ mm, this time

between two periodically bilayered substrates which are mirror-symmetric with respect to the layer midplane; see Fig. 5.3 (a). Their geometrical parameters are $T_1 = 1$ mm, $T_2 = 1.5$ mm and $L_2 = 1$ mm. Note that the propagative spectra for the mirror-symmetric substrates are identical. Moreover, the propagative spectrum has no stop bands, since the substrates are laterally uniform; see Fig. 5.3 (b)-(d). If the layer is uniform ($r_1 = 0$), then the whole structure is laterally uniform and mirror-symmetric, so that its spectrum represents formally folded and intersecting branches of symmetric and antisymmetric waves; see Fig. 5.3 (b). There are no band gaps in this case. Next let us place the periodic inclusions (Pb cylinders of radius $r_1 = 0.08$ mm) in the middle of the layer, so that the structure becomes laterally heterogeneous staying mirror-symmetric. Then the symmetric/antisymmetric uncoupling persists and hence the corresponding branches intersect inside the Brillouin zone; see Fig. 5.3 (c). Now let us shift the inclusions with respect to the layer midplane. The structure becomes asymmetric. Hence the branches no longer intersect, but repulse each other inside the Brillouin zone; see Fig. 5.3 (d).

5.6 The displacement and traction field

5.6.1 The propagators for decreasing modes

The wave field decreasing into the depth of the lower and upper 2D-periodic substrates is calculated by introducing two new tools, the propagators $\mathbf{M}_d$ and $\widetilde{\mathbf{M}}_{dop}$ for decreasing modes in the direction of reference and in the opposite direction, respectively. These new objects $\mathbf{M}_d \equiv \mathbf{M}_d(T_2 + x_2, x_2)$ and $\widetilde{\mathbf{M}}_{dop} \equiv \widetilde{\mathbf{M}}_{dop}(x_2 - T_2, x_2)$ can be viewed as the substrate propagators $\mathbf{M}_{sub}(x_2+T_2, x_2)$ and $\widetilde{\mathbf{M}}_{sub}(x_2-\widetilde{T}_2, x_2)$ with only eigenvalues corresponding to decreasing modes left and other eigenvalues replaced by zeroes. We define $\mathbf{M}_d$ and $\widetilde{\mathbf{M}}_{dop}$ as the modified spectral projector $\mathbf{P}_d$ on decreasing modes in the direction of reference

and the projector

$$\widetilde{\mathbf{P}}_{dop} = \frac{1}{2\pi i} \oint_{|z|=1-0} \widetilde{\mathbf{R}}_z(-\widetilde{T}_2, 0) dz. \tag{6.25}$$

on the decreasing modes in the opposite direction, respectively (cf. spectral projector definition (4.31) in 3.4.3):

$$\mathbf{M}_d(x_2 + T_2, x_2) = \frac{1}{2\pi i} \oint_{|z|=1-0} z\mathbf{R}_z(x_2 + T_2, x_2) dz \tag{6.26}$$

and

$$\widetilde{\mathbf{M}}_{dop}(x_2 - \widetilde{T}_2, x_2) = \frac{1}{2\pi i} \oint_{|z|=1-0} z\widetilde{\mathbf{R}}_z(x_2 - \widetilde{T}_2, x_2) dz. \tag{6.27}$$

Moreover, we have the identity

$$\widetilde{\mathbf{M}}_{dop}(x_2 - \widetilde{T}_2, x_2) = \mathbf{T}\widetilde{\mathbf{M}}^*_d(x_2, x_2 - \widetilde{T}_2)\mathbf{T}^{-1}, \tag{6.28}$$

similarly to the projector identity (A.2.8) for the projectors $\widetilde{\mathbf{P}}_d$ and $\widetilde{\mathbf{P}}_{dop}$; see (C.3.5) for more details. Note that the implementation of $\mathbf{M}_d$ and $\widetilde{\mathbf{M}}_{dop}$ as a matrix function of corresponding resolvents is discussed in Appendix C.3.3.

5.6.2 The wave field equation

The displacement and traction field is recast in terms of the initial field, the resolvents and two propagators $\mathbf{M}_d$ and $\widetilde{\mathbf{M}}_{dop}$ for decreasing modes defined in (6.26) and (6.27). The calculation consists of two main steps. On the one hand, we use the wave field calculation method for the free plate (see Chapter 4) in terms of resolvents. On the other hand, the wave field in the depth of the upper and lower substrates is given by $\mathbf{M}_d$ and $\widetilde{\mathbf{M}}_{dop}$.

First, the wave field is calculated inside the plate and the surrounding layers of the upper and lower substrates, i.e. for $x_2 \in [-\widetilde{T}_2, d + T_2]$. Here we apply the same resolvent method like for the traction-free plate (see §4.7.1.), since it is independent from boundary

conditions (either with traction or traction-free). The initial wave field at the interface $x_2 = -\widetilde{T}_2$ of the first and second layer in the upper substrate is given by

$$\boldsymbol{\eta}(-\widetilde{T}_2) = \mathbf{R}_{sls}\boldsymbol{\eta}_0, \tag{6.29}$$

where $\mathbf{R}_{sls} \equiv \mathbf{R}(d + T_2, -\widetilde{T}_2)$ and $\boldsymbol{\eta}_0$ is obtained as an eigenvector of the overall sandwiched plate dispersion eigenvalue problem (see §5.3.1 for more details; cf. (3.8)). Explicitly, $\boldsymbol{\eta}_0$ satisfies

$$\mathbf{D}\boldsymbol{\eta}_0 = 0 \text{ with } \mathbf{D} = \mathbf{D}_1^*\mathbf{D}_1 + \mathbf{D}_2^*\mathbf{D}_2, \tag{6.30}$$

where

$$\begin{aligned} \mathbf{D}_1 &\equiv (\widetilde{\mathbf{P}}_i - \mathbf{I})\mathbf{R}_{sls} \text{ and} \\ \mathbf{D}_2 &\equiv (\mathbf{P}_d - \mathbf{I})(z\mathbf{R}_{sls} - \mathbf{I}). \end{aligned} \tag{6.31}$$

Note that we have $\mathbf{R}_{sls}$ in (6.31) in place of $\mathbf{R}_l \equiv \mathbf{R}(d, 0)$ in the original dispersion equation (3.8). Denoting further $\mathbf{R}_f \equiv \mathbf{R}(x_2, -\widetilde{T}_2)$ and $\mathbf{R}_r \equiv \mathbf{R}(d + T_2, x_2)$, we obtain from (6.29) the wave field $\boldsymbol{\eta}(x_2) \equiv (\mathbf{u}(x_2), \boldsymbol{\sigma}(x_2))^T$ for $x_2 \in [-\widetilde{T}_2, d + T_2]$ as

$$\begin{aligned} \boldsymbol{\eta}(x_2) &= \mathbf{M}_{sls}\boldsymbol{\eta}(-\widetilde{T}_2) = \mathbf{M}_{sls}\mathbf{R}_{sls}\boldsymbol{\eta}_0 \\ &= (z\mathbf{R}_f - \mathbf{I})(z(1-z)\mathbf{R}_r\mathbf{R}_f + z\mathbf{R}_r + z\mathbf{R}_f - \mathbf{I})^{-1}\mathbf{R}_r\boldsymbol{\eta}_0, \end{aligned} \tag{6.32}$$

where $\boldsymbol{\eta}_0$ is given by (6.30).

Secondly, the wave field $\boldsymbol{\eta}$ decreasing into the depth of the substrates is calculated by multiplying $\mathbf{M}_d$ and $\widetilde{\mathbf{M}}_{dop}$ with the wave field $\boldsymbol{\eta}(x_2)$ inside the first layer of the substrates, i.e. for $x_2 \in [d, d + T_2]$ and $x_2 \in [-\widetilde{T}_2, 0]$. In the n-th layer of a 2D-periodic (lower and upper) substrate, the wave field is determined via

$$\boldsymbol{\eta}(x_2 + nT_2) = \mathbf{M}_d^n(x_2 + T_2, x_2)\boldsymbol{\eta}(x_2), \;\; x_2 \in [d, d + T_2], \tag{6.33}$$

and

$$\boldsymbol{\eta}(x_2 - n\widetilde{T}_2) = \widetilde{\mathbf{M}}^n_{dop}(x_2 - \widetilde{T}_2, x_2)\boldsymbol{\eta}(x_2), \quad x_2 \in [-\widetilde{T}_2, 0], \tag{6.34}$$

with $\mathbf{M}_d$ and $\widetilde{\mathbf{M}}_{dop}$ defined by (6.26) and (6.27) and with $\boldsymbol{\eta}(x_2)$ given by (6.32).

5.6.3 Numerical examples

We compare the wave fields for two waveguides of the same geometry, but with oppositely chosen materials. First, consider the layer of epoxy located between the two periodic half-spaces consisting of silicium square rods ($r_2 = 0.6$ mm) inside epoxy matrix; see Fig. 5.4 (a). The geometrical parameters are $T_1 = 1$ mm and $T_2 = \widetilde{T}_2 = 1.2$ mm. The layer of thickness $d = L_1 + r_1 + \widetilde{L}_1 = 1.6$ mm includes periodic square rods of silicium ($r_1 = 0.6$ mm) placed at the layer midplane ($L_1 = \widetilde{L}_1 = 0.5$ mm). Displacement field moving along the horizontal axis reaches the highest positive or negative amplitude (depicted in red and blue) in the middle of the waveguide - on the areas of square form corresponding to the soft matrix between the stiff inclusions. Going away from the middle of the waveguide, the behavior of the field remains the same, but its amplitude diminishes considerably (depicted in light green). On the homogeneous soft layers, the displacement field vanishes (depicted in black) or takes minor values (depicted in light green) forming a pattern in the middle of the waveguide or straight lines corresponding to weak propagation without perturbations in the depth of the waveguide. The displacement field vanishes completely (depicted in black) on the stiff inclusions. This behavior detects the rectangular form of inclusions, the (black) areas with zero displacement surrounded by (light green) minor displacement wave field.

Traction field propagates with much more complicated pattern than the displacement field. It has the biggest and lowest amplitude values (depicted in red and blue) on the stiff inclusions, on the interfaces between matrix and inclusions or even on the soft matrix between the inclusions. Like for the displacement field, we see also here the straight

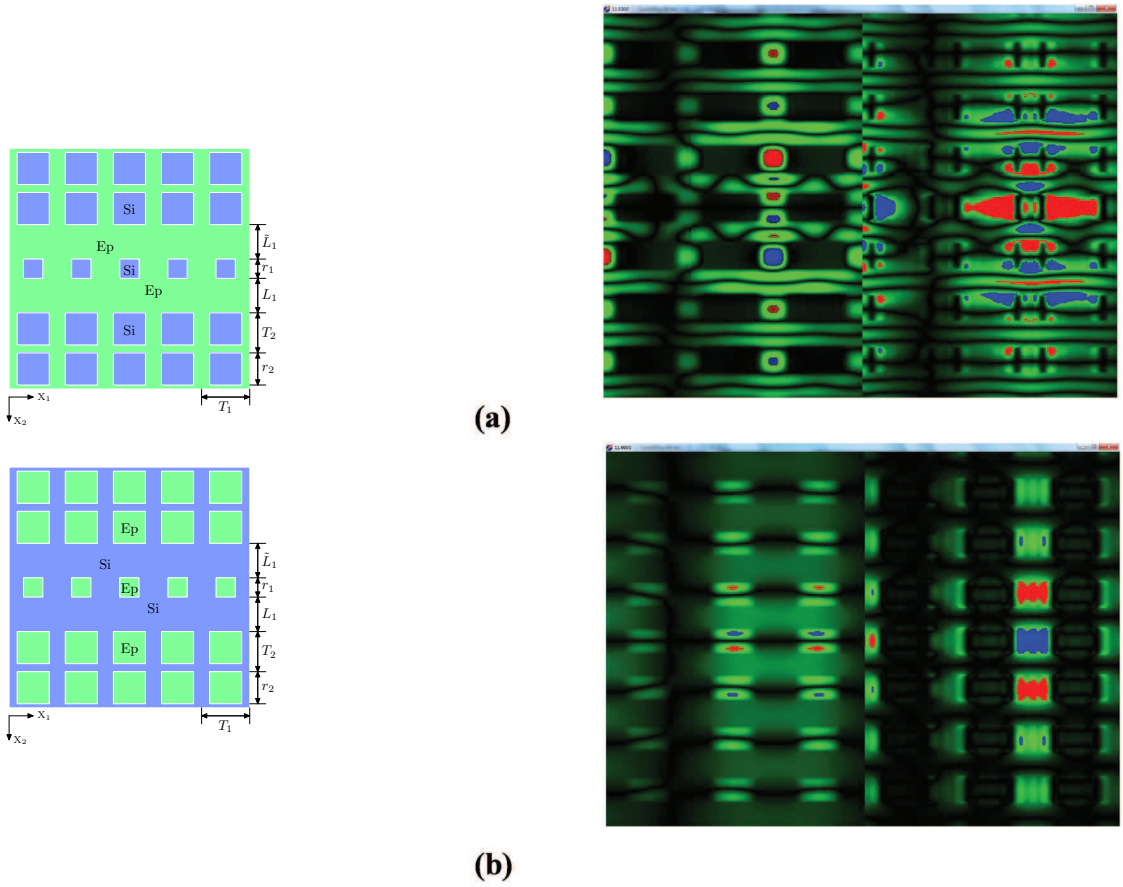

Figure 5.4: The displacement and traction wave fields. The left-hand diagrams show sandwiched plate with laterally periodic square bars with the matrix/inclusions materials (a) Ep/Si and (b) Si/Ep. The right-hand diagrams show the real part of displacement and traction field at the same time, $\mathrm{Re}(u)$ and $\mathrm{Re}(\sigma)$ (left and right part of the diagram, respectively) for the corresponding sandwiched plate with $k_1 T_1 = 0.4\pi$ and (a) $\omega T_1 = 6.86$, (b) $\omega T_1 = 9.36$. Here, black corresponds to zero wave field, green to near-zero (with values (a) $0 < |\mathrm{Re}(u)| < 0.022mm \equiv u_{Re}$, $0 < |\mathrm{Re}(\sigma)| < 0.2GPa \equiv s_{Re}$ and (b) $u_{Re} = 0.007mm$, $s_{Re} = 0.55GPa$) wave field, red and blue (with (a) $u_{Re} < |\mathrm{Re}(u)| < 0.05mm$, $s_{Re} < |\mathrm{Re}(\sigma)| < 1.05GPa$ and (b) $u_{Re} < |\mathrm{Re}(u)| < 0.01mm$, $s_{Re} < |\mathrm{Re}(\sigma)| < 1.5GPa$) to bigger positive and negative wave field amplitudes.

lines of a weaker propagation (depicted in light green) alternated with the domains of zero propagation (depicted in black). The traction field vanishes into the depth of the waveguide taking only minor or zero values (depicted in light green and black).

Secondly, consider the waveguide consistent of silicium matrix and epoxy inclusions; see Fig. 5.4(b). The displacement and traction fields for this waveguide have a much more simple form than in the first example. The wave fields propagate on square domains (depicted in red and blue and clear green) and vanish elsewhere (depicted in black and very clear green). For the displacement field, the square domains of propagation are the soft inclusions, whereas for the traction field, these are the stiff matrix between the inclusions. The amplitudes are the biggest in the middle of the waveguide vanishing into its depth. Therefore also for this waveguide the inclusions are recognized perfectly well.

5.7 Conclusion

The dispersion equation for 2D PC sandwiched plate is stated in terms of the plate resolvent $\mathbf{R}_l$ and two projectors $\mathbf{P}_d$ and $\widetilde{\mathbf{P}}_i$. Here, we keep subscripts 'd' and 'i' for the projectors on the modes decreasing in the direction $x_2 \to +\infty$ and in the opposite direction $x_2 \to -\infty$, respectively. Recall that the modes decreasing in the direction opposite to the direction of reference are given by the projector on the increasing modes. We also use a tilde to distinguish the upper half-space. The technique to state the dispersion equation has two key steps. First consider the plate. Here we substitute the numerically stable resolvent $\mathbf{R}_l$ instead of exponentially growing layer propagator $\mathbf{M}_l$. The ansatz is the same as in the case of Love waves (see Chapter 3). We consider a new initial solution $\widetilde{\boldsymbol{\eta}}$ premultiplied by the resolvent $\mathbf{R}_l$, i.e. $\boldsymbol{\eta} = \mathbf{R}_l\widetilde{\boldsymbol{\eta}}$. The premultiplied solution gives a numerically stable propagated solution $\mathbf{M}_l\boldsymbol{\eta} = \mathbf{M}_l\mathbf{R}_l\widetilde{\boldsymbol{\eta}}$, since the product $\mathbf{M}_l\mathbf{R}_l = z\mathbf{R}_l - \mathbf{I}$ expressed in terms of the resolvent is numerically stable. Secondly consider the lower and upper substrates. Using the projectors $\mathbf{P}_d$ and $\widetilde{\mathbf{P}}_i$, we extract the modes decreasing in the lower and upper half-spaces via $\boldsymbol{\eta} = \mathbf{P}_d\boldsymbol{\eta}$ and $\boldsymbol{\eta} = \widetilde{\mathbf{P}}_i\boldsymbol{\eta}$, respectively. That is, the projector maintains only the chosen type of waves (decreasing or increasing) discarding the others. Moreover, the projection of the spectrum of the propagating waves is given by union of the spectra

in the lower and upper substrates and is calculated via $\mathrm{trace}\,\mathbf{P}_d$ and $\mathrm{trace}\,\widetilde{\mathbf{P}}_i$. If the lower and upper substrates are identical, their projectors and hence their propagating spectra are identical too.

After the general case, the mirror-symmetric sandwiched plate with respect to the horizontal midplane is considered. Similarly as for the plate waves (see Chapter 4), the problem is decomposed for symmetric and anti-symmetric waves giving two independent dispersion equations. Despite the fact that these dispersion equations are not directly related to the overall sandwiched plate dispersion equation, their solutions (zeros) are correlated.

We consider sandwiched plate with identical and dissimilar substrates. The first case gives rise to mirror-symmetry, if the plate is either uniform or have inclusions placed at its midplane. Therefore we observe here the intersection of two independent dispersion spectra for symmetric and anti-symmetric waves hindering the existence of absolute gaps. As soon as the plate inclusions are shifted destroying the mirror symmetry, the branches split and the absolute gap opens up. At the same time, in the case of two dissimilar substrates, the absolute gaps are created regardless of the position of the inclusion. However the symmetric position gives a smaller gap.

The displacement and traction field is calculated in two steps. First, the wave field is calculated inside the plate and the surrounding layers of the upper and lower substrates - analogously like for the free plate (see Chapter 4) in terms of resolvents, since this method is independent from boundary conditions (either with traction or traction-free). Secondly, the wave field into the depth of the substrates is obtained by introducing the propagator $\mathbf{M}_d$ for decreasing modes (in the lower substrate) and the propagator $\widetilde{\mathbf{M}}_{dop}$ for decreasing modes in the opposite direction (in the upper substrate). Defined as the modified projector $\mathbf{P}_d$, the propagators $\mathbf{M}_d$ and $\widetilde{\mathbf{M}}_{dop}$ give the wave field at any depth of the periodic substrate from the initial field in its first layer: $\boldsymbol{\eta}(x_2 + nT_2) = \mathbf{M}_d^n(x_2 + T_2, x_2)\boldsymbol{\eta}(x_2)$ with $x_2 \in [d, d + T_2]$.

Chapter 6

Conclusions

We propose a new calculation method of the dispersion spectrum and wave field in 2D PC called the resolvent method. To approach this topic gradually, we begin with 1D PC. In this case, it is possible to compute the dispersion spectrum in an easier way, which sums up in the scalar impedance method.

The impedance method is applied to Love waves in the 1D PC coated substrate. The dispersion equation is stated as equality of scalar SH impedances of the coating layer and the substrate. Rigorous mathematical derivation demonstrates some helpful properties of the impedance functions giving several advantages of the method in comparison to the commonly used formulation via the transfer matrix. First of all, monotonicity of impedance functions in ω and k_x enables insightful graphical visualization of roots of the dispersion equation and clarify the connectivity of the broken branches of Love waves. Next, the behavior of the impedance functions underpins the relation of the number of Love waves in a stopband to the number of resonances of the coating layer. Moreover, the impedance method can be extended to the case of vector waves in a coated periodic substrate and/or in a periodic medium with different models of an embedded defect layer; see e.g. [10].

We also illustrate the observed spectral phenomena by means of diverse numerical ex-

amples contrasting them with the spectra of other PC structures. The dispersion spectrum of a 1D PC coated substrate is compared, first, to the classical case of a homogeneous substrate coated by a homogeneous or 1D layer and, secondly, to the 1D PC (uncoated) substrate. There are several differences. For instance, a periodic substrate, in contrast to a homogeneous one, admits localized waves emerging with finite frequencies at $k_x = 0$. A general dissimilarity between Love and surface waves is that any stopband at fixed k_x cannot contain more than one SH surface wave whereas it may contain several Love waves (about as many, as many resonances of the coating layer fall within this stopband). Another significant effect of coating arises in a fairly typical case where a free periodic substrate admits SH surface waves only in a narrow velocity range - then even a weak perturbation by thin coating creates localised waves in the spectral domain where they could not exist for the uncoated substrate.

The method based on the resolvent of propagator is developed and applied to calculation of the dispersion spectra and wave field of shear horizontal waves in the 2D PC coated substrates, the PC free plates and sandwiched plates. The background of the method consists of the Fourier expansion in the lateral coordinate and of the exact differential equation in the depth direction. One could have taken the equation for the propagator (monodromy matrix $\mathbf{M}$); however this approach is not satisfactory because the propagator is numerically unstable - it exponentially grows as the number of Fourier harmonics increases. In this regard, our method replaces the propagator by the numerically stable object, the resolvent $\mathbf{R}$, which is formally related to the propagator as $\mathbf{R} = (z\mathbf{I} - \mathbf{M})^{-1}$. The resolvent is the solution of the Riccati differential equation in the depth direction. Its calculation can be essentially simplified if the medium is at least partially homogeneous into the depth.

The dispersion equation for diverse PC waveguides consisting of layer(s) and one or two half-spaces can be formulated via three tools, the resolvent $\mathbf{R}_l$ of the layer(s), the projector $\mathbf{P}_d$ on the decreasing modes in the first half-space and eventually the projector $\mathbf{P}_i$

on the modes decreasing in the second half-space. We apply the resolvent tool $\mathbf{R}_l$ for the plate or coating and the projector tool (defined in terms of the substrate resolvent $\mathbf{R}_s$) for the substrate. By these means the problem is always reduced to a single unit cell of the 2D periodic structure. The technique to state the dispersion equation has two key steps. First consider a layer. Here we substitute the numerically stable resolvent $\mathbf{R}_l$ instead of exponentially growing layer propagator $\mathbf{M}_l$. The substitution can follow either directly (plate waves, see Chapter 4) or by a premultiplying (Love waves and guided waves, see Chapters 3 and 5). The last case consists of considering a new initial solution $\widetilde{\boldsymbol{\eta}}$ premultiplied by the resolvent $\mathbf{R}$, i.e. $\boldsymbol{\eta} = \mathbf{R}\widetilde{\boldsymbol{\eta}}$. The premultiplied solution gives a numerically stable propagated solution $\mathbf{M}\boldsymbol{\eta} = \mathbf{M}\mathbf{R}\widetilde{\boldsymbol{\eta}}$, since the product $\mathbf{MR} = z\mathbf{R} - \mathbf{I}$ expressed in terms of the resolvent is numerically stable. Secondly consider a substrate. The decreasing solution $\boldsymbol{\eta}$ is extracted applying the projector $\mathbf{P}_d$ on the decreasing modes by imposing the equality $\boldsymbol{\eta} = \mathbf{P}_d\boldsymbol{\eta}$. That is, a projector can be considered as a kind of filter maintaining only the chosen kind of waves (decreasing or propagating) and discarding the rest. Analytical properties of the resolvent and, in the case of a substrate and a waveguide, of the projector are presented and several options for calculation of the resolvent and projector are provided (see Appendix).

We calculate the wave field for the PC waveguides by extending the method developed for the dispersion equation. The displacement and traction field for PC structures consisting of layer(s) and one or two half-spaces can be formulated via three tools, the resolvent $\mathbf{R}_l$ of the layer(s), the propagator $\mathbf{M}_d$ for the decreasing modes in the first half-space and eventually the propagator $\widetilde{\mathbf{M}}_{dop}$ for the modes decreasing in the opposite direction in the second half-space. First, we take the solution of the dispersion equation for the overall PC structure discussed above as the initial wave field. Next, we calculate the propagating wave field by 'moving' our tools inside the structure. For example, we consider the resolvent $\mathbf{R}(x_2, 0)$ with any $x_2 \in [0, d]$ instead of the layer resolvent $\mathbf{R}(d, 0)$ and the propagator $\mathbf{M}_d(x_2 + T_2, x_2)$ with any $x_2 \in [d, d + T_2]$ instead of the substrate projector

$\mathbf{P}_d(T_2, d)$. First consider a plate (either sandwiched or traction-free), since this method is independent from boundary conditions (Chapters 4 and 5). Here the wave field is calculated in terms of resolvents. Recasting the initial field $\boldsymbol{\eta}(0)$ in terms of the resolvent $\mathbf{R}(d, 0)$ of the whole plate as $\boldsymbol{\eta}(0) = \mathbf{R}(d, 0)\widetilde{\boldsymbol{\eta}}(0)$ yields a numerically stable expression $\boldsymbol{\eta}(x_2) = \mathbf{M}(x_2, 0)\mathbf{R}(d, 0)\widetilde{\boldsymbol{\eta}}(0)$ for the propagating field. The crucial point here is that the product $\mathbf{M}(x_2, 0)\mathbf{R}(d, 0)$ is numerically stable for $x_2 \in [0, d]$, since we can decompose $\mathbf{R}(d, 0)$ into $\mathbf{R}(d, x_2)$ and $\mathbf{R}(x_2, 0)$ using the resolvent chain rule. Secondly consider a substrate (Chapter 5). The wave field $\boldsymbol{\eta}(x_2)$ with $x_2 \in [d, d + T_2]$ inside the first layer of the substrate is calculated like for the free plate in terms of resolvents. The wave field in the further layers decreasing into the depth of the substrates is obtained by introducing the propagator $\mathbf{M}_d$ for decreasing modes (in the lower substrate) and the propagator $\widetilde{\mathbf{M}}_{dop}$ for decreasing modes in the opposite direction (in the upper substrate). Defined as the modified projector $\mathbf{P}_d$, the propagators $\mathbf{M}_d$ and $\widetilde{\mathbf{M}}_{dop}$ give the wave field at any depth of the periodic substrate from the initial field in its first layer. For example, in the n-th layer of a 2D-periodic substrate, the wave field is determined via $\boldsymbol{\eta}(x_2+nT_2) = \mathbf{M}_d^n(x_2+T_2, x_2)\boldsymbol{\eta}(x_2)$, where $x_2 \in [d, d + T_2]$. Note that also the field of Love waves can be calculated using this technique.

The method deriving simple dispersion and wave field equations with different computational features (Riccatti equation, contour integral, matrix function) has several advantages. First, it is fast and stable thanks to the resolvent circumventing the instabilities of the propagator. Secondly, it gives a good precision: exact solution into the depth gives better accuracy than the plane-wave expansion method which implies Fourier expansion in each coordinate. Thirdly, the method is relatively computationally cheap in comparison e.g. with the supercell method, since we reduce consequently the problems for the periodic structures to their unit cells, whereas the supercell method requires several unit cells for the same purpose. Fourthly, the method is versatile, multifunctional and extendible in the following sense. It is versatile, since it covers the broad frequency

range and the diversity of media, e.g. 2D-uniform, depth-uniform, 2D-heterogeneous. Next, the method is multifunctional, since it can be applied to different kinds of problems in phononic crystals with various interfaces, e.g. layer on a half-space, layer between two half-spaces. Finally, it is extendible to vector waves and three-dimensional phononic crystals. Moreover, the resolvent (like the propagator) does not depend on the boundary conditions and hence allows the old discretized data to be used for a further calculation of a better precision in contrast to the iterative methods.

Note that the Fourier series expansion limits the application of the method on the other types of phononic plates as fluid/solid, solid/fluid or solid with void inclusions. A possible solution is to take other basis functions instead of the Fourier.

The numerical examples were obtained by means of Embarcadero Delphi Xe with the use of MtxVec component which provides highly optimized BLAS and LAPACK linear algebra routines.

Our physical observations reveal absolute low-frequency band gaps. It is shown that the low-frequency dispersion branches may either cross or repulse each other, the latter leading to the low-frequency band gaps inside the Brillouin zone. They are the bigger, the closer are the inclusions to the traction-free surface and the bigger are the inclusions themselves. For the PC with substrates (see Chapter 3 and 5), the projection of the spectrum of the propagating waves is traced and the spectrum of localized waves is studied. It has been shown for such structures that the inclusions in the substrate do not have a big influence on a localized spectrum. Next, a special attention is paid to mirror-symmetric profiles (see Chapter 4 and 5). The stop bands arise by the repulsion of dispersion branches at their former intersections at the edge of the Brillouin zone for mirror-symmetric profile and at the edge and inside the Brillouin zone for asymmetric profile.

In numerical examples for the wave field, we consider the waveguides with highly contrasting matrix/inclusions stiffness values. This allows us to recognize well the PC geometry by observing the amplitudes of the displacement and traction fields. For exam-

ple, a stiff inclusion in a soft matrix can be detected as an area with zero displacement values and at the same time maximal traction field values.

Appendix A

Useful identities for the propagator, resolvent and projector

A.1 Chain rule and Hilbert identity for resolvent

For any a, b, c, we have the chain rule for the propagator

$$\mathbf{M}(c,a) = \mathbf{M}(c,b)\mathbf{M}(b,a). \tag{A.1.1}$$

The resolvent satisfies the chain rule in the following form. Having two resolvents $\mathbf{R}(b,a) = (z\mathbf{I} - \mathbf{M}(b,a))^{-1}$ and $\mathbf{R}(c,b) = (z\mathbf{I} - \mathbf{M}(c,b))^{-1}$ at hand, the aggregate resolvent

$$\mathbf{R}(c,a) = (z\mathbf{I} - \mathbf{M}(c,b)\mathbf{M}(b,a))^{-1} \tag{A.1.2}$$

is given by

$$\begin{aligned} \mathbf{R}(c,a) &= (z\mathbf{I} - (z\mathbf{I} - \mathbf{R}^{-1}(c,b))(z\mathbf{I} - \mathbf{R}^{-1}(b,a)))^{-1} \\ &= \mathbf{R}(b,a)(z(1-z)\mathbf{R}(c,b)\mathbf{R}(b,a) + z\mathbf{R}(c,b) + z\mathbf{R}(b,a) - \mathbf{I})^{-1}\mathbf{R}(c,b), \end{aligned} \tag{A.1.3}$$

avoiding unstable term $\mathbf{R}^{-1}$.

If one resolvent $\mathbf{R}_\alpha(b,a) = (\alpha\mathbf{I} - \mathbf{M}(b,a))^{-1}$ for a fixed α is known, then we can easily calculate a resolvent $\mathbf{R}_\beta(b,a) = (\beta\mathbf{I} - \mathbf{M}(b,a))^{-1}$ for any β by using identity

$$\mathbf{R}_\beta(b,a) = \mathbf{R}_\alpha(b,a)\Big(\mathbf{I} - (\alpha-\beta)\mathbf{R}_\alpha(b,a)\Big)^{-1}. \tag{A.1.4}$$

Equation (A.1.4) follows from the Hilbert identity (also called the first resolvent identity)

$$\mathbf{R}_\beta(b,a) - \mathbf{R}_\alpha(b,a) = (\alpha-\beta)\mathbf{R}_\beta(b,a)\mathbf{R}_\alpha(b,a). \tag{A.1.5}$$

The latter can be proved by premultiplying both sides of (A.1.5) by $\mathbf{R}_\beta^{-1}(b,a) = \beta\mathbf{I} - \mathbf{M}(b,a)$ from the left and by $\mathbf{R}_\alpha^{-1}(b,a) = \alpha\mathbf{I} - \mathbf{M}(b,a)$ from the right.

A.2 T-unitarity of the propagator and its consequences

The propagator can be calculated as a multiplicative Volterra integral

$$\mathbf{M}(b,a) = \widehat{\int_a^b}(\mathbf{I} + \mathbf{Q}(x_2)dx_2) = \lim_{n\to\infty}\left(\mathbf{I} + \frac{1}{n}\mathbf{Q}\left(a + n\frac{b-a}{n}\right)\right)\ldots\left(\mathbf{I} + \frac{1}{n}\mathbf{Q}\left(a + 0\frac{b-a}{n}\right)\right),$$

where $b > a$. The inverse propagator is

$$\begin{gathered}
\mathbf{M}(a,b) = \mathbf{M}^{-1}(b,a) = \widehat{\int_b^a}(\mathbf{I} + \mathbf{Q}(x_2)dx_2) = \\
\lim_{n\to\infty}\left(\mathbf{I} - \tfrac{1}{n}\mathbf{Q}\left(a + 0\tfrac{b-a}{n}\right)\right)\ldots\left(\mathbf{I} - \tfrac{1}{n}\mathbf{Q}\left(a + n\tfrac{b-a}{n}\right)\right) = \\
\lim_{n\to\infty}\left(\left(\mathbf{I} + \mathbf{T}\tfrac{1}{n}\mathbf{Q}\left(a + n\tfrac{b-a}{n}\right)\mathbf{T}^{-1}\right)\ldots\left(\mathbf{I} + \mathbf{T}\tfrac{1}{n}\mathbf{Q}\left(a + 0\tfrac{b-a}{n}\right)\mathbf{T}^{-1}\right)\right)^* = \\
\mathbf{T}\left(\lim_{n\to\infty}\left(\mathbf{I} + \tfrac{1}{n}\mathbf{Q}\left(a + n\tfrac{b-a}{n}\right)\right)\ldots\left(\mathbf{I} + \tfrac{1}{n}\mathbf{Q}\left(a + 0\tfrac{b-a}{n}\right)\right)\right)^*\mathbf{T}^{-1} = \\
\mathbf{T}\mathbf{M}^*(b,a)\mathbf{T}^{-1},
\end{gathered} \tag{A.2.1}$$

where * is Hermitian conjugation and we have used that $\mathbf{Q}$ defined in (2.3) with real μ and ρ is symplectic

$$\mathbf{Q} = -\mathbf{T}\mathbf{Q}^*\mathbf{T}^{-1} \text{ with } \mathbf{T} = -\mathbf{T}^* = -\mathbf{T}^{-1} = \begin{pmatrix} \mathbf{0} & \mathbf{I} \\ -\mathbf{I} & \mathbf{0} \end{pmatrix}. \tag{A.2.2}$$

Thus identities (A.2.1) amount to $\mathbf{T}$-unitarity of the propagator

$$\mathbf{M}^{-1}(b,a) = \mathbf{T}\mathbf{M}^*(b,a)\mathbf{T}^{-1}. \tag{A.2.3}$$

In particular, (A.2.3) yields that the sets of eigenvalues of $\mathbf{M}^{-1}$ and $\mathbf{M}^*$ are identical consisting of $q_d,\ q_p$ and q_i with

$$q_i^{-1} = q_d^* \text{ and } q_p^{-1} = q_p^*,$$

$$\dim E_i = \dim E_d \text{ and } \dim E_p \in 2\mathbb{Z}. \tag{A.2.4}$$

$\mathbf{T}$-unitarity (A.2.3) of the propagator leads via

$$\mathbf{R}^*_\alpha(b,a) = \mathbf{T}(\overline{\alpha} - \mathbf{M}^{-1}(b,a))^{-1}\mathbf{T}^{-1}, \tag{A.2.5}$$

where $\overline{\alpha}$ denotes complex conjugated value of α, to the corresponding identity

$$\mathbf{R}_\alpha(a,b) = \mathbf{T}\mathbf{R}^*_{\overline{\alpha}}(b,a)\mathbf{T}^{-1} \tag{A.2.6}$$

for the resolvent. Next, note that the projector on the increasing modes $\mathbf{P}_i$ is identical to the projector $\mathbf{P}_{dop}$ on the decreasing modes in the opposite direction, since

$$\mathbf{P}_i = \mathbf{I} - \frac{1}{2\pi i}\oint_{|z|=1+0}(z\mathbf{I} - \mathbf{M})^{-1}dz = \mathbf{I} - \frac{1}{2\pi i}\oint_{|z|=1+0}(z\mathbf{M}^{-1} - \mathbf{I})^{-1}\mathbf{M}^{-1}dz$$

$$= \mathbf{I} - \frac{1}{2\pi i} \oint_{|z|=1+0} z^{-1}(z\mathbf{M}^{-1} - \mathbf{I})^{-1}(z\mathbf{M}^{-1} - \mathbf{I} + \mathbf{I})dz$$

$$= \mathbf{I} - \frac{1}{2\pi i} \oint_{|z|=1+0} z^{-1}\mathbf{I}dz - \frac{1}{2\pi i} \oint_{|z|=1+0} z^{-1}(z\mathbf{M}^{-1} - \mathbf{I})^{-1}dz$$

$$= \mathbf{I} - \mathbf{I} - \frac{1}{2\pi i} \oint_{|z|=1+0} z^{-2}(\mathbf{M}^{-1} - z^{-1}\mathbf{I})^{-1}dz$$

$$= -\frac{1}{2\pi i} \oint_{|z|=1+0} z^{-2}(\mathbf{M}^{-1} - z^{-1}\mathbf{I})^{-1}dz = \frac{1}{2\pi i} \oint_{|z|=1+0} (\mathbf{M}^{-1} - z^{-1}\mathbf{I})^{-1}d(z^{-1})$$

$$= -\frac{1}{2\pi i} \oint_{|z|=1-0} (\mathbf{M}^{-1} - z\mathbf{I})^{-1}dz = \frac{1}{2\pi i} \oint_{|z|=1-0} (z\mathbf{I} - \mathbf{M}^{-1})^{-1}dz \equiv \mathbf{P}_{dop}. \tag{A.2.7}$$

Using (A.2.7) and applying the resolvent identity (A.2.6) for the substrate resolvent $\mathbf{R}_z(T_2, 0)$ over the depth period T_2 implies for the projectors

$$\mathbf{P}_i = \mathbf{P}_{dop} = \frac{1}{2\pi i} \oint_{|z|=1-0} \mathbf{R}_z(0, T_2)dz = \frac{1}{2\pi i} \oint_{|z|=1-0} \mathbf{T}\mathbf{R}^*_{\overline{z}}(T_2, 0)\mathbf{T}^{-1}dz$$

$$= \mathbf{T}\left(\frac{1}{2\pi i} \oint_{|z|=1-0} \mathbf{R}^*_{\overline{z}}(T_2, 0)dz\right)\mathbf{T}^{-1} = \mathbf{T}\left(-\frac{1}{2\pi i} \oint_{|z|=1-0} \mathbf{R}_{\overline{z}}(T_2, 0)d\bar{z}\right)^*\mathbf{T}^{-1}$$

$$= \mathbf{T}\left(\frac{1}{2\pi i} \oint_{|z|=1-0} \mathbf{R}_z(T_2, 0)dz\right)^*\mathbf{T}^{-1} = \mathbf{T}\mathbf{P}^*_d\mathbf{T}^{-1}. \tag{A.2.8}$$

From (A.2.8), it follows that the set of the eigenvalues of $\mathbf{P}_i$ and $\mathbf{P}^*_d$ is identical. In other words,

$$\operatorname{trace}\mathbf{P}_i = \operatorname{trace}\mathbf{P}^*_d = \operatorname{trace}\mathbf{P}_d. \tag{A.2.9}$$

Therefore in our case, already the projector $\mathbf{P}_d$ on the decreasing modes contains all the information about decreasing, increasing and propagating modes thanks to the fact that the system matrix $\mathbf{Q}$ is symplectic and using the projector sum identity (4.30). Explicitly,

$$\begin{gathered}\mathbf{P}_i = \mathbf{T}\mathbf{P}^*_d\mathbf{T}^{-1}, \;\; \mathbf{P}_p = \mathbf{I} - \mathbf{P}_d - \mathbf{T}\mathbf{P}^*_d\mathbf{T}^{-1} \\ \text{and} \;\; \operatorname{trace}\mathbf{P}_p = 2(2N+1) - 2\operatorname{trace}\mathbf{P}_d.\end{gathered} \tag{A.2.10}$$

A.3 Mirror-symmetric sublayers

Consider two sublayers $x_2 \in [a_1, b_1]$ and $x_2 \in [a_2, b_2]$ of the same length $d = b_1 - a_1 = b_2 - a_2$ and with the property that one is the reflection of the other:

$$\mathbf{Q}(a_1 + x_2) = \mathbf{Q}(b_2 - x_2), \;\; x_2 \in [0, d]. \tag{A.3.1}$$

The identity (A.2.1) with (A.3.1) for the reflected propagator gives us

$$\begin{gathered}
\mathbf{M}^{-1}(b_1, a_1) = \lim_{n\to\infty}\left(\mathbf{I} - \tfrac{1}{n}\mathbf{Q}\left(a_1 + 0\tfrac{d}{n}\right)\right)...\left(\mathbf{I} - \tfrac{1}{n}\mathbf{Q}\left(a_1 + n\tfrac{d}{n}\right)\right) = \\
\lim_{n\to\infty}\left(\mathbf{I} - \tfrac{1}{n}\mathbf{Q}\left(a_2 + n\tfrac{d}{n}\right)\right)...\left(\mathbf{I} - \tfrac{1}{n}\mathbf{Q}\left(a_2 + 0\tfrac{d}{n}\right)\right) = \\
\lim_{n\to\infty}\left(\mathbf{I} + \mathbf{S}\tfrac{1}{n}\mathbf{Q}\left(a_2 + n\tfrac{d}{n}\right)\mathbf{S}^{-1}\right)...\left(\mathbf{I} + \tfrac{1}{n}\mathbf{S}\mathbf{Q}\left(a_2 + 0\tfrac{d}{n}\right)\mathbf{S}^{-1}\right) = \\
\mathbf{S}\lim_{n\to\infty}\left(\mathbf{I} + \tfrac{1}{n}\mathbf{Q}\left(a_2 + n\tfrac{d}{n}\right)\right)...\left(\mathbf{I} + \tfrac{1}{n}\mathbf{Q}\left(a_2 + 0\tfrac{d}{n}\right)\right)\mathbf{S}^{-1} = \mathbf{S}\mathbf{M}(b_2, a_2)\mathbf{S}^{-1},
\end{gathered} \tag{A.3.2}$$

where we have used that $\mathbf{Q}$ given in (2.3) satisfies

$$-\mathbf{Q} = \mathbf{S}\mathbf{Q}\mathbf{S}^{-1} \;\text{ for }\; \mathbf{S} = \mathbf{S}^{-1} = \begin{pmatrix} \mathbf{I} & \mathbf{0} \\ \mathbf{0} & -\mathbf{I} \end{pmatrix}. \tag{A.3.3}$$

The identities (A.3.2) amount to

$$\mathbf{M}^{-1}(b_1, a_1) = \mathbf{S}\mathbf{M}(b_2, a_2)\mathbf{S}^{-1} \tag{A.3.4}$$

which implies

$$\mathbf{M}(a_1, b_1) = \mathbf{S}\mathbf{M}(b_2, a_2)\mathbf{S}^{-1} = \mathbf{S}\begin{pmatrix} \mathbf{M}_1 & \mathbf{M}_2 \\ \mathbf{M}_3 & \mathbf{M}_4 \end{pmatrix}\mathbf{S}^{-1} = \begin{pmatrix} \mathbf{M}_1 & -\mathbf{M}_2 \\ -\mathbf{M}_3 & \mathbf{M}_4 \end{pmatrix}. \tag{A.3.5}$$

Using (A.3.5) with (A.2.6) we obtain the following identity for the direct and reflected resolvents

$$\mathbf{R}_\alpha(b_1,a_1)=\mathbf{J}\mathbf{R}^*_{\overline{\alpha}}(b_2,a_2)\mathbf{J}\ \text{ with }\ \mathbf{J}=\mathbf{J}^{-1}=\mathbf{S}\mathbf{T}=\begin{pmatrix}\mathbf{0} & \mathbf{I}\\ \mathbf{I} & \mathbf{0}\end{pmatrix}. \tag{A.3.6}$$

Consider two semi-infinite periodic profiles $(-\infty,a)$ (direct) and (b,∞) (reflected) and denote the propagator through period and projectors for the reflected layer with symbol $\widetilde{\ }$. Then for the direct and reflected projectors we have the following identities

$$\widetilde{\mathbf{P}}_d=\frac{1}{2\pi i}\oint\limits_{|z|=1-0}(z-\widetilde{\mathbf{M}})^{-1}dz=\mathbf{S}\frac{1}{2\pi i}\oint\limits_{|z|=1-0}(z-\mathbf{M}^{-1})^{-1}dz\mathbf{S}^{-1}=\mathbf{S}\mathbf{P}_i\mathbf{S}^{-1}. \tag{A.3.7}$$

Appendix B

Explicit formulas for propagator, resolvent, and projector of the uniform layer

This section demonstrates that the propagator $\mathbf{M}$ grows exponentially with growing size of $\mathbf{M}$ while the resolvent $\mathbf{R}$ grows only linearly. Besides, the formulas obtained herein will be used in Appendix C in the case, where 2D layer includes uniform sublayer(s) or a half-space is uniform.

Consider the uniform layer with the constant stiffness μ and the constant density ρ formally as periodic in x_1. Then the system matrix has the following form

$$\mathbf{Q} = \begin{pmatrix} \mathbf{0} & \mathbf{Q}_2 \\ \mathbf{Q}_3 & \mathbf{0} \end{pmatrix} \quad \text{with} \quad \mathbf{Q}_2 = \mu^{-1}\mathbf{I}, \quad \mathbf{Q}_3 = \operatorname*{diag}_{-N\leqslant j\leqslant N}(\mu\theta_j), \quad \theta_j = (2\pi j + k_1)^2 - \frac{\omega^2\rho}{\mu}, \quad \text{(B.0.1)}$$

where $\mathbf{I}$ is $(2N+1)\times(2N+1)$ identity matrix. The matrix $\mathbf{Q}$ admits another useful

representation, namely,

$$\mathbf{Q} = \mathbf{U} \operatorname*{diag}_{-N\leqslant j\leqslant N}(\mathbf{q}_j)\mathbf{U}^{-1}, \text{ where } \mathbf{q}_j = \begin{pmatrix} 0 & \mu^{-1} \\ \mu\theta_j & 0 \end{pmatrix} \text{ and} \tag{B.0.2}$$

$$\mathbf{U} = (u_{nm})_{n,m=1}^{2(2N+1)}, \ u_{nm} = \begin{cases} \delta_{n,\frac{m+1}{2}}, & \text{if } n \leqslant 2N+1 \\ \delta_{n-2N-1,\frac{m}{2}}, & \text{if } n > 2N+1 \end{cases}, \tag{B.0.3}$$

where δ_{pq} denotes the Kronecker symbol for rational numbers p, q and $\operatorname{diag}(\mathbf{q}_j)$ is the matrix with diagonal blocks $\mathbf{q}_j$. The propagator through this layer of the depth l is given by

$$\mathbf{M} = \exp(l\mathbf{Q}) = \mathbf{U} \operatorname*{diag}_{-N\leqslant j\leqslant N}(\mathbf{m}_j)\mathbf{U}^{-1} = \begin{pmatrix} \mathbf{M}_1 & \mathbf{M}_2 \\ \mathbf{M}_3 & \mathbf{M}_1 \end{pmatrix} \text{ with} \tag{B.0.4}$$

$$\mathbf{m}_j = \exp(l\mathbf{q}_j) = \begin{pmatrix} \cosh l\sqrt{\theta_j} & \frac{\sinh l\sqrt{\theta_j}}{\mu\sqrt{\theta_j}} \\ \mu\sqrt{\theta_j}\sinh l\sqrt{\theta_j} & \cosh l\sqrt{\theta_j} \end{pmatrix} \text{ and } \mathbf{M}_1 = \operatorname*{diag}_{-N\leqslant j\leqslant N}(\cosh l\sqrt{\theta_j}), \tag{B.0.5}$$

$$\mathbf{M}_2 = \operatorname*{diag}_{-N\leqslant j\leqslant N}\left(\frac{\sinh l\sqrt{\theta_j}}{\mu\sqrt{\theta_j}}\right), \ \mathbf{M}_3 = \operatorname*{diag}_{-N\leqslant j\leqslant N}(\mu\sqrt{\theta_j}\sinh l\sqrt{\theta_j}). \tag{B.0.6}$$

Note the exponential growth of the propagator matrix $\mathbf{M}$ components with the growing index j of the Fourier harmonic. Using the block inversion formula, we obtain the following explicit form for the resolvent

$$\mathbf{R} = (z\mathbf{I} - \mathbf{M})^{-1} = \mathbf{U} \operatorname*{diag}_{-N\leqslant j\leqslant N}(\mathbf{r}_j)\mathbf{U}^{-1} = \begin{pmatrix} \mathbf{R}_1 & \mathbf{R}_2 \\ \mathbf{R}_3 & \mathbf{R}_1 \end{pmatrix}, \tag{B.0.7}$$

$$\text{where } \mathbf{r}_j = (z - \mathbf{m}_j)^{-1} = \begin{pmatrix} r_{1j} & r_{2j} \\ r_{3j} & r_{1j} \end{pmatrix} \text{ and} \tag{B.0.8}$$

$$\mathbf{R}_1 = \underset{-N\leqslant j\leqslant N}{\operatorname{diag}}(r_{1j}),\quad r_{1j} = \begin{cases} \frac{z-\cos l\sqrt{|\theta_j|}}{z^2-2z\cos l\sqrt{|\theta_j|}+1}, & \theta_j \leqslant 0 \\ \frac{z\operatorname{sech} l\sqrt{\theta_j}-1}{(z^2+1)\operatorname{sech} l\sqrt{\theta_j}-2z}, & \theta_j > 0 \end{cases}, \tag{B.0.9}$$

$$\mathbf{R}_2 = \underset{-N\leqslant j\leqslant N}{\operatorname{diag}}(r_{2j}),\quad r_{2j} = \begin{cases} \frac{\sin l\sqrt{|\theta_j|}}{\mu\sqrt{|\theta_j|}(z^2-2z\cos l\sqrt{|\theta_j|}+1)}, & \theta_j \leqslant 0 \\ \frac{\tanh l\sqrt{\theta_j}}{\mu\sqrt{\theta_j}((z^2+1)\operatorname{sech} l\sqrt{\theta_j}-2z)}, & \theta_j > 0 \end{cases}, \tag{B.0.10}$$

$$\mathbf{R}_3 = \underset{-N\leqslant j\leqslant N}{\operatorname{diag}}(r_{3j}),\quad r_{3j} = \begin{cases} \frac{\mu\sqrt{|\theta_j|}\sin l\sqrt{|\theta_j|}}{z^2-2z\cos l\sqrt{|\theta_j|}+1}, & \theta_j \leqslant 0 \\ \frac{\mu\sqrt{\theta_j}\tanh l\sqrt{\theta_j}}{(z^2+1)\operatorname{sech} l\sqrt{\theta_j}-2z}, & \theta_j > 0 \end{cases}. \tag{B.0.11}$$

Therefore we see that the inversion of the resolvent block $\mathbf{R}_1$ is numerically stable, whereas that of $\mathbf{R}_2$ and $\mathbf{R}_3$ is not. The reason for it is, in simple words, that the shift by z is not involved in the numerators of $\mathbf{R}_2$ and $\mathbf{R}_3$. The components of the resolvent $\mathbf{R}$ can have only linear growth for $j \to \infty$. Finally, the projector $\mathbf{P} \equiv \mathbf{P}_d$ on decreasing modes (see the definition of g_d in (C.2.1)) has the following explicit form

$$\mathbf{P} = g_d(\mathbf{Q}) = \mathbf{U} \underset{-N\leqslant j\leqslant N}{\operatorname{diag}}(\mathbf{p}_j)\mathbf{U}^{-1} = \begin{pmatrix} \mathbf{P}_1 & \mathbf{P}_2 \\ \mathbf{P}_3 & \mathbf{P}_1 \end{pmatrix}, \text{ where} \tag{B.0.12}$$

$$\begin{aligned} \mathbf{p}_j = g_d(\mathbf{q}_j) &= \begin{pmatrix} \mu^{-1} & \mu^{-1} \\ \sqrt{\theta_j} & -\sqrt{\theta_j} \end{pmatrix} \begin{pmatrix} g_d(\sqrt{\theta_j}) & 0 \\ 0 & g_d(-\sqrt{\theta_j}) \end{pmatrix} \begin{pmatrix} \frac{\mu}{2} & \frac{1}{2\sqrt{\theta_j}} \\ \frac{\mu}{2} & \frac{-1}{2\sqrt{\theta_j}} \end{pmatrix} = \\ &= \begin{pmatrix} \mu^{-1} & \mu^{-1} \\ \sqrt{\theta_j} & -\sqrt{\theta_j} \end{pmatrix} \begin{pmatrix} 0 & 0 \\ 0 & H(\theta_j) \end{pmatrix} \begin{pmatrix} \frac{\mu}{2} & \frac{1}{2\sqrt{\theta_j}} \\ \frac{\mu}{2} & \frac{-1}{2\sqrt{\theta_j}} \end{pmatrix} = \\ &= H(\theta_j) \begin{pmatrix} \frac{1}{2} & \frac{-1}{2\mu\sqrt{\theta_j}} \\ \frac{-\mu\sqrt{\theta_j}}{2} & \frac{1}{2} \end{pmatrix} \quad \text{and} \quad \mathbf{P}_1 = \underset{-N\leqslant j\leqslant N}{\operatorname{diag}}\left(\frac{H(\theta_j)}{2}\right), \end{aligned} \tag{B.0.13}$$

$$\mathbf{P}_2 = \underset{-N\leqslant j\leqslant N}{\operatorname{diag}}\left(\frac{-H(\theta_j)}{2\mu\sqrt{\theta_j}}\right),\ \ \mathbf{P}_3 = \underset{-N\leqslant j\leqslant N}{\operatorname{diag}}\left(\frac{-H(\theta_j)\mu\sqrt{\theta_j}}{2}\right),$$
$$H(x) = \begin{cases} 0, & x \leqslant 0 \\ 1, & x > 0. \end{cases} \tag{B.0.14}$$

Appendix C

Options for calculation of the resolvent, projector and propagator for decreasing modes

C.1 Options for calculation of the resolvent

In general, the resolvent for the layer can be computed as a root of the Riccati equation (3.16) by the standard numerical means such as the Runge-Kutta method.

However the calculation can be substantially simplified, if a considerable part of the layer is uniform in the depth coordinate x_2. Within a sublayer uniform in x_2, the calculation of the resolvent reduces from solving the differential equation to taking a function of the constant system matrix. Note that various object oriented numerical libraries (we use e.g. Mtx Vec) include an implemented matrix function for a given matrix and a given function. Moreover, the explicit formula for the resolvent is available, if the sublayer is 2D-uniform in x_1 and x_2. Therefore, the computation of the resolvent is most efficient, if we can decompose the layer into sublayers some of which are either 2D-uniform or depth-uniform or there are both. The aggregate resolvent of the layer is then calculated

via the chain rule.

We start by discussing the computation of the resolvent for two particular cases of constitutive sublayers: 2D-uniform (in x_1 and x_2) and depth-uniform (in x_2). Thereafter, we incorporate these methods into the calculation of the aggregate resolvent.

C.1.1 2D-uniform sublayer. The explicit formula

In this case, the resolvent is given by an explicit formula

$$\mathbf{R} = \begin{pmatrix} \mathbf{R}_1 & \mathbf{R}_2 \\ \mathbf{R}_3 & \mathbf{R}_1 \end{pmatrix} \text{ with } \mathbf{R}_i = \underset{-N\leqslant j\leqslant N}{\operatorname{diag}}(r_{ij}),\ i = 1, 2, 3. \tag{C.1.1}$$

Here the coefficients r_{ij} are given by (B.0.9)-(B.0.11) in the Appendix B. The calculation can be further shortened in the following way. For a uniform sublayer, the wave equation for each Fourier harmonic can be stated and solved independently. It means that we can compute the 2×2 resolvents $\mathbf{r}_j$ for each jth Fourier harmonic and then compose them into an aggregate $2(2N+1) \times 2(2N+1)$ resolvent $\mathbf{R}$ of the whole wave packet. Explicitly, we have

$$\mathbf{R} = \mathbf{U} \underset{-N\leqslant j\leqslant N}{\operatorname{diag}}(\mathbf{r}_j)\mathbf{U}^{-1} \text{ with } \mathbf{r}_j = \begin{pmatrix} r_{1j} & r_{2j} \\ r_{3j} & r_{1j} \end{pmatrix}, \tag{C.1.2}$$

where the permutation matrix $\mathbf{U}$ is given by (B.0.3).

C.1.2 Depth-uniform sublayer. The function of system matrix

The system matrix $\mathbf{Q}$ here is constant and the resolvent $\mathbf{R}$ is given by

$$\mathbf{R} = (\alpha\mathbf{I} - \exp(l\mathbf{Q}))^{-1} \tag{C.1.3}$$

with l denoting the thickness of the sublayer. We compute the formula (C.1.3) via the function of a matrix defined by the scalar function of its eigenvalues. The function of a matrix may be defined via the spectral decomposition. Given a constant diagonalizable matrix

$$\mathbf{A} = \mathbf{C} \operatorname*{diag}_{-N \leqslant i \leqslant N} (z_i) \mathbf{C}^{-1}$$

and a function $f(z),\ f : \mathbb{C} \to \mathbb{C}$, we define a function $f(\mathbf{A})$ of a matrix via

$$f(\mathbf{A}) := \mathbf{C} \operatorname*{diag}_{-N \leqslant i \leqslant N} (f(z_i)) \mathbf{C}^{-1}. \tag{C.1.4}$$

For a diagonalizable system matrix $\mathbf{Q}$, the eigenvalues λ_i of the resolvent (C.1.3) are given by the eigenvalues z_i of $\mathbf{Q}$, that is $\lambda_i = (\alpha - e^{lz_i})^{-1}$. Computing them numerically, we can avoid the instabilities for the case, when the values $\operatorname{Re} z_i$ are relatively big. In stable terms, the computational formula for the resolvent $\mathbf{R}$ has the form

$$\mathbf{R} = f(\mathbf{Q}) \quad \text{with} \quad f(z) = \begin{cases} (\alpha - e^{lz})^{-1}, & \text{if } \operatorname{Re} z < 0, \\ e^{-lz}(\alpha e^{-lz} - 1)^{-1}, & \text{otherwise.} \end{cases} \tag{C.1.5}$$

We find $\mathbf{R}$ via (C.1.5) for any $\mathbf{Q}$, since the analytical function f can be extended to the class of non-diagonalizable matrices $\mathbf{Q}$. Note that numerical instabilities can arise for a $\mathbf{Q}$ with multiple eigenvalues due to the instability of the eigenvalue algorithms in this case. However this fact restricts rarely the practical implementation of (C.1.5), since the multiple eigenvalues are seldom present on the (ω, k_1)-plane and therefore practically not involved in the numerical grid used for the calculation.

C.1.3 Multilayer. The chain rule

If we have a 2D- or depth-uniform sublayers alternating with the heterogeneous ones, then we can take advantage of the simple computation for the uniform sublayers in the

following way.

First, we decompose the unit cell into three possible types of horizontal sublayers according to the uniformity criteria, namely, (i) 2D-uniform, (ii) depth-uniform, (iii) 2D-heterogeneous. Then we compute the resolvent for every layer applying (C.1.2), (C.1.5) or (3.16), correspondingly. Note that the number of operations needed for the calculation of the layer resolvent via the three approaches differs substantially. The formula (C.1.2) corresponds to $O(N)$ operations for computing the coefficients of $\mathbf{r}_j$'s and putting them into the matrix $\mathbf{R}$, since $\mathbf{U}$ reduces to a permutation. In turn, (C.1.5) yields $O(N^3)$ operations for the square matrix manipulations. Finally, (3.16) needs $N_{step}O(N^3)$ operations for the Runge-Kutta algorithm with N_{step} steps.

Secondly, the aggregate resolvent of the plate is obtained from the layer resolvents via a successive application of the resolvent chain rule (A.1.3). Note that if there are two successive 2D-uniform layers, the chain rule (A.1.3) can be further simplified. In this case, we can apply (A.1.3) instead of $\mathbf{R}(b,a)$ and $\mathbf{R}(c,b)$ directly to the corresponding 2×2 resolvents $\mathbf{r}_j(b,a)$ and $\mathbf{r}_j(c,b)$ of the Fourier harmonics given by $\mathbf{R} = \mathbf{U} \operatorname*{diag}_{-N\leqslant j\leqslant N} \mathbf{r}_j \mathbf{U}^{-1}$. The aggregate resolvent has then the form

$$\mathbf{R}(c,a) = \mathbf{U} \operatorname*{diag}_{-N\leqslant j\leqslant N} \mathbf{r}_j(c,a)\mathbf{U}^{-1}. \tag{C.1.6}$$

C.1.4 Examples of the calculation scheme

Let us exemplify the calculation steps for the layer resolvent basing on the procedure detailed above. For the profile with rectangular inclusions depicted in Fig. C.1(a), the resolvent $\mathbf{R}_l$ of the aggregate layer can be calculated in the most efficient way in three steps as follows.

1. $\mathbf{R}_{layer1}$ for the depth-uniform layer 1 is obtained by the matrix function formula (C.1.5).

2. $\mathbf{R}_{layer2}$ for 2D-uniform layer 2 is obtained by the explicit formula (C.1.2).

(a) (b)

Figure C.1: Two unit cells partitioned into layers.

3. $\mathbf{R}_l$ is obtained by the chain rule (A.1.3) from the both layer resolvents $\mathbf{R}_{layer1}$ and $\mathbf{R}_{layer2}$.

For the profile with circular inclusions depicted in Fig. C.1(b), the plate resolvent can be calculated in five steps.

1. $\mathbf{R}_{layer1}$ for 2D-uniform layer 1 is obtained by the explicit formula (C.1.2).

2. $\mathbf{R}_{layer2}$ for heterogeneous layer 2 is obtained by the Runge-Kutta algorithm for (3.16).

3. $\mathbf{R}_{layer3}$ for the layer 3 is obtained by a symmetry transformation (A.3.6) of $\mathbf{R}_{layer2}$, since the layer 3 is the reflected layer 2.

4. $\mathbf{R}_{layer4}$ for 2D-uniform layer 4 is obtained by the explicit formula (C.1.2).

5. $\mathbf{R}_l$ is obtained by the chain rule (A.1.3) from all the four layer resolvents $\mathbf{R}_{layer1}$, $\mathbf{R}_{layer2}$, $\mathbf{R}_{layer3}$ and $\mathbf{R}_{layer4}$.

C.2 Options for calculation of the projector

There exist several options for obtaining the projector. We present them in the order of increasing of computation time. By the substrate we mean either upper or lower half-spaces.

C.2.1 2D-uniform substrate. The explicit formula

If the substrate unit cell is uniform, then the projector matrix has an explicit form; see (B.0.12)-(B.0.14) in Appendix B.

C.2.2 Depth-uniform substrate. The function of system matrix

In the case of the depth-independent unit cell of the substrate, the system matrix $\mathbf{Q}_{\rm sub}$ for the substrate does not depend on the depth coordinate x_2. So the projectors can be obtained without using the resolvent of propagator through the unit cell but just as a function of system matrix

$$\begin{aligned} \mathbf{P}_d = g_d(\mathbf{Q}_{\rm sub}) \ \text{ with } \ g_d(z) = \begin{cases} 1, & \text{if } \operatorname{Re} z < 0, \\ 0, & \text{otherwise,} \end{cases} \\ \mathbf{P}_i = g_i(\mathbf{Q}_{\rm sub}) \ \text{ with } \ g_i(z) = \begin{cases} 1, & \text{if } \operatorname{Re} z > 0, \\ 0, & \text{otherwise.} \end{cases} \end{aligned} \tag{C.2.1}$$

To justify these formulas, we note that in the uniform case we have $\mathbf{M}_{\rm sub} = \exp(T_2\mathbf{Q}_{\rm sub})$, where T_2 is arbitrary, and so the eigenvalues q_j of $\mathbf{M}_{\rm sub}$ are exponentials of eigenvalues z_j of $\mathbf{Q}_{\rm sub}$. Hence the absolute value of the eigenvalue of $\mathbf{M}_{\rm sub}$ is less than 1 iff the real part of corresponding eigenvalue of $\mathbf{Q}_{\rm sub}$ is less than 0.

C.2.3 2D-periodic substrate. The function of resolvent matrix

In this case, we implement, by means of the function $f(\mathbf{R}_{\rm sub})$ of the resolvent matrix, the spectral projector definition (4.25) with (4.20) via the propagator eigenvalues:

$$\mathbf{P}_d\boldsymbol{w} = \boldsymbol{w} \ \Leftrightarrow \ \boldsymbol{w} \in E_d \tag{C.2.2}$$

with

$$E_d := \mathrm{span}\{\boldsymbol{w} : \mathbf{M}_{\mathrm{sub}}\boldsymbol{w} = q\boldsymbol{w}, |q| < 1\}. \tag{C.2.3}$$

Hence the eigenvalues w_j of $\mathbf{P}_d$ are given through the corresponding eigenvalues q_j of the propagator $\mathbf{M}_{\mathrm{sub}}$ as

$$w_j(q_j) = \begin{cases} 1, & \text{if } |q_j| < 1, \\ 0, & \text{otherwise.} \end{cases} \tag{C.2.4}$$

Recalling that $\mathbf{M}_{\mathrm{sub}}$ is numerically unstable, it remains, for the sake of stability, to express q_j in terms of the eigenvalues λ_j of the resolvent $\mathbf{R}_{\mathrm{sub}}$. Assuming $\mathbf{R}_{\mathrm{sub}}$ is diagonalizable, we have

$$q_j = z - \lambda_j^{-1}. \tag{C.2.5}$$

Identifying q_j numerically, we have to avoid calculating sufficiently big values of q_j, i.e. small values of λ_j, which anyway give $w_j = 0$ as (C.2.4) states. The key observation to do so is

$$|\lambda_j| \leqslant (|z| + 1)^{-1} \;\Rightarrow\; |q_j| \geqslant 1. \tag{C.2.6}$$

This can be derived as follows. Observe that $|\lambda_j| \leqslant (|z| + 1)^{-1}$ is equivalent to

$$|\lambda_j|^{-1} \geqslant |z| + 1. \tag{C.2.7}$$

At the same time, (C.2.5) yields

$$|q_j| \geqslant |\lambda_j|^{-1} - |z| \tag{C.2.8}$$

due to the triangle inequality. Inserting (C.2.7) into (C.2.8) implies $|q_j| \geqslant 1$. The statement (C.2.6) is proved. Consequently, $\lambda_j \in A$ with

$$A = \{\lambda : |\lambda| \leqslant (|z| + 1)^{-1}\} \tag{C.2.9}$$

directly yields $w_j = 0$ and it suffices to verify the condition $|q_j| < 1$ only for $\lambda_j \notin A$. On these grounds, we recast (C.2.4) via λ_j in stable terms and obtain the following computational formula for the projector $\mathbf{P}_d$:

$$\mathbf{P}_d = f_d(\mathbf{R}_{\rm sub}) \quad \text{with} \quad f_d(\lambda) = \begin{cases} 1, & \text{if } |z - \lambda^{-1}| < 1 \text{ with } \lambda \notin A, \\ 0, & \text{otherwise.} \end{cases} \tag{C.2.10}$$

Similarly

$$\mathbf{P}_i = f_i(\mathbf{R}_{\rm sub}) \quad \text{with} \quad f_i(\lambda) = \begin{cases} 1, & \text{if } \lambda \in A, \\ 1, & \text{if } |z - \lambda^{-1}| > 1 \text{ with } \lambda \notin A, \\ 0, & \text{otherwise.} \end{cases} \tag{C.2.11}$$

C.2.4 2D-periodic substrate. The sum of resolvents

Let us discuss an alternative computation of the projector as a sum of resolvents $\mathbf{R}_{\rm sub}(z)$ – based on the projector definition (4.31) via a path integral. This implementation can be useful in particular for parallel programming. The matrix $\mathbf{P}_d$ defined as a path integral (see (4.31))

$$\mathbf{P}_d = \frac{1}{2\pi i} \oint_{|z|=1-0} \mathbf{R}_z dz \tag{C.2.12}$$

can be expressed in terms of the matrices $\mathbf{R}_{\rm sub}(z) = (z\mathbf{I} - \mathbf{M}_{\rm sub})^{-1}$ with varying complex parameter z. We have the approximation

$$\mathbf{P}_d = \frac{1}{2\pi i} \oint_{|z|=1-\varepsilon} \mathbf{R}_{\rm sub}(z) dz \approx \frac{(1-\varepsilon)}{n} \sum_{m=1}^{n} e^{2\pi i \frac{m}{n}} \mathbf{R}_{\rm sub}((1-\varepsilon)e^{2\pi i \frac{m}{n}}) \tag{C.2.13}$$

for n sufficiently big and ε small enough. Here any matrix $\mathbf{R}_{\rm sub}(z)$ with a varying z can be obtained in terms of the matrix $\mathbf{R}_{\rm sub}(z_0)$ with a fixed z_0 via the identity (A.1.4), namely,

$$\mathbf{R}_{\rm sub}(z) = \mathbf{R}_{\rm sub}(z_0)(\mathbf{I} - (z_0 - z)\mathbf{R}_{\rm sub}(z_0))^{-1}. \tag{C.2.14}$$

Substitution of (C.2.14) in (C.2.13) gives a stable computational formula for the projector $\mathbf{P}_d$.

C.3 Calculation of the propagators for decreasing modes

The propagator $\mathbf{M}_d \equiv \mathbf{M}_d(T_2 + x_2, x_2)$ for decreasing modes in a 2D-periodic substrate (see definition (6.26)) can be recasted as

$$\mathbf{M}_d \boldsymbol{w}_j = \begin{cases} q_j \boldsymbol{w}_j, & |q_j| < 1 \\ \mathbf{0}, & \text{elsewhere} \end{cases}, \tag{C.3.1}$$

where $\boldsymbol{w}_j$ are the eigenvectors composing the wave field $\boldsymbol{\eta}(x_2)$ and q_j the eigenvalues of the substrate propagator $\mathbf{M}_{sub}(x_2 + T_2, x_2)$. This gives the implementation of $\mathbf{M}_d$ as a matrix function of the corresponding resolvent $\mathbf{R}_z(T_2 + x_2, x_2)$:

$$\mathbf{M}_d(T_2{+}x_2, x_2) = h_d(\mathbf{R}_z(T_2{+}x_2, x_2)) \ \text{ with } \ h_d(\lambda) = \begin{cases} z - \lambda^{-1}, & \text{if } |z - \lambda^{-1}| < 1 \text{ with } \lambda \notin A, \\ 0, & \text{otherwise.} \end{cases} \tag{C.3.2}$$

Here the set A is defined by (C.2.9). The derivation of the formula (C.3.2) is analogous to the formula (C.2.10) for the implementation of the spectral projector $\mathbf{P}_d$ as a matrix function of a resolvent in Appendix C.2.3. Note that the matrix functions h_d in (C.3.2) and f_d in (C.2.10) are linked.

The propagator $\mathbf{M}_{dop}(0, T_2)$ for the modes decreasing in the direction opposite to the di-

rection of reference in a 2D-periodic substrate (see definition (6.27)) can be also calculated via matrix function h_d of the backward resolvent $\mathbf{R}_z(x_2 - T_2, x_2)$ as

$$\mathbf{M}_{dop}(x_2 - T_2, x_2) = h_d(\mathbf{R}_z(x_2 - T_2, x_2)) \tag{C.3.3}$$

or even via the forward resolvent $\mathbf{R}_z(x_2, x_2 - T_2)$ as

$$\mathbf{M}_{dop}(x_2 - T_2, x_2) = \mathbf{T}\Big(h_d(\mathbf{R}_z(x_2, x_2 - T_2))\Big)^* \mathbf{T}^{-1}, \tag{C.3.4}$$

since we have, similarly to the identity (A.2.8) for the projectors $\mathbf{P}_i$ and $\mathbf{P}_d$, the identity for $\mathbf{M}_{dop}(x_2 - T_2, x_2)$ and $\mathbf{M}_d(x_2, x_2 - T_2)$:

$$\mathbf{M}_{dop}(x_2 - T_2, x_2) = \frac{1}{2\pi i} \oint\limits_{|z|=1-0} z\mathbf{R}_z(x_2 - T_2, x_2)dz = \frac{1}{2\pi i} \oint\limits_{|z|=1-0} z\mathbf{T}\mathbf{R}^*_{\overline{z}}(x_2, x_2 - T_2)\mathbf{T}^{-1}dz$$

$$= \mathbf{T}\Big(\frac{1}{2\pi i} \oint\limits_{|z|=1-0} z\mathbf{R}^*_{\overline{z}}(x_2, x_2 - T_2)dz\Big)\mathbf{T}^{-1} = \mathbf{T}\Big(-\frac{1}{2\pi i} \oint\limits_{|z|=1-0} \overline{z}\mathbf{R}_{\overline{z}}(x_2, x_2 - T_2)d\bar{z}\Big)^* \mathbf{T}^{-1}$$

$$= \mathbf{T}\Big(\frac{1}{2\pi i} \oint\limits_{|z|=1-0} z\mathbf{R}_z(x_2, x_2 - T_2)dz\Big)^* \mathbf{T}^{-1} = \mathbf{T}\mathbf{M}^*_d(x_2, x_2 - T_2)\mathbf{T}^{-1}. \tag{C.3.5}$$

Appendix D

The spectrum of the propagating waves calculated via resolvent

D.1 Dispersion equation

The projection of the propagating wave spectrum is given by the spectral projector $\mathbf{P}_p$, namely by $\mathrm{trace}\,\mathbf{P}_p$. However at a fixed k_2, the spectral projector gives no dispersion data. The propagating wave spectrum at a fixed k_1 or k_2 can be given by the resolvent $\mathbf{R}$.

We calculate k_2 in terms of the eigenvalues λ_j, $1 \leqslant j \leqslant 2(2N+1)$, of the resolvent $\mathbf{R}(\omega, k_1) = (\alpha\mathbf{I} - \mathbf{M})^{-1}$ at a fixed (ω, k_1). On the one hand, the eigenvalues q_j, $1 \leqslant j \leqslant 2(2N+1)$, of the propagator $\mathbf{M}(\omega, k_1)$ satisfy $|q_j| = 1$ ensuring no decay in x_2, that is,

$$q_j = e^{ik_2 T_2}. \tag{D.1.1}$$

Note that $\mathbf{M}(\omega, k_1)$ is considered with real k_1 which ensures no decay in x_1. On the other hand,

$$q_j = \alpha - \lambda_j^{-1}. \tag{D.1.2}$$

Setting equal the both identities (D.1.1) and (D.1.2) gives the result (D.1.3) in terms of the

appropriate resolvent eigenvalues $\lambda_j,\ 1 \leqslant j \leqslant 2(2N+1)$:

$$k_2 = \frac{1}{iT_2}\operatorname{Log}(\alpha - \lambda_j^{-1}) = \frac{1}{T_2}\operatorname{Arg}(\alpha - \lambda_j^{-1}) \text{ with } \lambda_j \text{ such that } |\alpha - \lambda_j^{-1}| = 1. \tag{D.1.3}$$

Here we use the definition of the complex logarithm Log as follows:

$$\operatorname{Log} z = \ln|z| + i\operatorname{Arg} z,\ \operatorname{Arg} z \in (-\pi, \pi). \tag{D.1.4}$$

D.2 Numerical implementation

We consider the reduced Brillouin zone given by the triangle with vertices $(k_1, k_2) = (0,0)$, $(\pi, 0)$ and (π, π). For the second edge $k_1 = \pi,\ k_2 \in [0, \pi]$, we obtain the whole range of k_2 calculating it for every ω and a fixed $k_1 = \pi$. We find k_2 by (D.1.3) as a function of the resolvent eigenvalues λ_j:

$$k_2 = f(\lambda_j) \quad \text{with} \quad f(q) = \begin{cases} \frac{1}{T_2}\operatorname{Arg}(\alpha - \lambda^{-1}), & \text{if } |\lambda| > 0 \text{ and } |\alpha - \lambda^{-1}| \approx 1, \\ 0, & \text{otherwise.} \end{cases} \tag{D.2.1}$$

We calculate two other edges at the same time for every ω and k_1. For $k_2 = 0$ and each $k_1 \in [0, \pi]$, we find all $\omega = \omega(k_1)$ such that $(k_2 =) f(\omega(k_1)) = 0$. For each pair $k_1 = k_2 \in [0, \pi]$, we find all $\omega(k_1)$ such that $(k_2 =) f(\omega(k_1)) = k_1$.

D.3 Numerical examples

We display the spectra of the propagating waves for 2D periodic spaces in the reduced Brillouin zone spanned in a triangle between $(0,0)$, $(\pi, 0)$ and (π, π).

Consider an epoxy space with periodically distributed circular or square rods; see Figs. D.1 (a) and (b). The geometrical parameters are $T_1 = 1$ mm and $T_2 = 1.4$ mm. For

comparison, we display the spectrum for the uniform epoxy space considered formally as periodic. This spectrum is given by folded dispersion branches; see Fig. D.1 (c).

We change the size, material and form of inclusions observing how it affects the stop band pattern. The inclusions of different forms and materials, steel circular and silicium square, but similar size (circular inclusions of radius $r = 0.08$ mm and square rods of radius $r = 0.1$ mm), produce a similar perturbation of the spectrum; see Figs. D.1 (d) and (e). The dispersion branches in this case are repulsed both at the edges $(0, 0)$, $(\pi, 0)$ and (π, π) and inside the Brillouin zone giving local stop bands around the corresponding frequencies. However if we increase the size of inclusions, e.g. we increase the radius r of the silicium square rods from 0.1 to 0.2 mm, then the size of the local stop bands gets bigger producing absolute stop bands. See e.g. the low-frequency stop band given by repulsion of the first and second dispersion branches in Fig. D.1 (f).

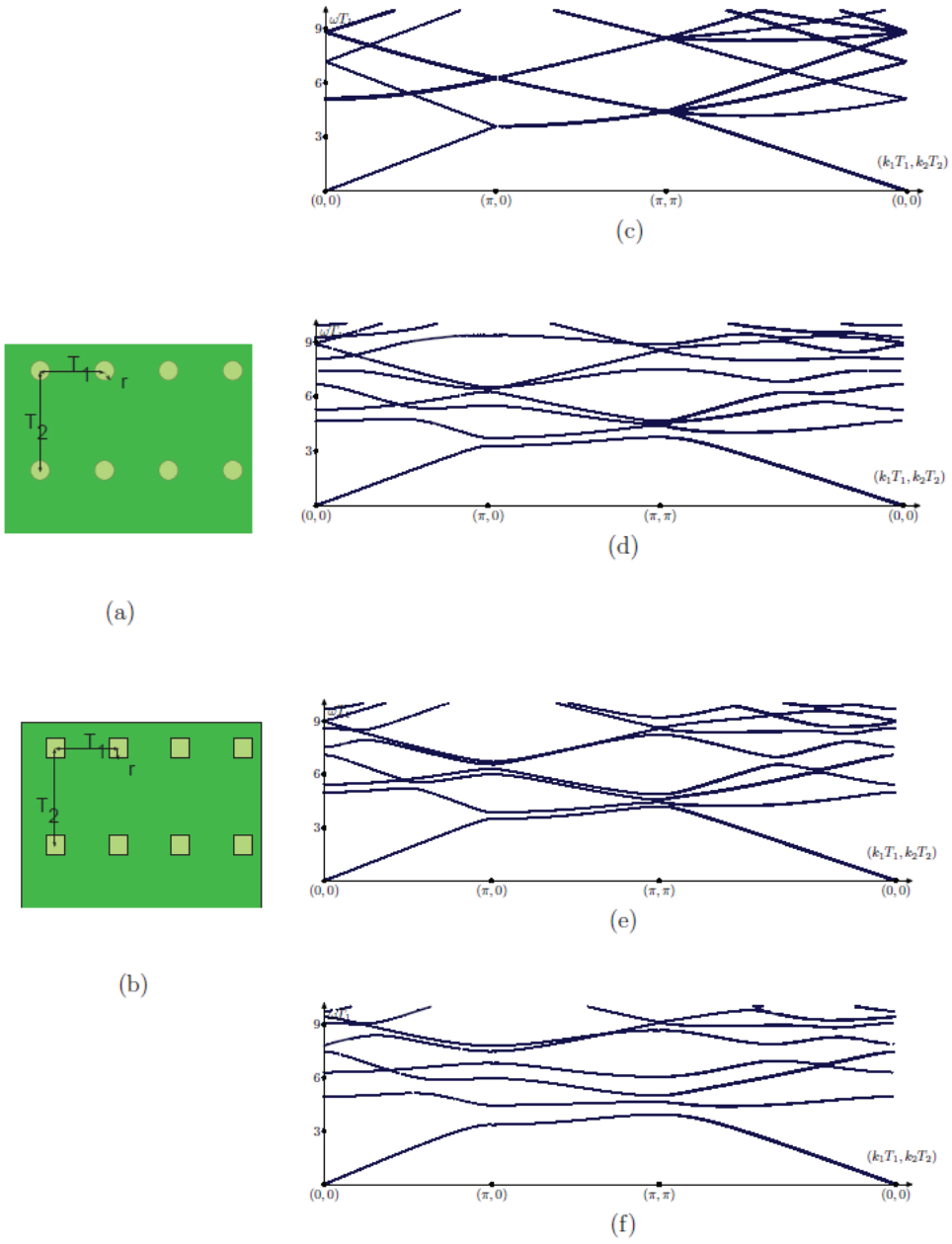

Figure D.1: 2D-periodic (half-)space with (a) steel circle and (b) silicium square inclusions. Spectra for (c) uniform, i.e. $r = 0$, (d) $r = 0.08$ mm. Spectra for (b) with (e) $r = 0.1$ mm, (f) $r = 0.2$ mm

Bibliography

[1] P. A. Deymier (ed.). Acoustic metamaterials and phononic crystals. Springer, Berlin (2013)

[2] E. H. El Boudouti, B. Djafari-Rouhani, E. M. Khourdifi, L. Dobrzynski. Surface and interface waves in superlattices: Transverse localized and resonant modes. Phys. Rev. B **48**, 10987-10997 (1993)

[3] E. H. El Boudouti, B. Djafari-Rouhani, A. Akjouj, and L. Dobrzynski. Theory of surface and interface elastic waves in N-layer superlattices. Phys. Rev. B **54**, 14728-14740 (1996)

[4] M. Hammouchi, E. H. El Boudouti, A. Nougaoui, B. Djafari-Rouhani, M. L. H. Lahlaouti, A. Akjouj, and L. Dobrzynski. Acoustic waves in finite superlattices: Influence of buffer layers. Phys. Rev. B **59**, 1999-2010 (1999)

[5] S. Mizuno. Eigenfrequency and decay factor of the localized phonon in a superlattice with a defect layer. Phys. Rev. B **65**, 193302 (2002)

[6] S. Tamura, H. Watanabe, and T. Kawasaki. Acoustic-phonon cavity modes in one-dimensional multilayered elastic structures. Phys. Rev. B **72**, 165306 (2005)

[7] Ph. Gatignol, C. Potel, and J. F. de Belleval. Two families of modal waves for periodic structures with two field functions: a Cayleigh-Hamilton approach. Acustica-Acta Acustica **93**, 959-975 (2007)

[8] K.-M. Li, L.-L. Wang, W.-Q. Huang, and B.-S. Zou. Effect of diffusion layers and defect layer on acoustic phonons transport through the structure consisting of different films. Phys. Lett. A **372**, 5046-5051 (2008)

[9] L. Castro-Arce, B. Manzanares-Martínez, and F. Ramos-Mendieta. Localized sagittal modes of variable transverse and longitudinal components in one-dimensional phononic crystals. J. Appl. Phys. **107**, 033515 (2010)

[10] M.V. Golub, C. Zhang, and Y.-S. Wang. SH-wave propagation and scattering in periodically layered composites with a damaged layer. J. Sound Vibr. **331** 1829-1843 (2012)

[11] J. O. Vasseur, A.-C. Hladky-Hennion, B. Djafari-Rouhani, F. Duval, B. Dubus, Y. Pennec, and P. A. Deymier. Waveguiding in two-dimensional piezoelectric phononic crystal plates. J. Appl. Phys. **101**, 114904 (2007)

[12] Y. Pennec, B. Djafari-Rouhani, H. Larabi, J. O. Vasseur, and A.-C. Hladky-Hennion. Low frequency gap in a phononic crystal constituted of cylindrical dots deposited on a thin homogeneous plate. Phys. Rev. B **78**, 104105 (2008)

[13] M. B. Assouar and M. Oudich. Dispersion curves of surface acoustic waves in a two-dimensional phononic crystal. Appl. Phys. Lett. **99**, 123505 (2011)

[14] Y. Achaoui, A. Khelif, S. Benchabane, L. Robert, and V. Laude. Experimental observation of locally-resonant and Bragg band gaps for surface guided waves in a phononic crystal of pillars. Phys. Rev. B **83**, 104201 (2011)

[15] M. Oudich and M. B. Assouar. Surface acoustic wave band gaps in a diamond-based two-dimensional locally resonant phononic crystal for high frequency applications. J. Appl. Phys. **111**, 014504 (2012)

[16] D. Yudistira, Y. Pennec, B. Djafari Rouhani, S. Dupont, and V. Laude. Non-radiative complete surface acoustic wave bandgap for finite-depth holey phononic crystal in lithium niobate. Appl. Phys. Lett. **100**, 061912 (2012)

[17] V. M. García-Chocano, R. Graciá-Salgado, D. Torrent, F. Cervera, and J. Sánchez-Dehesa. Quasi-two-dimensional acoustic metamaterial with negative bulk modulus. Phys. Rev. B **85**, 184102 (2012)

[18] V. L. Zhang, C. G. Hou, H. H. Pan, F. S. Ma, M. H. Kuok, H. S. Lim, S. C. Ng, M. G. Cottam, M. Jamali, and H. Yang. Phononic dispersion of a two-dimensional chessboard-patterned bicomponent array on a substrate. Appl. Phys. Lett. **101**, 053102 (2012)

[19] Y. Li, Z. Hou, M. Oudich, and M. B. Assouar. Analysis of surface acoustic wave propagation in a two-dimensional phononic crystal. J. Appl. Phys. **112**, 023524 (2012)

[20] A. Khelif, Y. Achaoui, and B. Aoubiza. Surface acoustic waves in pillars-based two-dimensional phononic structures with different lattice symmetries. J. Appl. Phys. **112**, 033511 (2012)

[21] M. A. Al-Lethawe, M. Addouche, A. Khelif, and S. Guenneau. All-angle negative refraction for surface acoustic waves in pillar-based two-dimensional phononic structures. New J. Phys. **14**, 123030 (2012)

[22] C. Charles, B. Bonello, and F. Ganot. Propagation of guided elastic waves in two-dimensional phononic crystals. Ultrasonics **44**, 1209(E) (2006)

[23] J.C. Hsu and T.T. Wu. Efficient formulation for band-structure calculations of two-dimensional phononic-crystal plates. Phys. Rev. B **74**, 144303 (2006)

[24] A. Khelif, B. Aoubiza, S. Mohammadi, A. Adibi, and V. Laude. Complete band gaps in two-dimensional phononic crystal slabs. Phys. Rev. E **74**, 046610 (2006)

[25] J.-H. Sun and T.-T. Wu. Propagation of acoustic waves in phononic crystal plates and waveguides using a finite-difference time-domain method. Phys. Rev. B **76**, 104304 (2007)

[26] J. O. Vasseur, P. Deymier, B. Djafari-Rouhani, Y. Pennec, and A. C. Hladky-Hennion. Absolute forbidden bands and waveguiding in two-dimensional phononic crystal plates. Phys. Rev. B **77**, 085415 (2008)

[27] S. Mohammadi, A. A. Eftekhar, W. D. Hunt, and A. Adibi. High-Q micromechanical resonators in a two-dimensional phononic crystal slab. Appl. Phys. Lett. **94**, 051906 (2009)

[28] Y. Pennec, J. O. Vasseur, B. Djafari-Rouhani, L. Dobrzynski, and P. Deymier. Two-dimensional phononic crystals: Examples and application. Surface Sci. Pep. **65**, 229-291 (2010)

[29] B. Djafari-Rouhani, J. O. Vasseur, A. C. Hladky-Hennion, P. Deymier, F. Duval, B. Dubus, and Y. Pennec. Absolute band gaps and waveguiding in free standing and supported phononic crystal slabs. Phonon. Nanostruct. Fundam. Appl. **6**, 32-37 (2011)

[30] T.-T. Wu, J.-C. Hsu, and J.-H. Sun. Phononic Plate Waves. IEEE Trans. Ultrason. Ferroelectr. Freq. Control **58**, 2146-2161 (2011)

[31] Y. Yao, F. Wu, Z. Hou, and Z. Xin. Lamb waves in two-dimensional phononic crystal plate with anisotropic inclusions. Ultrasonics **51**, 602-605 (2011)

[32] Y. Cheng, X. J. Liu, and D. J. Wu. Band structures of phononic-crystal plates in the form of a sandwich-layered structure. J. Acoust. Soc. Am. **130**, 2738-2745 (2011)

[33] J. Chen, Y. Xia, X. Han, and H. Zhang. Lamb waves in phononic crystal slabs: Truncated plane parallels to the axis of periodicity. Ultrasonics **52**, 920-924 (2012)

[34] M. Oudich and M. B. Assouar. Complex band structures and evanescent Bloch waves in two-dimensional finite phononic plate. J. Appl. Phys. **112**, 104509 (2012)

[35] J. Liu, F. Li, and Y. Wu. The slow zero order antisymmetric Lamb mode in phononic crystal plates. Ultrasonics **53**, 849-852 (2013)

[36] P. Wang, T.-N. Chen, K.-P. Yu, and X.-P.Wang. Lamb wave band gaps in a double-sided phononic plate. J. Appl. Phys. **113**, 053509 (2013)

[37] J. Ma, Z. Hou, and B. M. Assouar. Opening a large full phononic band gap in thin elastic plate with resonant units. J. Appl. Phys. **115**, 093508 (2014)

[38] P. Joly and S. Fliss. Wave propagation in locally perturbed periodic media (case with absorption): Numerical aspects. J. Comput. Phys. **231** (4), 1244-1271 (2012)

[39] A. A. Maradudin. Some efects of point defects on the vibrations of crystal lattices. Rep. Progr. Phys. **28**, 331-380 (1965)

[40] P. A. Martin. Discrete scattering theory: Green's function for a square lattice. Wave Motion **43**, 619-629 (2006)

[41] M. Makwana and R. V. Craster. Localised point defect states in asymptotic models of discrete lattices. Q. J. Mechanics Appl. **66** (3), 289-316(2013)

[42] A. A. Kutsenko and A. L. Shuvalov. Shear surface waves in phononic crystals. J. Acoust. Soc. Am. **133**, 653-660 (2013)

[43] A. L. Shuvalov, A. A. Kutsenko, M. E. Korotyaeva, and O. Poncelet. Love waves in a coated vertically periodic substrate. Wave Motion **50**, 809-820 (2012)

[44] M. E. Korotyaeva, A. A. Kutsenko, A. L. Shuvalov, and O. Poncelet. Love waves in two-dimensional phononic crystals with depth-dependent properties. Appl. Phys. Lett. **103**, 111902 (2013)

[45] M. E. Korotyaeva, A. A. Kutsenko, A. L. Shuvalov, and O. Poncelet. Resolvent method for calculation dispersion spectra of the shear waves in the phononic plates and waveguides. J. of Comput. Acoust. **22**, 1450008 (2014)

[46] B. A. Auld. Acoustic Fields and Waves in Solids. R.E. Krieger, Malabar, (1990)

[47] R. E. Camley, B. Djafari-Rouhani, L. Dobrzynski, and A. A. Maradudin. Transverse elastic waves in periodically layered infinite and semi-infinite media. Phys. Rev. B **27**, 7318-7329 (1983)

[48] S.-Y. Ren and Y.-C. Chang. Theory of confinement effects in finite one-dimensional phononic crystals. Phys. Rev. B **75**, 212301 (2007)

[49] A. L. Shuvalov, O. Poncelet, and S. V. Golkin. Existence and spectral properties of shear horizontal surface acoustic waves in vertically periodic half-spaces. Proc. R. Soc. A **465**, 1489-1511 (2009)

[50] M. V. Golub, S. I. Fomenko, T. Q. Bui, Ch. Zhang, and Y.-S. Wang. Transmission and band gaps of elastic SH waves in functionally graded periodic laminates. Int. J. Solids Struct. **49**, 344-354 (2012)

[51] M. C. Pease. III. Methods of matrix algebra. Academic Press, New York (1965)

[52] A. A. Kutsenko, A. L. Shuvalov, A. N. Norris, and O. Poncelet. Spectral properties of a 2D scalar wave equation with 1D-periodic coefficients: application to SH elastic waves. Math Mech Solids **18** (7), 677-700 (2013)

[53] M. Ahmad, E. Nolde, A. V. Pichugin. Explicit asymptotic modelling of transient Love waves propagated along a thin coating. Z. Angew. Math. Phys. **62**, 173-181 (2011)

[54] B. Djafari-Rouhani, A. A. Maradudin, and R. F. Wallis. Rayleigh waves on a superlattice stratified normal to the surface. Phys. Rev. B **29**, 6454 (1984)

[55] A. A. Maznev and A. G. Every. Surface acoustic waves in a periodically patterned layered structure. J. Appl. Phys. **106**, 113531 (2009)

[56] I. A. Veres and T. Berer. Complexity of band structures: Semi-analytical finite element analysis of one-dimensional surface phononic crystals. Phys. Rev. B **86**, 104304 (2012)